

Optimizing the Toehold-Mediated Strand Displacement Reaction on the Nanoparticle Surface by Altering the Surface DNA Density for the Design of a microRNA Nano-Optical Sensor

Gurbrinder Ghotra

A thesis submitted to
the Faculty of Graduate Studies
in Partial Fulfillment of the Requirements
for the Degree of
Master of Science

Graduate Program in Chemistry

York University

Toronto, Ontario

March 2019
© Gurbrinder Ghotra, 2019

Abstract

We present a method for modulating the kinetics and thermodynamic properties of aggregation and disassembly processes of DNA-functionalized nanoparticles. Specifically, we examine factors influencing the toehold strand-displacement reaction on nanoparticle surfaces. Gold nanoparticles were functionalized with oligonucleotide sequences with varying surface density by incorporating diluent DNA strands. The hybridization of DNA yields aggregates which then disassemble via a strand-displacement reaction by the target sequence. Localized surface plasmon resonance of gold nanoparticles and fluorescently tagged DNA strands were employed to gain an understanding of the aggregation and disassembly steps. The surface density of DNA impacts the aggregation kinetics, the melting temperature and the target-induced disassembly of these nanoaggregates. It does so by modulating the cooperativity and attainability of the oligonucleotides, the electrostatic repulsion between the nanoparticles and the accessibility of the linkers to the target nucleic acid. A dramatic decrease in the initiation time and increase in the rate of disassembly are achieved by optimizing the surface density. Our work provides insight into the strand-displacement reaction on nanoparticle surfaces that underpins various sensing and DNA-driven nanomachine applications. This fundamental understanding allowed the design of a label-free, low cost and miniaturized biosensing platform based on the disassembly of core-satellite nanoassemblies. We successfully manipulate the system for the rapid and selective detection of a nucleic acid biomarker – microRNA-210, enabling diverse biological applicability.

Acknowledgments

First of all, I would like to take this opportunity to express a heartfelt thanks to Dr. Jennifer Chen of Faculty of Science and Engineering at York University for the constant guidance and supervision throughout my thesis work. This thesis would not have been possible without her timely suggestions and discussions. It has been a very rewarding experience working with her research group. Besides my advisor, I am grateful to the rest of my thesis committee members: Prof. Sergey N. Krylov and Prof. Derek Wilson for their directions and suggestions.

I extend my thanks to all fellow group members for always being helpful and supportive. Especially, Bach Kim Nguyen and Anthony Le for the training and for laying a strong foundation for my project. My heartfelt gratitude to my loving father and mother for moral support and encouragement throughout my degree. Last but not least, I would like to thank my wife Harpreet Bhalay for the tremendous support.

Table of Contents

Abstract	ii
Acknowledgments.....	iii
Table of Contents.....	iv
List of Tables.....	vii
List of Figures.....	viii
List of Equations	xii
List of Schemes	xiii
List of Abbreviations	xiv
 Chapter 1. Introduction.....	 1
1.1 General Principles of a Biosensor and of Localized Surface Plasmon Resonance	1
1.2 Plasmonic Hybridization and Coupling	2
1.3 Factors Influencing the LSPR	4
1.4 DNA Functionalized AuNP in Sensing Applications: Solution-Based Biosensing and Colorimetric Assay	4
1.5 Factors Influencing the Behavior of DNA on AuNP	6
1.6 Overview of the Target and Comparison of Different Sensing Platforms	8
 Chapter 2. Implications of Altering the Surface DNA Density of AuNPs on the Thermodynamic and Kinetic Properties of Nanoaggregate Formation and Their Disassembly Via a Toe-Hold Mediated Strand Displacement Reaction.	 15
2.1 Introduction.....	15
2.1.1 Toehold Mediated Strand Displacement Reaction in DNA Nanotechnology	15
2.1.2 Objective	17
2.2 Experimental.....	18
2.2.1 Reagent, Materials and DNA	18
2.2.2 Reducing thiolated-DNA:	19
2.2.3 AuNP Cap exchange:	19
2.2.4 Conjugation of DNA onto 30-nm AuNPs:.....	20
2.2.5 Determining DNA Loading on Satellite NPs.....	20

2.2.6	Determining Accessibility of the DNA Immobilized on AuNPs (30-nm) for Various Surface Densities.....	21
2.2.7	Aggregation in solution.....	21
2.2.8	Thermal Disassembly of nanoaggregates in solution (melting of DNA duplexes)	22
2.2.9	Target-induced disassemble of aggregates in solution.....	22
2.2.10	Disassembly using fluorescently tagged target (DNA-210-CY3)	22
2.3	Results and Discussion.....	24
2.3.1	Structure and Function of DNA Strands Immobilized on AuNPs in the Aggregation and Disassembly Processes.	24
2.3.2	Determining the Surface Density of Functional and Diluent DNA on the AuNP.	26
2.3.3	Strategy Employed to Modulate Surface Coverage of Functional DNA.....	27
2.3.4	Determining the Accessibility of Immobilized Functional DNA Strands and the Effect of Incorporating Diluent DNA on the Accessibility	27
2.3.5	Exploring the Impact of the Surface DNA Density on the Aggregation of AuNPs	30
2.3.6	Effect of Surface Density of Functional DNA on the Thermal Disassembly of Nanoaggregates	34
2.3.7	Influence of Surface DNA Density on the Target-Induced Disassembly of Nanoaggregates	40
2.3.8	Using Fluorescently-Tagged Target to Determine the Impact of Surface DNA Density on the Toe-Hold Mediated Nanoaggregate Disassembly Process	44
2.4	Conclusion	47
Chapter 3. A Biosensing Platform: Detection of Oligonucleotide Biomarkers Based on the Disassembly of the Plasmonic Core-Satellite Nanocluster		49
3.1	Introduction.....	49
3.1.1	Surface-bound nanostructure: Discrete nanoparticle dimer structures	50
3.1.2	Surface-bound core-satellite nanoassemblies	52
3.1.3	Purpose.....	54
3.2	Experimental.....	56
3.2.1	Activation and Preparation of Silanized Glass Substrate.....	56
3.2.2	Deposition and DNA-functionalization of Core AuNPs on amino-modified substrate.....	56
3.2.3	Passivation of the substrate surface after core functionalization	57
3.2.4	Layer-by-layer assembly on the core AuNPs.....	57
3.2.5	Detection of the biomarker (DNA-210 or miR-210) by core-satellite disassembly	58

3.2.6 Cell-lysate preparation (hypoxic and normoxic cells)	58
3.3 Results and Discussion	59
3.3.1 Fabrication of a Core-Satellite Nanocluster on a Glass Substrate	60
3.3.2 Method for the Optical Analysis Assembly and Disassembly Process.....	63
3.3.3 Monitoring the Assembly of Core-Satellite Nanocluster Anchored on the Substrate .	64
3.3.4 Sensing of Oligonucleotide Biomarkers Based on the Disassembly of the Plasmonic Core-Satellite Nanocluster	68
3.3.5 Calibration Curve for DNA-210 and miR-210 sensing	70
3.3.6 Direct Measurement in Cell Lysate	73
3.4 Conclusion	76
Chapter 4. Outlook and Future work	78
4.1 Summary	78
4.2 Outlook and Future Work	81
Chapter 5. References	83
Appendix A	89

List of Tables

Table 2-1 Maximum Surface DNA density determined by using Scheme 2-2 for all Surface-DNAs used in the study

Table 2-2 Summary of results obtained from the accessibility determination experiments showing the number and percentage of AuNP-functionalized strands (Probe and Seq. 2) that accessible for hybridization at various surface DNA densities.

Table 2-3 Summary of parameter obtained from Figure 2-3. Impact of the surface density of DNA on the melting profile, hence on thermodynamic (T_m , melting on-set and offset) and kinetic properties (FWHM) of these nanoaggregates. Symmetry factor reveals the relative contribution of cooperativity and interparticle repulsion on the disassembly rate. Note, T_m and Inflection point are not identical values due to asymmetry.

Table 2-4 A tabulated summary of the impact of surface DNA density on the charge and crowdedness on the AuNP surface.

Table 2-5 Summary of parameter obtained from Figure 2-5. Impact of the surface density of DNA on the thermodynamic (T_{50}) and kinetic properties (FWHM) of target-induced disassembly of nanoaggregates, and on the charge and crowdedness on the AuNP surface.

List of Figures

Figure 1-1 (a) Illustration of the phenomenon of localized surface plasmon resonance which occurs when the electric field of the electro-magnetic radiation interacts with the free conduction electrons of a metallic NP which is smaller than the light's wavelength. Adapted from reference 9 with permission. (b) Energy diagram of plasmon hybridization showing splitting of bonding (σ) and antibonding (σ^*) plasmons as NPs are brought in proximity to each other. Adapted from reference 3 with permission.

Figure 1-2 An illustration of a sensing technique based on the aggregation of NPs. (A) the mechanism of a reversible aggregation of AuNPs through a specific linker DNA strand at temperatures lower than the melting temperature of the linker-capture DNA hybrid. (B) The color change of the solution from red to blue as a result of target-induced aggregation. (C) Monitoring aggregation process by UV-vis spectroscopy or simply by spotting solution on a silica support. Illustrating the positive cooperative behaviour of functionalized DNA where melting transition curve obtained via thermal dissociation of aggregates (red) is sharper than that of unmodified DNA (Black). Adapted from reference 14 with permission.

Figure 1-3 Melting curve of DNA hybridization. Illustrating the non-cooperative situation ($D=0$), positive ($D<1$) and negative ($D>1$) cooperativity. Positive cooperativity results in a sharper melting transition, whereas negative cooperativity generates a broader melting transition as compared to non-cooperative situation. Adapted from reference 18 with permission.

Figure 2-1 Examples of toehold mediated strand displacement reaction in DNA nanotechnology. (a) illustrates the underlying mechanism of this displacement reaction where a short single-stranded overhanging region (a toehold) of DNA colocalizes another complementary strand which displaces prehybridized strands through a branch migration process. (b) A demonstration of DNA machinery (tweezers) that could be repeatedly cycled between an open and a closed state via two specific ssDNA molecules. (c) The potential of using toehold mediated strand displacement reaction in logic circuits (specifically AND gates) where output C is produced only if both A and B are present. Adapted from reference 31 with permission.

Figure 2-2 Impact of surface DNA density on the aggregation kinetics and binding properties. Herein, legends denote the number of strands/AuNP as the prefix, followed by the sequence name. Plots a, b and c show three sets of plots with surface Seq. 2 density fixed to 260, 202 and 173 strands/AuNP, respectively. In each of these plots, the Probe density is varied from 121 to 220 strands/AuNP and their aggregation kinetics and binding properties are determined by monitoring extinction at 526 nm over time. Similarly, data is reorganized in plots (d-f) to visualize the impact of Seq. 2 surface density on the aggregation process with fixed probe surface density. Plot (g) summarizes the impact of surface Probe density on the hybridization transition time (T_h , minimum of the first derivative to the aggregation curve) with Seq. 2 density kept constant.

Figure 2-3 Impact of the surface density of DNA on the melting profile, hence on thermodynamic and kinetic properties of these nanoaggregates. Change in the extinction at 526 nm is plotted against the temperature to generate melting curves. (a and b) representative melting curves for nanoaggregates where the surface density for Seq. 2 was varied while surface density of Probe was

kept at 220 and 154 strands/NP, respectively. (c and d) show the first derivative plots of the fits shown in a and b, respectively. Likewise, e and f are melting curves, and g and h are first derivatives plots for nanoaggregates where Probe density is varied but Seq. 2 is fixed. T_m indicates the mid-point in the change of extinction of the sigmoidal transition curve

Figure 2-4 A diagram showing the method used to characterize the asymmetry of the first derivative curve.

Figure 2-5 The impact of surface DNA density on the thermodynamic and kinetic properties of target-induced disassembly of nanoaggregates. The disassembly analyses were carried out with the target concentration of 206 nM in a neutral pH buffer (0.01 M PB, 0.3 M NaCl, and 0.01 % SDS). Change in the extinction at 526 nm over time is plotted to produce disassembly profile. a, b and c show sets of nanoparticles where the Probe surface density was fixed (220, 143, and 121, respectively) while varying Seq. 2 surface densities (260, 202 and 173 strands/AuNP). Plots in d, e and f show the first derivatives of the fitting curves from a, b, and c, respectively. Similarly, the same data was reorganized in figures (g-l) to elucidate the impact of varying the surface density of Probe with constant Seq. 2 density.

Figure 2-6 The impact of surface DNA density on the rate of hybridization of fluorescently tagged target. Quenching of fluorescently labelled target via FRET was monitored over time to determine the rate of hybridization of target to the Probe sequence. Unaggregated AuNPs (orange and brown) are also analyzed for comparison.

Figure 3-1 Illustration of discrete NP dimer structures as a plasmon ruler and as a sensing platform. (a) Design of the interparticle ssDNA tethering in a plasmon ruler by means of thiol-Au bonding on one end and a highly specific Streptavidin-Biotin binding on the other end. (b) Representative scattering spectra of AuNP (green) and AuNP pair (orange) revealing a spectral shift of 23nm due to plasmon coupling. Adapted from reference 4 with permission. (c) a schematic of a stem-loop DNA-linked NP dimer as a sensing motif (top) and a geometrical extension of dimer upon hybridization of target strand (bottom). (d) Results generated via scheme (c) revealing the sensitivity and dynamic range of the dimer motif. An exponential relation is observed between the fractional shift and the target (miR-210) concentration. Inset shows calibration curve on a logarithmic scale. Adapted from reference 3 with permission.

Figure 3-2 A plasmonic biosensor based on the disassembly of surface-anchored core-satellite nanocluster. (a) Representative SEM images of assemblies with 1, 2 and 3 layers of satellite (30 nm) AuNPs on a 60 nm core AuNP. (b) The sensing via disassembly of the nanoaggregate into individual satellite particles in the presence of the target is illustrated here along with the concomitant decrease in scattering intensity shown in DF images. (c) Calibration curve and tunability of the sensing platform is depicted in the plot where different sized cluster expressed different dynamic performance. Inset in (c) shows the linear relationship between the scattering intensity and the log of target concentration (d) The setup for the direct detection of ATP from lysed adherent cells which were in close contact with the plasmonic assemblies. Adapted from reference 59 with permission.

Figure 3-3 A reaction mechanism for the PEGylation of the amino-modified surface followed by acylation of sterically shielded amino groups to achieve an effective surface passivation. Primary

amines on the substrate react with bulky mPEG ester molecules by nucleophilic attack at slightly basic pH which immobilizes mPEG on the substrate and releases N-Hydroxysuccinimide (NHS) as by-product. Passivation can further be improved by acylation of sterically shielded amino groups via similar mechanism using Sulfo-NHS-acetate which generates Sulfo-NHS as by-product.

Figure 3-4 A diagram describing the layout of a typical inverted DF microscope. The white light is focused on the substrate where some of the incident gets scattered by the nanoassemblies and is collected by the objective lens. The output signal is directed to the eye-piece, charge-couple device (CCD) camera for imaging and to the spectrometer for measurement of spectrum.

Figure 3-5 A comparison of DF images of the samples during layer-by-layer assembly using different core sizes (60 nm and 100 nm) and with satellite particle bearing varied surface density of Probe. DF images (a-d) represent core-satellite assemblies constructed using 60 nm AuNP core and 30 nm satellite AuNPs bearing maximum surface density of DNA. DF images (e-i) represent core-satellite assemblies formed as in (a-d) but with 100 nm core AuNP. DF images (j-l) represent a two layer nanoassembly formed as in (a-c) but with 121 Probe/AuNP DNA density for the first layer. Plot (e) summarizes the change in scattering intensity with respect to the number of layers of core-satellite nanocluster formed by varying surface density of DNA. Scale bar = 10 μ m in all DF images. Error bars: Std dev (n=100).

Figure 3-6 The impact of surface density of DNA on the kinetics of target-induced disassembly of surface-bound nanoassemblies with an excess amount (1 μ M) of DNA-210 is illustrated here. Plot in (e) summarizes the rate of disassembly (decay of scattering intensity) overtime. Four combinations of satellite particles bearing varied surface density of DNA were investigated in this study, as illustrated in figure (a-d). The surface density of DNA, number of layers, composition of each layer and the NaCl content are all captured in the legends of (e). Diluting the surface DNA density were generally observed to enhance the disassembly rate even at high NaCl content.

Figure 3-7 The calibration curves for the quantification of DNA-210 and miR-210. DF images of nanoparticle assemblies at various concentrations of target after incubating for 1h. are shown in (a). (b) shows the relationship between scattering intensity and the target (DNA-210 (red) or miR-210(black)) and target concentration. (c) reveals a linear relationship between scattering intensity and the log of target concentration. Scale bar = 10 μ m for DF images. Note: Different NaCl content was required for these two targets. Fitting equation in (c) - DNA-210: $y = -64.2x + 277.7$ ($R^2 = 0.997$), miR-210: $y = -78.6x + 304.8$ ($R^2 = 0.986$). Error bars: std dev (n=3).

Figure 3-8 DF images and scattering intensities of core-satellite nanoassemblies before and after they are exposed to hypoxic and normoxic cell lysate. DF images of sensors before and after exposure to cell lysate from normoxic cells (a), from hypoxic cells (b). (c) shows nanoassemblies formed by using scrambled DNA sequences before and after exposure to hypoxic cell lysate. (d) summarizes the scattering intensity before and after exposure to their corresponding cell lysate. Error bars: std dev (n=51). Scale bar in DF images = 10 μ m

Figure S-1 Monitoring the LSPR peak by UV-Vis spectroscopy during the aggregation of AuNPs with varied surface density of DNA in solution-phase. Initially, the AuNPs exhibit a sharp peak at

526nm which redshifts and broadens as the aggregation proceeds. Arrows indicate the progression of aggregation over time.

List of Equations

Equation 2-1	A five-parameter logistic equation	
	$Y = A1 + \frac{A2-A1}{(1+10^{(x0-x)*p})^s}$.35
Equation 2-2	Symmetry factor = $S = \frac{C-A}{2(B-A)}$	37

List of Schemes

- Scheme 2-1** The mechanism of aggregate formation and the disassembly of AuNPs. (a) A representation of the interparticle linkage that occur via hybridization of the β domain of the Probe sequence with the β^* domain of the Seq. 2. (b) the γ^* domain (blue) of the target (DNA-210) hybridizes with γ toe-hold domain (blue) of the Probe sequence to initiate the toe-hold strand displacement event, and finally (d) the strand migration of the target strand displaces DNA Seq. 2 resulting in disassembly of the AuNP clusters. 25
- Scheme 2-2** An illustration of the method used to determine the DNA loading on AuNPs. Briefly, AuNPs were functionalized using the pH-assisted DNA conjugation followed by salt aging steps. Then, washed particles were etched with KCN and the free DNA strands were stained and computed using fluorescence microscopy. 26
- Scheme 2-3** A depiction of the method employed to determining accessibility of immobilized DNA on 30nm AuNP. Briefly, an excess amount of fluorescently tagged target strands were annealed to the DNA functionalized AuNPs. AuNPs were washed and then etched with KCN to compute hybridized target by using fluorescence microscopy. 28
- Scheme 3-1** The mechanism of the sensing platform based on the disassembly of core-satellite nanoassemblies via toe-hold mediated strand-displacement reaction is depicted here. (a) The layer-by-layer assembly of satellite AuNPs around a large core nanoparticle disassembles when target is introduced to it. (b) A representation of the interparticle linkage that occur via hybridization of the β domain of the Probe sequence with the β^* domain of the Seq. 2. (c) the γ^* domain (blue) of the target (DNA-210) hybridizes with γ toe-hold domain (blue) of the Probe sequence to initiate the toe-hold strand displacement event, and finally (d) the strand migration of the target strand displaces DNA Seq. 2 resulting in disassembly of the AuNPs. 59
- Scheme 3-2** The layer-by-layer DNA self assembly approach to fabricate a core-satellite nanoassembly on a substrate. The core (60 nm or 100 nm AuNP) is first deposited on a silanized glass substrate which are then functionalized with thiolated Seq. 2 strands. Then the substrate is passivated with mPeg-SVA and Sulfo-NHS-Acetate for downstream manipulations. A large excess of Probe-functionalized satellite particles (30 nm AuNP with desired surface density) are then allowed to self assemble on the core via DNA hybridization. Then Seq.2-functionalized satellite particles are introduced in large excess to self-assemble into second layer by hybridizing with the Probe sequence. This cycle can be repeated to achieve desired number of layers. 60

List of Abbreviations

2D	Two dimensional
3D	Three Dimensional
5PL	Five-Parameter logistic equation
A.U	Absorbance Unit
APTMS	Aminopropyltrimethoxy silane
ATP	Adenosine Triphosphate
AuNP	Gold Nanoparticle
BSPP	Bis(p-sulfonatophenyl)phenyl phosphine dihydrate dipotassium salt
CCD	Charge-Coupled Device
DF	Darkfield
DMSO	Dimethyl sulfoxide
DNA	Deoxyribonucleic Acid
DNA-AuNP	DNA-Functionalized Gold Nanoparticles
dsDNA	Double-stranded DNA
EM	Electromagnetic
FRET	Förster Resonance Energy Transfer
FWHM	Full Width at Half-Maximum
HEPES	4-(2-hydroxyethyl)-1-piperazineethanesulfonic acid
K_d	Dissociation Constant
LOD	Limit of Detection
LSPR	Localized Surface Plasmon Resonance
miR-210	MicroRNA-210
mPEG-SVA	Methoxy poly(ethyleneglycol)succinimidyl valerate
NGS	Next Generation Sequencing
NP	Nanoparticle
PB	Phosphate buffer
polyA	Poly Adenine
RT-qPCR	Quantitative Reverse Transcription Polymerase Chain Reaction
R²	Coefficient of determination
RNA	Ribonucleic Acid
S/N	Signal-to-Noise
SAM	Self-assembled monolayer
SDS	sodium dodecylsulfate
SEM	Scanning Electron Microscope
SNP	Single nucleotide polymorphism
ssDNA	Single-stranded DNA
T₅₀	Time required for 50% disassembly

TCEP	Tris(2-carboxyethyl)phosphine hydrochloride
T_h	Hybridization transition time
T_m	Melting transition temperature
UV-Vis	Ultraviolet–visible spectroscopy
ε_i	Imaginary part of the dielectric function
ε_m	Dielectric constant of the medium
ε_r	Real part of the dielectric function

Chapter 1. Introduction

Massive growth in the use of plasmonic nanoparticles (NPs) in biosensing has emerged in recent years due to their exceptional advantages over traditional sensing methodologies. Plasmonic NPs can be utilized as the building blocks in the bottom-up DNA self assembly approach to design a nanocluster, therefore are considered as a powerful tool for sensing applications.^[1] Both solution-based and substrate-bound sensing platforms have been exploited using plasmonic nanosensors. Discrete two-dimensional and three-dimensional nanostructures have been reported to improve the detection sensitivity of plasmonic biosensors.^[1c, 2] Many sensing methods based on plasmonic nanostructures have been developed as miniaturized and cost-effective devices for their improved stability, sensitivity, specificity, and rapid and multiplexed detection of targets. Additionally, plasmonic biosensors have vast applications in health-care, biomedical research, pharmaceuticals and environment monitoring.^[3]

1.1 General Principles of a Biosensor and of Localized Surface Plasmon Resonance

A biosensor is comprised of two components: a recognition component and a transducer. The recognition component recognizes and binds the target and ideally should have high specificity and binding affinity for the target to be successful in the medical and bioscience domain. The transducer converts the biochemical signal into a detectable electronic or optical signal and should have a high sensitivity and signal-to-noise (S/N) ratio to detect the target in complex media where there is significant background scattering. Mostly antibodies, oligonucleotides, aptamers or phages are used as biorecognition component due to their high selectivity and affinity. Plasmonic NPs are a strong candidate for a recognition transducer because they have an extremely high magnitude of molar extinction coefficients for wavelength-selective absorption and scattering due to the

phenomenon of localized surface plasmon resonance (LSPR).^[4] The phenomenon of LSPR occurs when the size of the nanoparticle is smaller than the wavelength of the incident light and is schematically displayed in Figure 1.1(a).^[5] Incident light causes the free electrons in the conduction band of the metallic nanoparticle to coherently resonate with electromagnetic (EM) radiation, thus induces a dramatic enhancement in the local electromagnetic field. Plasmonic NPs can have a molar extinction coefficient for absorption up to $10^{11} \text{ M}^{-1}\text{cm}^{-1}$. Additionally, these particles can scatter light with six orders of magnitude greater than the cross-section of a fluorescein molecule without photobleaching and photoblinking which makes these particles intense and robust transducing label for sensing applications.^[4-5] The common materials used in the production of these NPs are noble metals such as Ag and Au because their energy levels for d-d transition exhibits in the visible range. Therefore, their high absorption and scattering cross-sections allow them to be easily observed by naked eyes, spectroscopy and under darkfield (DF) microscopy which is highly desirable in sensing applications. Furthermore, due to their inertness, ease of synthesis, low toxicity, biocompatibility, ease of surface functionalization, gold NPs (AuNPs) are highly considered for sensing and for constructing nanoassemblies to enhance S/N ratio.^[2c]

1.2 Plasmonic Hybridization and Coupling

The phenomenon of plasmonic coupling occurs when two plasmonic NPs are brought in proximity to one another (a gap of less than 2.5 times the length of the short axis of the NP).^[1c, 6] The interaction of localized plasmon and the interference of electromagnetic fields generated by these NPs are believed to be the factors involved. The plasmon coupling has been explained analogously to the molecular orbital binding theory by the pioneering work reported by Nordlander

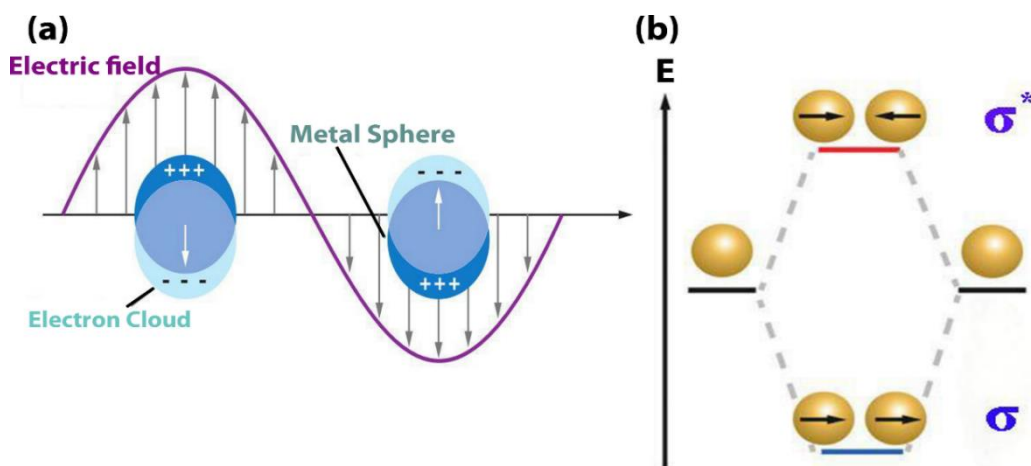


Figure 1-1 (a) Illustration of the phenomenon of localized surface plasmon resonance which occur when the electric field of the electro-magnetic radiation interacts with the free conduction electrons of a metallic NP which is smaller than the light's wavelength. Adapted from reference 5 with permission. (b) Energy diagram of plasmon hybridization showing splitting of bonding (σ) and antibonding (σ^*) plasmons as NPs are brought in proximity to each other. Adapted from reference 1c with permission.

and Halas.^[6-7] A simplest example of this interaction is the coupling of two nearby dipoles, as in the case of a symmetrical dimer. Figure 1.1(b) illustrates a schematic of the plasmon resonance hybridization of NP dimer. The dimer plasmons can be viewed as bonding and antibonding combinations. The splitting of bonding and antibonding dimer plasmon resonance increases as their interaction increases. In the case of bonding configuration (denoted as σ), the two dipole moments are in phase whereas the antibonding configuration (denoted as σ^*) corresponds to the negative parity of dipoles. In the case of identical spheres, the net dipole moment in the antibonding configuration is zero, hence cannot be easily excited by light. In contrast, the lower-energy bonding configuration is strongly coupling to the incident light. Since, the energy of the bonding plasmon decreases, a red-shift is observed in the plasmon spectra. The plasmon shift decays exponentially with the increase in particle distance.^[8] In the case of a heterodimer, the parity is broken, hence both bonding and antibonding dimer plasmons are dipole-active. Therefore, multiple peaks or a broad absorption line is observed in the absorption spectrum.^[6]

1.3 Factors Influencing the LSPR

Herein, we discuss the concept of LSPR and the factors influencing their optical signal. LSPR occurs because of the restriction to the oscillation of electrons through the internal lattice of the noble metals, therefore the frequency of the plasmon peaks strongly depends on the material, density, geometry, size, local environment and presence of other plasmonic particles in proximity. As the size of AuNP increases, the plasmon peak becomes less sensitive, broader and red-shifted. Particles do not obey Rayleigh approximation as their size becomes comparable to the wavelength of the light, hence a spectral red-shift is observed due to the retardation effect where conduction electrons of the metal do not oscillate in phase.^[4] Material of the NP is important because only material that possesses a negative real (ϵ_r) and a small positive imaginary (ϵ_i) dielectric constant are capable of supporting LSPR. The complex dielectric constant of the bulk metal is ϵ where $\epsilon = \epsilon_r + i\epsilon_i$. The condition when the EM field is enhanced is when $\epsilon_r = -2\epsilon_m$, where ϵ_m is the dielectric constant of the surrounding medium. Therefore, the composition of the NP and the dielectric constant of the local environment both dictate the frequency at which LSPR is observed. A spectral red-shift is observed when dielectric of the environment increases because of the accumulation of polarization charges on the dielectric that weakens the restoring force within NP.^[4]

1.4 DNA Functionalized AuNP in Sensing Applications: Solution-Based Biosensing and Colorimetric Assay

Traditional LSPR-based biosensing techniques are based on the sensitivity of the plasmonic frequency to the change in local dielectric constant at the NP surface and are well established for the detection of large biological molecules. This approach has many drawbacks such as high detection limits, susceptibility to false readouts, low selectivity, and inadequate S/N ratio which render them ineffective for many biological applications. Although the sensitivity and

limit of detection can be improved by modulating the NP material, size, and shape, the selectivity and specificity remain unaddressed. Amplification of signal via plasmonic coupling is often utilized to improve the signal to noise ratio and sensitivity. One way to induce plasmonic coupling

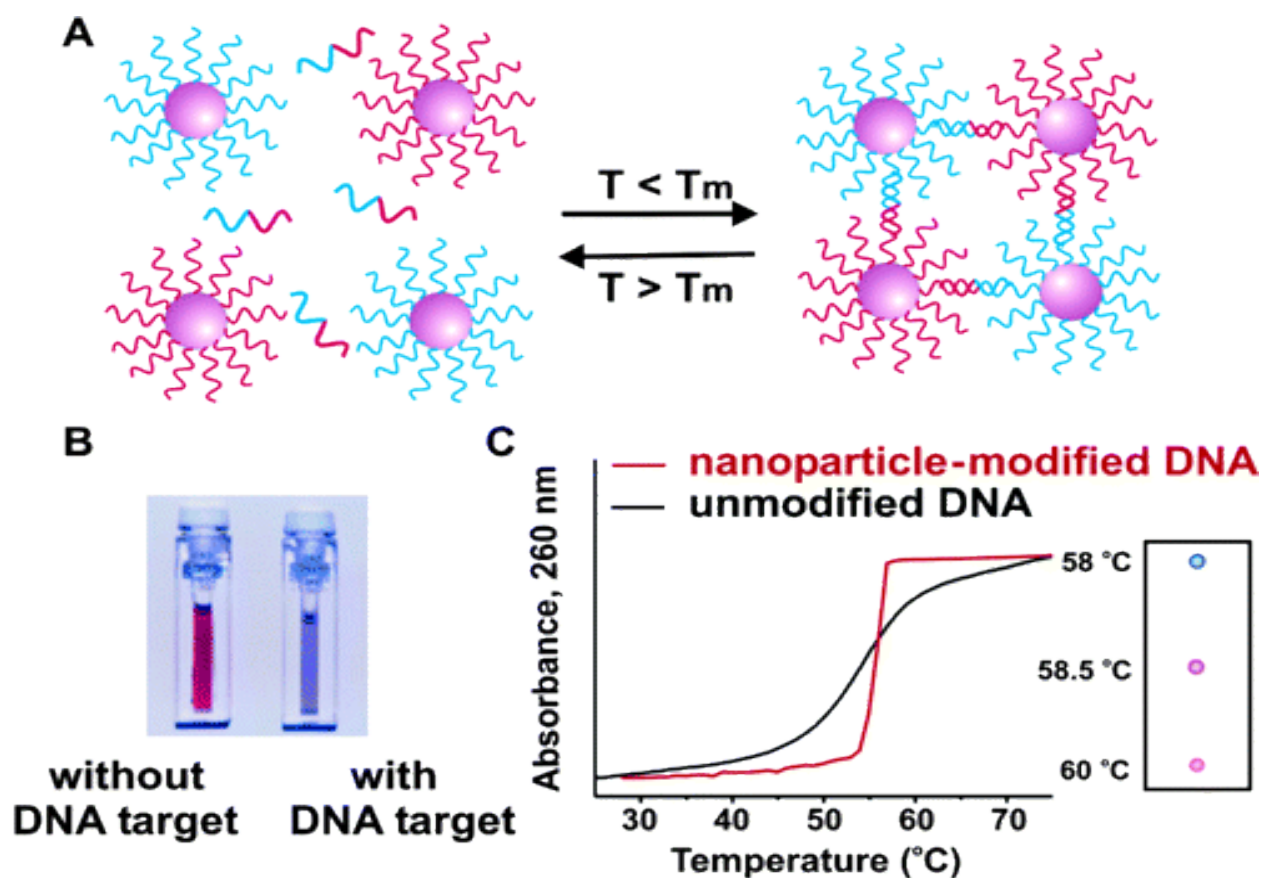


Figure 1-2 An illustration of a sensing technique based on the aggregation of NPs. (A) the mechanism of a reversible aggregation of AuNPs through a specific linker DNA strand at temperatures lower than the melting temperature of the linker-capture DNA hybrid. (B) The color change of the solution from red to blue as a result of target-induced aggregation. (C) Monitoring aggregation process by UV-vis spectroscopy or simply by spotting solution on a silica support. Illustrating the positive cooperative behaviour of functionalized DNA where melting transition curve obtained via thermal dissociation of aggregates (red) is sharper than that of unmodified DNA (Black). Adapted from reference 9 with permission.

is the formation of a nanoaggregate in solution upon the introduction of the analyte. A highly selective and sensitive colorimetric biosensing platform reported by Mirkin and co-workers^[9] for detecting oligonucleotides is presented in Figure 1-2. Figure 1-2(a) illustrates the mechanism of a reversible aggregation of AuNPs through a specific linker DNA strand at temperatures lower than

the melting temperature of the linker-capture DNA hybrid. Briefly, two sets of non-complementary DNA functionalized AuNPs were used as reporter groups and the hybridization of complementary target to both immobilized strands were used to form aggregates. Aggregation is governed by the change in optical property due to plasmon coupling of NPs upon aggregation. As these NPs aggregate into a large structure, retardation effects and multipolar plasmonic interaction (dipolar, quadrupolar, octupolar, etc.,) result in a spectral red-shifted, broad and damped plasmon, thus induces a red to the blue color change of the colloidal solution. These aggregates disassemble into individual particles upon heating above their melting transition temperature (T_m). Figure 1-2(b and c) shows the enhancement of the signal achieved through plasmonic coupling strategy which can qualitatively be analyzed visually by the naked eye or quantitatively measured by absorption spectroscopy. This strategy offers an improved S/N ratio and lower detection limits. Another crucial observation in Figure 1-2(c) is that the melting profile of the DNA immobilized on the AuNP is dramatically sharper than that of the unmodified DNA. Due to this sharp melting curve, the sensor demonstrated high specificity as it was able to discriminate between single nucleotide mismatch sequences upon controlling the temperature of the reaction.^[10]

1.5 Factors Influencing the Behavior of DNA on AuNP

There are mainly three factors controlled by DNA density that can influence the aggregation and disassembly processes of DNA-AuNPs. Firstly, the DNA density directly controls the number of DNA links at the interparticle junction. Higher DNA links at the interparticle space can synergistically enhance the apparent affinity through the phenomenon known as avidity. Avidity occurs in high DNA density scenarios where even one hybridization event at the interparticle space can potentially align other hybridizable strands at the interparticle space in a precise orientation and proximity, thus promoting their hybridization efficiency. Additionally, multiple hybridization

events between the particles will keep any newly dissociated strands in proximity against diffusion and therefore further enhance DNA duplex stability. The density of these functional strands also plays a critical role in the enhancement of this apparent affinity because these strands need be sufficiently close together and properly aligned with each other due to limited lateral bending of densely packed DNA strands on the AuNP surface.^[11] The second factor is attinebility. Attinebility is a recently coined term for a phenomenon where high local concentration of ligands (i.e., DNA on AuNP) increases the retention of the target strand in the proximity of the AuNP surface and facilitates a faster rebinding.^[12] The probability of target diffusing away from the particle surface after a transient dissociation event is lower when the density of DNA strands is higher, leading to a smaller dissociation rate constant. Avidity and attinebility result in cooperative binding properties of densely functionalized DNA-AuNP, which consequently controls the aggregation and disassembly. Lastly, modulating the surface DNA density by replacing functional DNA strands with diluent DNA strands impacts the repulsive forces between nanoparticles. The work presented on the aggregation and disassembly of DNA-AuNP in this thesis will be discussed in relation to the three factors mentioned above.

In general, cooperativity is classified as positive when the binding affinity of subsequent binding events is higher than the previous binding, or

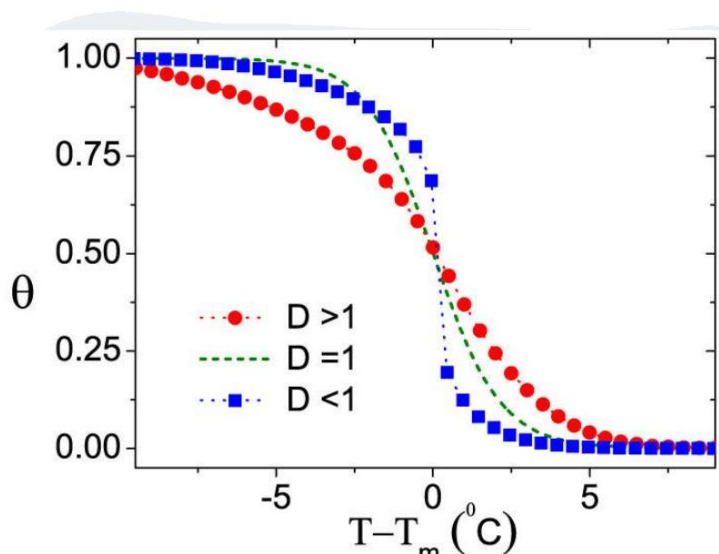


Figure 1-3 Melting curve of DNA hybridization. Illustrating the non-cooperative situation ($D=0$), positive ($D<1$) and negative ($D>1$) cooperativity. Positive cooperativity results in a sharper melting transition, whereas negative cooperativity generates a broader melting transition as compared to non-cooperative situation. Adapted from reference 14 with permission.

negative when the subsequent binding affinity is lower. In the noncooperative scenario, the binding is identical for all molecules.^[13] Commonly, the hybridization cooperativity in the thermal melting of DNA-AuNPS is measured by analysing the full width at half-maximum (FWHM) of the first derivative peak, where positive cooperativity leads to a narrower FWHM due to sharp transition and negative cooperativity results in broader FWHM due to retarded transition (Figure 1-3).^[14] To minimize negative cooperativity, spacers are used which are conjugated between probe and surface in order to control DNA density and to raise the DNA probe from the surface, thus improving the accessibility of immobilized strand to hybridization.^[15] Additionally, diblock oligonucleotides have been designed where the poly-adenine (polyA) block is used to tune the surface density and to keep the upright orientation of functionalized strands to improve accessibility. Due to the strong binding of polyA block on AuNP, the length of polyA can be modified to tune the surface coverage of strands.^[16]

1.6 Overview of the Target and Comparison of Different Sensing Platforms

MicroRNAs are small non-coding ribonucleic acid (RNA) molecules involved in the regulation of gene expression, hence play critical roles in physiological and pathological processes. Their expressions are altered in various diseases and tumors; therefore, the examination of their expression profiles can reveal information on their regulation and function.^[17] It is predicted that alteration in the miRNA expression happens in bodily fluids and tissue before conventional biomarkers; therefore, the disease can be detected before significant tissue damage has occurred. The presence of miRNAs not only in tissues but also in extracellular fluid, along with their altered expression in various pathological conditions has implicated miRNAs as promising biomarkers, thus their detections demand has been on the rise. To detect miRNA in such a low quantity with only a few folds of variation in their expression requires a rigorous method that does not have

many steps involved in their detection. Profiling of multiple miRNA species and their differential expression pattern is correlated with physiological status to understand disease pathogenesis. Profiling of miRNA is a multi-step process involving the sample collection and extraction of miRNA species followed by their quantification and profiling. Although several methods have been established to quantify them, a method for their high-throughput detection is still lacking.^[18] Benchmark techniques for microRNA analysis, such as microarrays, next-generation sequencing (NGS) and quantitative reverse transcription PCR (RT-qPCR) require complex handling procedures, laborious sample preparation, manipulation, and purification steps.

RT-qPCR has a better limit of detection, sensitivity, and selectivity than microarray technologies for miRNA profiling, but the RT-qPCR method is limited in the context of multiplexed detection as compared to microarrays. There are high-throughput platforms commercially available that use RT-qPCR, such as customizable microfluidic cards or plates. Although microfluidic cards are flexible but are still limited in the number of miRNAs that can be examined compared to microarrays. Additionally, during the sample collection from blood, anticoagulants such as EDTA, citrate or heparin are commonly used to profile miRNA. These anticoagulants have a tendency to inhibit enzyme activities that are used in PCR and NGS platforms thus requires additional steps for their quantitative removal from the sample in order to achieve accurate miRNA yield.^[19] Moreover, during sample collection, the presence of hemoglobin and lactoferrin can also inhibit the subsequent RT-qPCR. Thus, these platforms suffer from inadvertent contamination.^[19b] The sensing platform needs to be highly specific and selective towards the desired miRNA to minimize the number of steps involved in their detection. Currently, most methods do not offer such a high selectivity hence require miRNA extraction methods, such as the use of phenol-chloroform-based extraction technique followed by their precipitation with

isopropyl alcohol or chromatographic separation from the complex medium. Due to their smaller size, miRNA recovery requires an overnight precipitation step at low temperatures followed by the long pelleting time. Conventional methods also suffer from high cost and lack of portability. A range of techniques has been developed to overcome the challenges of miRNA profiling. For example, miRNA profiling and expression detection by RT-qPCR are mostly performed using either TaqMan® or SYBR green methodologies, however, these methods are labor-intensive, requires expertise and is not cost effective because additional equipment is required to use these platforms. Although the quantification of miRNA expression to obtain the absolute number of miRNA by RT-qPCR can be performed, it is impractical to use this platform to profile a large number of miRNA species. Due to the lack of an invariant endogenous control and unreliability of exogenous control for normalization, determination of the absolute quantity of miRNA using RT-qPCR is limited.^[19b]

As mentioned above, the multiplexed detection of miRNA expression is achievable using microarray methodology. Microarrays have a remarkable advantage due to their comprehensive coverage and customizability, thus making them a flexible and versatile tool. However, unlike RT-qPCR, microarrays cannot be used for absolute quantification and they offer lower sensitivity and specificity than RT-qPCR.^[20] Additionally, these platforms are highly sophisticated, costly and require technical specialization. The limit of detection for microarray-based platforms is high and usually requires the sample to be concentrated within a maximum volume of 3-8 μ L. These methods also require additional steps such as labeling of the miRNA.^[19b]

Next-Generation Sequencing is considered the most promising technology for miRNA analysis because it offers important advantages such as the ability to generate comprehensive and definitive analyses. NGS does not require knowledge of target miRNA nor it requires specific

primers or probes. Additionally, NGS is an extremely sensitive technique with a large dynamic range than microarrays. This technique can also provide a relative expression for miRNAs, highly specific and can generate a profile of all small RNAs in the sample.^[19b, 21] However, this platform has some inherent limitations, such as inability to generate absolute quantification of miRNA. NGS also requires miRNA extraction and purification steps to eliminate factors that can influence the activity of enzymes involved in NGS. NGS suffers from the high cost of profiling miRNA populations and from the advanced data analysis requirement which requires computational infrastructure and bioinformatics support.^[19b] Above mentioned conventional laboratory methods are considered the mainstream procedures applied for the determination of miRNAs; however, recent progress in the miRNA sensing has emerged in the fields of electrochemical, optical and nanoparticle-based biosensing platforms.^[22] Electrochemical biosensor transduces a molecular recognition event into a detectable and quantifiable electrical signal. There are four main types of electrochemical biosensors based on signal transduction types: amperometric, potentiometric, impedimetric and ion charge effect. These platforms are based on the reduction or oxidation of a molecule to generate a signal.^[23] Although comparable molecular techniques can be used in both optical and electrochemical detection resulting in similar detection limits and dynamic ranges, electrochemical sensors are advantageous in terms of scalability and sensitivity. However, most of the electrochemical methods for miRNA sensing require multiple sample-processing steps such as purification of the sample to reduce the background noise and the direct labeling steps to introduce the source for the electrochemical signal to improve the signal to noise ratio and sensitivity. Some strategies are known to omit the labeling steps such as sandwiching the desired miRNA between a surface-bound capture strand and labeled signal probe, but these techniques are not promising for miRNA detection because of the low concentrations of miRNA in the sample and short lengths of miRNA preventing simultaneous hybridization of both capture and signal probes to the same

miRNA strand. Additional strategies to avoid sample labeling steps such as guanine oxidation or the use of electroactive intercalators have been proposed and used, but these strategies suffer from the low specificity and selectivity due to their inability to distinguish between miRNAs comprising single base mismatches. Another limiting factor for the development of electrochemical genosensors is their sensitivity because the amount of DNA/RNA is below femtomolar levels, but when combined with amplification strategies, these sensors have proven to be feasible.^[24] Considerable efforts have been made to develop amplification techniques to improve the sensitivity of electrochemical biosensors, such as isothermal amplification of nucleic acids.^[25] However, the high cost of enzymes, complicated labeling procedures, and time-consuming process resist their broad applications in clinical and diagnosis and biomedical research. Nanomaterial-based electrochemical and optical miRNA sensing platforms have advanced sensing performance due to their excellent characteristics, such as large surface area, active binding sites, and enhanced catalytic and conductivity properties. Additionally, nanomaterials offer many physical and chemical advantages by serving as an electrode material, carrier of signal elements to assist complex hybridization reaction, and chemical reaction catalyst.^[24] Yet, there are significant challenges in the application of nanomaterial-based electrochemical sensing of miRNA due to many factors: (1) methods still require purification of the complex matrix to eliminate non-specific adsorption of co-existing species on the nanomaterial surface, (2) highly controlled synthesis of nanomaterials is required to minimize batch to batch variation.^[26] Nanomaterial-based electrochemical sensors still suffer from moderate specificity, moderate selectivity, high background noise in complex media.

Fluorogenic miRNA sensing platforms based on Förster Resonance Energy Transfer(FRET), such as molecular beacons based on organic dye or gold nanoparticles, use fluorescence signal

generation and quenching to selectively detect miRNA with considerable sensitivity. Molecular beacons are highly unique oligonucleotides which are designed as stem-loop DNA oligonucleotide probes bearing the anti-target sequence. The termini of the probe sequence are conjugated to a fluorescent dye and its suitable quencher. The specific binding of the target to the probe causes dye and quencher to separate which elicits a fluorescent signal. This design allows the direct and selective sensing of the miRNA and eliminates the need to remove other sequences in the solution and the excess amount of probe sequences.^[27] Therefore, miRNA assay can be performed without the need for enzymes or amplification steps. However, these platforms are susceptible to false readouts from degradation and in many cases offer poor selectivity and specificity for miRNA detection. Additionally, molecular beacons suffer from incomplete quenching and inability to distinguish Single nucleotide polymorphisms (SNPs), pre-miRNA and mature miRNA.^[28] The sensitivity and S/N ratio of this platform is compromised in complex media due to high background fluorescence and autofluorescence.^[29] On top of that, fluorescence molecules suffer from photobleaching and short shelf life. The extinction cross-section and quantum yield of fluorescently labeled molecules is insignificant compared to that of plasmonic NPs.^[4] Therefore, compared to organic dyes and fluorescent proteins, NPs are more appealing for the direct detection applications with minimal need of sample enrichment and amplification, thus minimizing the procedural complexity and makes the technique more accessible and versatile to be adapted into portable systems. Moreover, similar to electrochemical sensors, plasmonic biosensors based on 2-D or 3-D structures nanomaterials have the potential to demonstrate outstanding sensitivity, rapid analysis with easy and cost-effective operation.

Here we briefly introduce our sensing platform which is based on the disassembly of core-satellite nanocluster which is bound to the glass substrate to obtain highly regulated and uniform

sizes. The particles are brought together spatially via hybridization of surface DNA on the AuNPs. The linkage can be displaced by the target (DNA-210) strand and cause disassembly of the aggregates. In the second chapter of the thesis, the impact of the surface density of DNA and environmental factors is explored in depth to understand their contribution towards cooperativity and accessibility. The fundamental understanding from chapter two is then exploited in chapter three to optimize the kinetic and thermodynamic properties of the sensing platform which can allow for the oligonucleotide detection. The ability to regulate kinetic and thermodynamic properties allows one to further regulate the dynamic performance of the sensor. Finally, the concluding chapter provides an outlook on the ongoing and future work of this platform and discusses additional possibilities offered by the sensor that still need to be explored.

To demonstrate proof-of-concept for the sensing capacity of our platform, miR-210 and its DNA analogue (DNA-210) were explored. miR-210 is a crucial biomarker for a hypoxia-related pregnancy disease known as preeclampsia.^[30] Preeclampsia is a major contributor to maternal mortality and morbidity worldwide. Elevated expression of miR-210 in the placenta has been reported to be linked with preeclampsia.^[31] Hypoxia is known to markedly increase the expression of miR-210 in the human trophoblast cell line, HTR8/SVneo.^[31-32] To study the impact of hypoxia in vitro, Cobalt chloride (CoCl₂) is used to induce and mimic hypoxia in HTR8/SVneo cell line.^[33]

Chapter 2. Implications of Altering the Surface DNA Density of AuNPs on the Thermodynamic and Kinetic Properties of Nanoaggregate Formation and Their Disassembly Via a Toe-Hold Mediated Strand Displacement Reaction.

2.1 Introduction

2.1.1 Toehold Mediated Strand Displacement Reaction in DNA Nanotechnology

Composition diversity, programmability and highly predictable hybridization of DNA strands have enabled the construction of a diverse set of nanostructures and nanodevices. DNA nanotechnology relies mainly on the non-covalent interactions to design higher-order assemblies that perform novel functionalities. DNA nanotechnology has shown interesting static and dynamic properties which attracted them for engineering various molecular devices^[34], such as circuits^[35], catalytic amplifiers^[36], autonomous molecular machineries^[37] and sensing platforms^[38]. Yurke *et al.*^[39] introduced the concept of toe-hold mediated strand-displacement reactions (Figure 2-1a) in which a short single-stranded overhanging region (a toehold) of DNA colocalizes another complementary strand which displaces one or more prehybridized strands through a branch migration process. Toehold domain offers an engineering control over the efficiency and reliability of the strand displacement reaction.^[34, 40]

A glimpse at the potential of toe-hold mediated strand displacement reaction in DNA nanotechnology is given in Figure 2-1 where the use of these specialized reactions in molecular switch (Figure 2-1b) and logic circuits (Figure 2-1c) is illustrated. The pioneering work by Yurke is represented in Figure 2-1b where they demonstrated a set of DNA tweezers that could be repeatedly cycled between an open and a closed state via two specific ssDNA molecules (F and \overline{F}). They demonstrated how DNA molecules can act as fuel for nanomachinery. The toe-hold mediated strand-displacement reaction has been explored for sensing based on FRET as shown in

Figure 2-1b, where they are used to investigate the interaction between chemically active components if attached to the ends of the tweezer is also demonstrated. Figure 2-1c reveals another importance of sequence recognition and strand displacement reaction in the designing of DNA-based digital logic circuits^[41]. Here an AND gate is illustrated where single-stranded nucleic acids are used as inputs and outputs. An output C is produced only if both A and B are present.

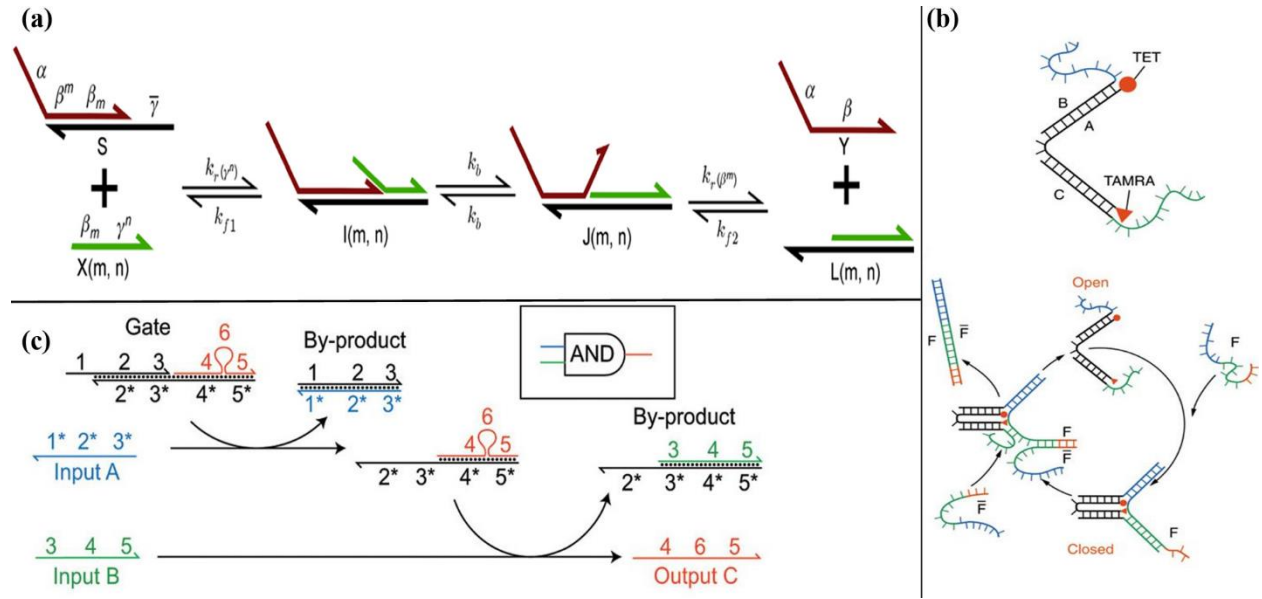


Figure 2-1 Examples of toehold mediated strand displacement reaction in DNA nanotechnology. (a) illustrates the underlying mechanism of this displacement reaction where a short single-stranded overhanging region (a toehold) of DNA colocalizes another complementary strand which displaces prehybridized strands through a branch migration process. (b) A demonstration of DNA machinery (tweezers) that could be repeatedly cycles between an open and a closed state via two specific ssDNA molecules. (c) The potential of using toehold mediated strand displacement reaction in logic circuits (specifically AND gates) where output C is produced only if both A and B are present. Adapted from reference 40 with permission.

While the toehold-mediated strand displacement reaction has been studied extensively in the solution phases to reveal the design requirements of the α , β and γ domains (referring to Figure 2-1a), the kinetics and thermodynamics of the reaction when taking place on surface can further be subjected to many factors such as molecular crowding, strand length, local ionic content, and density.^[42] Surface-immobilization spatially localizes molecular components which are typically more densely packed than their solution-phase counterparts. DNA hybridization is also known to

proceed more slowly on surfaces than in solutions.^[43] Secondary structure of the DNA can either be stabilized or destabilized as a result of crowding depending on the conformation of neighbouring molecules.^[44] Additionally, due to high density, one hybridization event on the surface can sterically and electrostatically retard the binding of the subsequent binding events, hence only a fraction of total surface-bound DNA can undergo hybridization effectively.^[45] Moreover, the density and the relative length of the DNA compared to neighbouring strands/molecules impacts the target accessibility of the DNA, thus further limits the hybridization efficiency dramatically.^[46]

2.1.2 Objective

Herein, we present a method for modulating the kinetics and thermodynamic properties of aggregation and disassembly processes of DNA-functionalized nanoparticles. Specifically, we study the influence of varying surface density of DNA on the toehold strand-displacement reaction on nanoparticle surfaces. The hybridization of DNA-AuNP yield aggregates which then disassemble via a strand-displacement reaction by the target sequence. The object is to modulate attainability and cooperativity to deduce the aggregation kinetics, the melting temperature and the target-induced disassembly of these nanoaggregates. A dramatic decrease in the initiation time and increase in the rate of disassembly are achieved by optimizing the surface density. Our work provides insight into the strand-displacement reaction on nanoparticle surfaces that underpins various sensing and DNA-driven nanomachine applications.

2.2 Experimental

2.2.1 Reagent, Materials and DNA

Colloidal AuNP solutions (spherical 30-nm, 60-nm and 100-nm diameter) were purchased from BBI Solutions. Glass coverslips (25mm x 25mm x 0.17mm) were purchased from VWR. Illustra NAP-5 columns were purchased from GE Healthcare Life Sciences, and CoverWell perfusion chambers (8 chambers, ports diameter 1.5mm, 9 mm in diameter x 0.6 mm depth) were purchased from Grace Bio-Labs. Anhydrous ethanol and 2-propanol were purchased from Commercial Alcohol, and water used for all experiments were purified (deionized to 18M Ω) using a Millipore system. Methoxy poly(ethyleneglycol)succinimidyl valerate (mPEG-SVA, MW = 5000 g/mol) was purchased from Layson Bio Inc. 1-acetyloxy-2,5-dioxopyrrolidine-3-sulfonic acid (sulfo-NHS-Acetate, Mw = 259.17g/mol) was purchased from proteoChem, SYBRTM Gold nuclein acid gel stain (10,000x concentrated in DMSO) was purchased from Thermo Fisher Scientific All other chemicals were purchased from Sigma Aldrich, Bis(p-sulfonatophenyl)phenyl phosphine dihydrate dipotassium salt (BSPP), including Tris(2-carboxyethyl)phosphine hydrochloride (TCEP), glacial acetic acid (CH₃CO₂H, 99.85%), sodium dodecylsulfate (SDS), sodium chloride (NaCl), sodium azide (NaN₃), 3-aminopropyltrimethoxysilane (APTMS), sodium phosphate monobasic monohydrate (NaH₂PO₄·H₂O), sodium phosphate dibasic (NaH₂PO₄), 4-(2-hydroxyethyl)-1-piperazineethanesulfonic acid(HEPES), Citric Acid (HOC(COOH)(CH₂COOH)₂), Sodium Citrate dihydrate (HOC(COONa)(CH₂COONa)₂ · 2H₂O), sodium carbonate (Na₂CO₃), TritonTM X-100, Potassium Cyanide (KCN) and sodium bicarbonate (NaHCO₃).

All oligonucleotides were purchased from Integrated DNA Technologies. The disulfide bond of thiolated oligonucleotides were cleaved using reducing agent tris(2-carboxyethyl) phosphine (TCEP) and desalted using Nap-5 columns prior to use. DNA sequences are listed below (underlined region is complementary to each other):

Functional DNA:

Probe: 5'- /5ThioMC6-D/AAA AAT CAG CCG CTG TCA CAC GCA CAG-3'

Seq.2 (complementary to seq.1): 5'-/5ThioMC6-D/AA AAA AAA AAGCAGG TGA CA – 3'

Diluent DNA

Diluent DNA: 5'-SH-(CH₂)₆-CCCAGGTTCTCT-3'

Targets:

DNA-210 (target) 1): 5'-CTG TGC GTG TGA CAG CGG CTG A-3'

miR-210 (target): 5'-CUG UGC GUG UGA CAG CGG CUG A-3'

Nanoflares: For DNA accessibility study and for solution-based fluorescence study.

Flare1 5'-CTG TGC GTG TGA CAG CGG CTG A Cy3 -3'

Flare2 5'- TCA GCC GCT GTC ACA CGC ACA G /3Cy3Sp/ -3'

2.2.2 Reducing thiolated-DNA:

The disulfide bonds of purchased thiolated-DNA sequences were first reduced with TCEP (50x excess) in 50mM acetate buffer (pH 5.2) for 1.5h. Then, the DNA sequences were purified using NAP5 desalting columns and quantitated using UV-Vis spectroscopy.

2.2.3 AuNP Cap exchange:

Using the ligand exchange method proposed in literature, the citrate capping of purchased 30 nm AuNPs was exchanged with BSPP by stirring 2 mL of particles (0.3 nM) with 2 mg BSPP overnight. Particles were then washed twice by centrifuging (5K rpm, 15 min, where 1000 g = 3900 rpm) with 5 nM BSPP and stored in 5 nM BSPP at 2-8°C.

2.2.4 Conjugation of DNA onto 30-nm AuNPs:

AuNPs were concentrated to 0.6 nM by centrifuging (10K rpm, 10 min). Depending on the required surface coverage, a predetermined ratio of functional DNA to diluent DNA (in 2x excess of maximum surface coverage of functional strand used) are mixed with about 0.6 nM satellite particles (BSPP-capped Au30). The mixture is then allowed to incubate for 15 min on a thermo-shaker (50°C, 650 rpm). Then, the pH of the mixture is lowered to 3 with 500 mM citrate buffer (pH 3) for 3min. The pH is then brought back to neutral with 500 mM HEPES (pH 7.4). While mixing on thermo-shaker (50°C, 650 rpm), the NaCl concentration is slowly (0.1 M per 20 min) increased to 0.4 M. Mixture is then allowed to incubate for 12h at 0.4 M NaCl. DNA-functionalized particles are washed three times with 0.01% SDS by centrifugation (10k rpm for 10 min) and are then stored on buffer (0.01 M PB, 0.05M NaCl, 0.01% SDS and 0.01% azide) at 4°C at 0.6 nM concentration.

2.2.5 Determining DNA Loading on Satellite NPs

The concentration of DNA functionalized AuNP was determined by performing UV-Vis analysis. Then particles were etched with 0.1 M KCN (final concentration) solution to completely dissolve. The pH of the solution was adjusted down to 8 using 1 M HCl. Then for every 90 μ L of solution, 10 μ L of 100x concentrated SYBR gold stain was added to obtain a final dye concentration of 10x. DF microscope (Nikon Eclipse, TE2000-U) was used to set up fluorescence platform where source from microscope was used to excite the stain and a portable charge coupled device spectrometer (USB2000, Ocean optics) was used to collect emission from the unknown solution. A known amount of stock solution standard was then added to the solution to construct a standard-addition calibration curve to determine the conc. of DNA in the unknown. From the conc. of AuNPs and that of DNA strands, the loading of DNA on satellite particles was determined.

2.2.6 Determining Accessibility of the DNA Immobilized on AuNPs (30-nm) for Various Surface Densities

DNA-AuNPs (0.3 nM final concentration) were mixed with their corresponding Nanoflares (DNA-210-CY3 or NF-210-2-flare for AuNPs functionalized with Probe or Seq. 2, respectively) in large excess (17 Nanoflares per functional-DNA strand) and the NaCl content of the buffer was raised to 0.34 M. Hybridization was facilitated through annealing by heating the mixture to 60°C for about 15 minute and then slowly cooling the reaction mixture down to room temperature over a period of 1h. Excess strands were washed three times with 0.35 M NaCl buffer by centrifuging (10K rpm for 10 min) to remove extra Nanoflares and were resuspended in 130 μ L buffer(0.01 M PB, 0.05M NaCl, 0.01% SDS). Then these particles were etched with 6 μ L of 1 M KCN solution for 30 min to completely dissolve particles (pH was not adjusted back to neutral). Fluorescence was monitored using a custom setup where two light collimators (Thor Labs) were set up to flank the cuvette stationed in a light protected holder. One collimator was connected to the light source (cyan light) via fibre optic cable, while the other collimator (at 90° to incident light) was connected to a portable charge-coupled spectrometer (USB2000, Oceran Optics) to collect emission from the unknown solution. A known amount of stock solution (2 μ L of 500 nM) standard was then added four times to the solution to construct a five-point standard-addition calibration curve in order to determine the concentration of DNA in the unknown.

2.2.7 Aggregation in solution

Aggregates were formed in solution by hybridizing complementary functional DNA strands immobilized on the AuNPs (with various surface DNA densities). Two sets of particles were mixed in one-to-one ratio (total conc 0.15 nM) in an aluminium micro cuvette (path length = 1 cm) held in an aluminum cuvette block. The NaCl concentration of the mixture was raised to 0.25 M NaCl in 0.01 M PB. The UV-spectrophotometer was set-up by attaching two light

collimators on each side of the cell holder. Tungsten light source was connected to one of the collimators (Thor labs), whereas the collimator was connected to a portable charge coupled device spectrometer (USB2000, Ocean optics). The UV-Vis spectrum was captured every minute until the aggregation was complete and no further change was observed on the spectrum (about 1h).

2.2.8 Thermal Disassembly of nanoaggregates in solution (melting of DNA duplexes)

When in-solution aggregation was complete, the aluminum cuvette block was wrapped with a heating tape that was controlled by a Variac. Two light collimators were attached on each side of the block. Tungsten light source was connected to one of the collimators (Thor labs), whereas the collimator was connected to a portable charge coupled device spectrometer (USB2000, Ocean optics). A thermocouple was inserted in the cuvette to monitor the temperature throughout the testing process. Temperature was increased slowly (roughly 1°C/min) using Variac and absorption spectra were obtained after every minute from room temperature until complete disassembly was observed.

2.2.9 Target-induced disassemble of aggregates in solution

Aggregates were prepared again as per section 2.2.7, to monitor disassembly with target (DNA-210). Upon aggregation, DNA-210 was added to the solution (final target concentration = 206 nM) while keeping the NaCl concentration same (0.25 M in 0.01 M PB buffer). Same setup as that used in section 2.2.8 (without heat) was employed to monitor the disassembly by capturing extinction spectra over time with an interval of 1min.

2.2.10 Disassembly using fluorescently tagged target (DNA-210-CY3)

Aggregates were prepared again as per section 2.2.7, to monitor disassembly with target (DNA-210). Upon aggregation, DNA-210-CY3 was added to the solution (concentration equivalent to 2 target strands per Probe strand) while keeping the NaCl concentration same (0.25

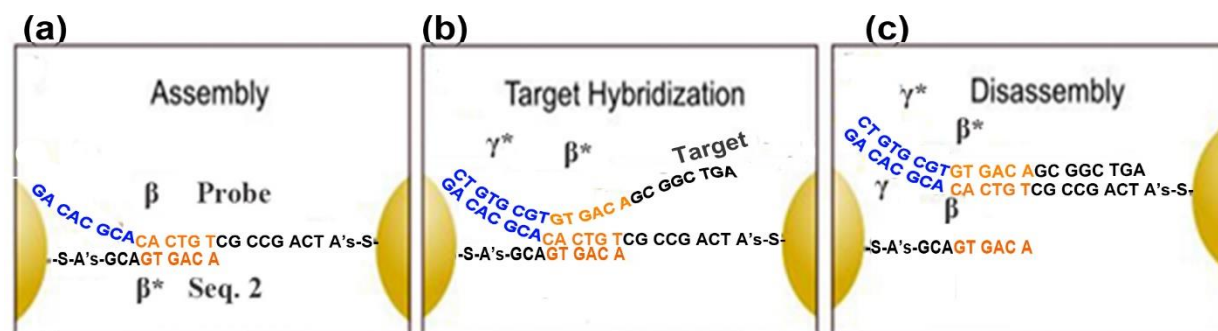
M in 0.01 M PB buffer). Same setup as that used in section 2.2.8 (without heat) was employed to monitor the disassembly by capturing extinction spectra over time with an interval of 1min.

2.3 Results and Discussion

2.3.1 Structure and Function of DNA Strands Immobilized on AuNPs in the Aggregation and Disassembly Processes.

We conducted systematic studies in which the density of DNA conjugated on the 30 nm gold nanoparticle (AuNP) surface was varied by incorporating diluent DNA during the conjugation step. As reported by Liu and co-workers, the pH-assisted functionalization of gold nanoparticle with thiolated DNA allows quantitative adsorption of different thiolated-DNA strands at predetermined ratios.^[47] Based on their reports where various oligonucleotide sequences and AuNP sizes were investigated, the surface DNA composition is comparable to the predetermined ratios of the mixture of oligonucleotides in the functionalization step. In our work, two sets of DNA-AuNP conjugates were prepared: one with the Probe sequence and the other with Seq. 2. Reversible AuNP aggregation and its disassembly were achieved by carefully designing these two DNA sequences bearing partial complementarity to each other. Nanoparticle aggregates form from the highly specific and programmed DNA hybridization events under appropriate environmental conditions.

These two DNA sequences were designed to obtain thermodynamic stability at selected buffer conditions. The Probe sequence comprises a toe-hold domain to induce disassembly via the strand displacement process in the presence of the perfect complementary target (denoted as DNA-210). The mechanisms for aggregate formation and disassembly of AuNPs are depicted in Scheme 2-1. Two sets of DNA-AuNP assemble through the hybridization of the β domain of the Probe sequence on one AuNP with the β^* domain of the Seq.2 strands on the other AuNP (Scheme 2-

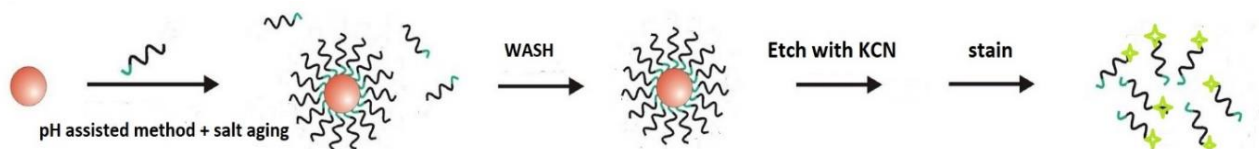


Scheme 2-1 The mechanism of aggregate formation and the disassembly of AuNPs. (a) A representation of the interparticle linkage that occur via hybridization of the β domain of the Probe sequence with the β^* domain of the Seq. 2. (b) the γ^* domain (blue) of the target (DNA-210) hybridizes with γ toe-hold domain (blue) of the Probe sequence to initiate the toe-hold strand displacement event, and finally (d) the strand migration of the target strand displaces DNA Seq. 2 resulting in disassembly of the AuNP clusters.

1a). Nanoaggregates were formed by mixing these AuNPs in buffer solution and inducing DNA hybridization by increasing NaCl content of the buffer. Once nanoclusters self-assemble by forming Watson-Crick base pairs, target DNA-210 can initiate the toe-hold mediated disassembly process because it bears higher complementarity to the Probe sequence than Seq. 2 (Scheme 2-1b). Upon hybridization, strand migration of the target then displaces Seq. 2 causing the clusters to disassemble (Scheme 2-1c) and LSPR to change. The optical properties of the nanoparticles were used to determine the extent of aggregation or disassembly process. It is essential to highlight the role of toe-hold domain in the disassembly process. The 8-mer toe-hold domain is known to drastically improve the kinetics of the strand displacement reaction. Additionally, the absence of any toe-hold domain for the reverse reaction makes it highly unfavourable for Seq. 2 to displace the target from the Probe sequence; such reverse reaction has been reported to proceed up to 6 orders of magnitude slower than the forward reaction. Hence the toe-hold mediated disassembly process should proceed towards the disassembly the nanoaggregates.^[48]

2.3.2 Determining the Surface Density of Functional and Diluent DNA on the AuNP.

To understand the impact of varying the number of strands on the AuNP surface, it is crucial to first determine the maximum number of strands that can be functionalized on AuNP surface. The applicable strands for this study were the Probe sequence, Seq. 2 and the Diluent DNA. Scheme 2-2 illustrates the method used to determine DNA loading on AuNPs, and to quantify of surface coverage. To achieve maximum loading of DNA, AuNP were mixed with a large excess of oligonucleotides during the conjugation step, followed by purification, as described in the method section (section 2.2.4). These functionalized AuNPs were then etched with 0.1 M KCN and the released DNA were stained with SYBR® fluorescent dye to quantify the surface coverage



Scheme 2-2 An illustration of the method used to determine the DNA loading on AuNPs. Briefly, AuNPs were functionalized using the pH-assisted DNA conjugation followed by salt aging steps. Then, washed particles were etched with KCN and the free DNA strands were stained and computed using fluorescence microscopy.

of the DNA on AuNP. Table 2-1 shows the maximum number of strands that bind to the surface a 30 nm AuNP. The surface coverages that were computed by this method are comparable to those reported by other research groups.^[49] Although all three thiolated DNA sequences have similar binding chemistry, their loading is significantly different. The Probe sequence has lower surface coverage (220 strands/AuNP) because it is long and forms a stable hairpin structure at high NaCl concentrations, leading to a greater lateral area occupied by the bound strands and more steric and electrostatic hindrance for the binding of subsequent strands. In comparison, Diluent DNA is most densely packed on the AuNP surface at 347 strands/AuNP because it is the shortest and does not form any secondary structure. Note, unlike the Diluent sequence strand, the Probe sequence and

the Seq. 2 acquire a Poly A chain near its binding site which has tendency to adsorb and span onto the AuNP surface, hence lowering the surface coverage.^[16]

Table 2-1 Maximum Surface DNA density determined by using Scheme 2-2 for all Surface-DNAs used in the study

DNA type	Maximum DNA density (Strands / AuNP)
Probe	220
Seq. 2	289
Diluent DNA	347

2.3.3 Strategy Employed to Modulate Surface Coverage of Functional DNA

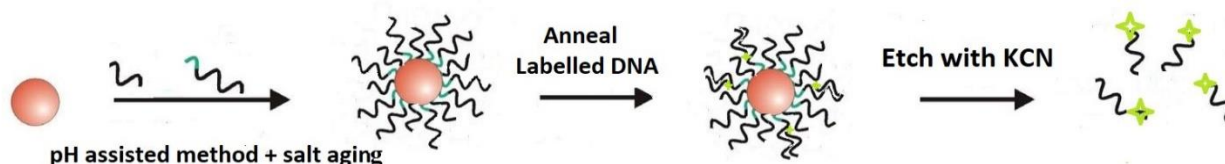
The surface density of both functional DNA strands, i.e., Probe and Seq. 2, on the AuNP surface were varied to understand their impact on the binding properties and kinetics of the hybridization process during the formation of the nanoaggregates, as well as to optimize the kinetic and thermodynamic properties of the toe-hold mediated strand displacement process on nanoparticle surface. To control the surface density of these functional sequences, Diluent DNA was incorporated during the conjugation step. The incorporation of Diluent DNA also offers other advantages, such as higher colloidal stability when the density of the functional DNA was decreased, and minimal non-specific adsorption of other molecules on the surface of AuNPs.^[50] Herein we control the number of hybridization events between AuNPs by modulating the number and the accessibility of the functional strands, thereby influencing the formation and disassembly of nanoaggregates.

2.3.4 Determining the Accessibility of Immobilized Functional DNA Strands and the Effect of Incorporating Diluent DNA on the Accessibility

Previous work has shown that only a fraction of the oligonucleotides on AuNP is accessible and can hybridize with complementary strands. Highly compact surface DNA density tends to sterically and electrostatically inhibit the initiation of duplex nucleation of the incoming complementary strand even when they are in proximity at the collision, resulting in a slower

hybridization rate.^[51] Therefore it is necessary to characterize the accessibility of the Probe sequence and Seq. 2 and their changes upon varying the surface coverage density with Diluent DNA. This knowledge would then help to understand the aggregation and disassembly of DNA-functionalized AuNP.

The total density of DNA sequences on AuNP and their accessibility were investigated. Briefly, AuNPs were functionalized with functional DNA and their density was varied by co-functionalizing Diluent DNA using the pH-assisted conjugation method. An excess amount of fluorescently labelled target DNA strand was then annealed to these DNA-functionalized AuNPs. The AuNPs were washed and then etched using KCN to determine the number of hybridized strands using fluorescence spectroscopy. Scheme 2-3 depicts the process. Refer to the methods (section 2.2.6) for details.



Scheme 2-3 A depiction of the method employed to determining accessibility of immobilized DNA on 30nm AuNP. Briefly, an excess amount of fluorescently tagged target strands were annealed to the DNA functionalized AuNPs. AuNPs were washed and then etched with KCN to compute hybridized target by using fluorescence microscopy.

Table 2-2 Summary of results obtained from the accessibility determination experiments showing the number and percentage of AuNP-functionalized strands (Probe and Seq. 2) that accessible for hybridization at various surface DNA densities.

% Seq. 2 density	Seq. 2 density (strands/AuNP)	Accessible density (strands/AuNP)	% Accessible Seq. 2	% Probe density	Probe density (strands/AuNP)	Accessible density (strands/AuNP)	% Accessible Probe
100	289	17	5.88	100	220	31	14.06
90	260	19	7.42	90	198	58	29.30
75	217	18	8.29	70	154	48	31.21
70	202	15	7.63	55	121	25	20.89
60	173	15	8.50				

Table 2-2 summarizes the findings and shows the number of surface-immobilized strands accessible for hybridization at various Probe and Seq. 2 surface DNA densities. Overall, a lower number of Seq. 2 strands (15 - 19 strands/AuNP) were accessible for hybridization as compared to the Probe sequence (25 - 58 strands/AuNP). For Seq. 2, the percentage of accessibility and the total number of accessible strands did not change significantly with decreasing surface DNA density. A higher density of Seq. 2 strands on the particle surface causes Seq.2 to be relatively less accessible due to high DNA crowding on the surface. Additionally, incorporation of Diluent DNA which are similar in length as Seq. 2 strands, increases the DNA crowding on the particle surface, thus further decrease their hybridization efficiency, thus accessibility. In contrast, AuNP functionalized with Probe and Diluent DNA shows a maximum number of accessible Probe strands for moderately diluted (70-90%) surface density. At maximum Probe surface coverage (220 strands/AuNP), the crowding of DNA lowers hybridization efficiency as all immobilized strands are of the same length. As more Diluent strands are incorporated on the AuNP surface, the longer Probe oligonucleotides become more accessible to the incoming target DNA because of lesser DNA crowding and easier DNA hybridization nucleation, resulting in a higher hybridization efficiency. Moreover, diluent DNA strands are known to hinder the formation of the secondary structure of neighbouring DNA strands on the AuNP surface. The Probe strands thus are even more accessible with enhanced hybridization efficiency upon the incorporation of diluent DNA.^[52] However, a decrease in accessibility of Probe sequence was observed at low coverage (121 strands/AuNP), which can be attributed to the loss of attainability upon diluting the surface density of the Probe strands. The data shows attainability can not solely be determined by the surface DNA density, but also by the accessibility of the strands. For the sequences we employed, attainability of Probe is higher than Seq. 2.

2.3.5 Exploring the Impact of the Surface DNA Density on the Aggregation of AuNPs

A systematic study was performed to establish the impact of surface DNA coverage on the kinetics of AuNP aggregation. UV-Vis absorption spectroscopy is a conventional method to investigate the stability and the aggregation behaviours of AuNPs in solution. Colloidal solution of 30-nm AuNP functionalized with DNA exhibits a sharp LSPR peak at 526 nm; however, when these free AuNPs form aggregates the LSPR peak red shifts, dampens and broadens, resulting in a decrease in peak intensity at 526 nm (Figure S-1 in Appendix-A section).^[8] This change in optical properties can be monitored to determine the extent of formation and disassembly of nanoaggregates. The extinction at the 526 nm reveals the extent of aggregation in the solution, therefore it can be monitored to determine the kinetics and thermodynamics of aggregation and disassembly processes. It also results in a visible colorimetric change in color of the solution from an intense red, when AuNPs are free, to purple/grayish, when AuNPs form aggregates.

Three batches of particles were prepared with varied Probe surface density and three additional batches of particles were prepared with varied Seq. 2 surface density. Figure 2-2 shows various surface DNA densities and their combinations explored in this study. Although Scheme 2-1a illustrates one hybridization event between two nanoparticles, it is crucial to recognize that there are many hybridization events possible at the interparticle junction, which is estimated to be ~10% of the overall surface area of 30 nm AuNPs. Incorporation of Diluent strands indirectly controls the average number of hybridized strands at the interparticle space, and modifies the avidity, cooperativity and attainability factors that influence the rate of formation and stability of the AuNP aggregates.

There are several environmental factors that tend to impact the hybridization kinetics and thermodynamics of AuNPs aggregation. Some of the major factors are ionic strength, pH,

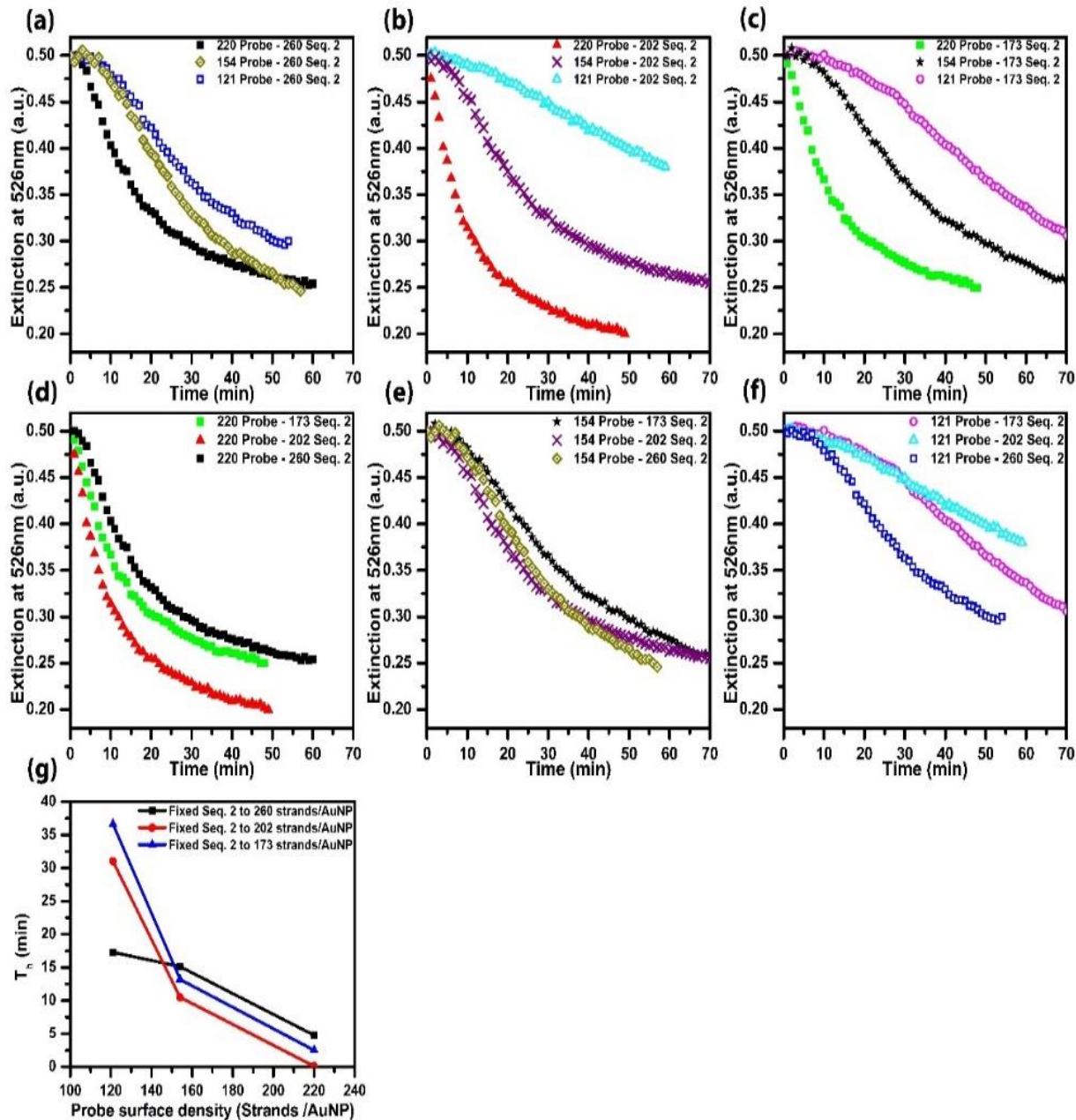


Figure 2-2 Impact of surface DNA density on the aggregation kinetics and binding properties. Herein, legends denote the number of strands/AuNP as the prefix, followed by the sequence name. Plots a, b and c show three sets of plots with surface Seq. 2 density fixed to 260, 202 and 173 strands/AuNP, respectively. In each of these plots, the Probe density is varied from 121 to 220 strands/AuNP and their aggregation kinetics and binding properties are determined by monitoring extinction at 526 nm over time. Similarly, data is reorganized in plots (d-f) to visualize the impact of Seq. 2 surface density on the aggregation process with fixed probe surface density. Plot (g) summarizes the impact of surface Probe density on the hybridization transition time (T_h , minimum of the first derivative to the aggregation curve) with Seq. 2 density kept constant.

temperature, the ratio of two sets of particles, and the concentration of functionalized AuNPs.^[51]

To minimize any contribution from these factors, all analysis in the aggregation study were performed at room temperature, in a neutral pH buffer containing 0.25M NaCl, and with a consistent ratio (i.e., 1:1) and concentrations of two sets of particles. The only factors contributing to the hybridization kinetics were the surface DNA density of functional DNA and the accessibility of the DNA strands. The kinetics of the formation of these nanoaggregates depends on the extent of collisions between AuNPs followed by the random encounter and hybridization of two complementary DNA strands. Since all the environmental factors were kept constant amongst all analysis, the aggregation kinetics and thermodynamics properties depended only on the DNA hybridization which is dictated by the random encounter of complementary DNA, attainability, and cooperativity by avidity. Figure 2-2 shows the kinetics of AuNP aggregation by monitoring the extinction at 526 nm over time upon mixing nine different combinations of the particles with different surface DNA density. Herein the number of strands/particle is denoted as the prefix, followed by the sequence name (i.e. Probe, or Seq. 2). The findings are organized into three sets: Figures 2-2a, b and c display the results when the density of Seq. 2 is fixed while the density of the Probe is varied (i.e. 121, 154 and 220 Probe strands per particle). Figures 2-2a-c reveal that the rate of hybridization dramatically depends on the surface density of Probe sequence. An increase in the Probe surface density while Seq. 2 was kept constant resulted in faster hybridization kinetics as depicted by the faster reduction in the extinction at 526 nm as the aggregates formed. The results obtained in these three plots agree with the expected results based on the attainability and avidity. As the Probe surface density is increased with constant Seq. 2 surface density, the attainability increases due to increase in the local density of probe strands which can retain and rebind the Seq. 2 strands more effectively after the transient unbinding event. Once a Seq. 2 strand is retained, other strands at the interparticle space can hybridize synergistically due to their precise orientation and proximity.

This cooperativity effect has been reported previously.^[51-53] Hence, fewer AuNP collisions and Probe–Seq. 2 encounters would be needed to form stable aggregates. Note that the impact of the change in surface density of the Probe sequence was more significant in particles with sparse Seq.2 density (Fig. 2-2b and c) as compared to AuNP densely populated with Seq. 2 (Fig. 2-2a). To understand these observations, we need to recognize that both strands, Seq. 2 and Probe, can contribute towards attinebility and avidity. With constant Seq. 2 surface density, decreasing the density of Probe eventually leads to a point where the number of accessible strands of both sequences becomes similar, and hence attinebility is minimal and a slower hybridization rate results. Overall, this observation is more pronounced when the density of Seq. 2 is low.

To quantitatively analyze these observations, the method proposed by Oh and Lee was employed to determine the hybridization transition time (T_h), at which half of the DNA-AuNP assembly formation is achieved. T_h is calculated from the minimum of the first derivative of the hybridization plot.^[51] Figure 2-2g shows how the T_h changes as the probe density is varied with fixed Seq. 2 density. In all three cases, hybridization transition time (T_h) is inversely proportional to the Probe density. As the surface density of two sets of particle becomes similar the rate of hybridization decreases as depicted by the dramatic increase in T_h . As expected from above explanation, for AuNP with highest surface DNA density, the increase in T_h from 154 probe density to 121 probe density is not increasing significantly due to attinebility contributed by densely populated of Seq. 2. It can be concluded from this study that to program the hybridization kinetics, one can control the attinebility by modulating the surface DNA density by introducing shorter Diluent DNA strands on the AuNP surface. The moderate surface density of Probe sequence works best for controlling the hybridization as at both extremes the attinebility appears to diminish significantly.

The data on the kinetics of AuNP aggregation are reorganized in Figure 2-2d, e and f. The plots reveal the impact of the change in the surface density of Seq. 2 while keeping the density of Probe constant. The T_h value does not change significantly as a function of Seq. 2 density except when the Probe density was extremely low and Seq.2 density was high (i.e. 121 Probe – 260 Seq. 2 combination). In this case, Seq. 2 has the potential to enhance the rate of hybridization via attainability, but this effect from Seq. 2 is not as significant as from Probe sequence. Therefore, to maximize the aggregation rate, one needs to employ AuNPs with high Probe density and moderate Seq. 2 surface density to maximize the attainability contribution.

2.3.6 Effect of Surface Density of Functional DNA on the Thermal Disassembly of Nanoaggregates

We have shown that co-functionalization of Diluent DNA strands can modulate the density of functional DNA strands, thereby influencing attractive forces and affinity through attainability, avidity and controlled valency of DNA-AuNPs. However, modulating the surface DNA density also has an impact on the repulsive forces due to a significant change in the steric hindrance and electrostatic force at the AuNP surface. The impact of surface density on the overall cooperative binding offered by these densely functionalized AuNPs can be revealed via additional thermodynamic investigations involving the thermal melting transitions of AuNP aggregates. The melting transition profiles are a strong indicator of binding properties of DNA on AuNP.

Temperature-induced disassembly studies of 30 nm gold nanoaggregates formed from the different combinations of two sets of DNA/AuNPs as in Section 3.6 were performed. Briefly, nano-aggregates were formed in a 0.25 M NaCl neutral pH phosphate buffer at room temperature for 1 h. These aggregates were then heated at the rate of 1°C/min until they disassembled as assessed by monitoring the increase in extinction at 526 nm using UV-Vis spectroscopy. DNA linked particles have much sharper melting transition curve as compared to that of free DNA due

to cooperative behaviour of DNA strands at the interparticle junction.^[53b] Cooperatively behaving DNA strands shift the melting-onset temperature to a higher value closer to the T_m which then disassemble quickly as T_m is approached to generate a sharp melting curve. A five-parameter logistic equation (5PL)^[54] was used to fit the melting curve:

$$Y = A1 + \frac{A2 - A1}{(1 + 10^{(x0 - x) * p})^s}$$

Equation 2-1 A five-parameter logistic equation

A1 = bottom asymptote
A2 = top asymptote,
x0 = center
P = hill slope
S = symmetry parameter

Thermal disassembly of free dsDNA strands in solution is a non-cooperative process where symmetrical sigmoidal fitting functions^[55] are used to analyze the melting process. However, due to the asymmetry, the 5PL equation (Equation 2-1) generated a better fit ($R^2 > 0.98$) for the melting transitions and elucidated the asymmetric nature of the melting curve; therefore, resulted in more accurate kinetic (FWHM) and thermodynamic (T_m , melting on-set and off-set) parameters from the first derivative of the melting curves.

Figure 2-3a and b show representative melting curves for nanoaggregates where the surface density for Seq. 2 was varied while the surface density of Probe was kept at 220 and 154 strands/NP, respectively. The first derivative plots of the fits are shown in Figure 2-3c and d, respectively. Likewise, Figure 2-3e and f are melting curves, and Figure 2-3g and h are first derivatives plots for nanoaggregates where Probe density is varied but Seq. 2 is fixed. It is clear that the surface density of DNA has an enormous impact on the melting transition profile, hence on the thermodynamic and kinetic properties of these nanoaggregates. We observe that the melting temperature (T_m), defined as the temperature at which half of the AuNPs have disassembled (i.e.

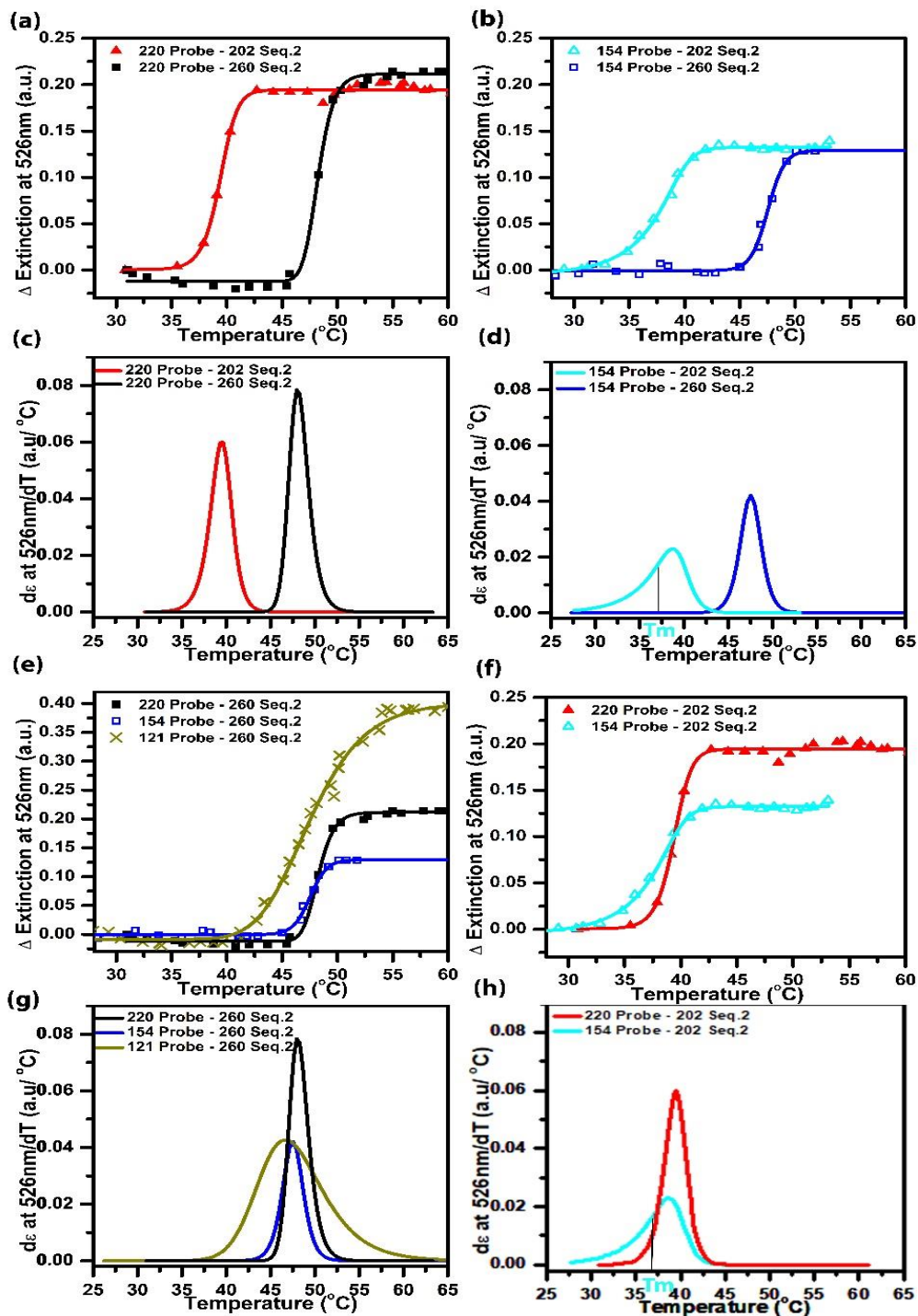


Figure 2-3 Impact of the surface density of DNA on the melting profile, hence on thermodynamic and kinetic properties of these nanoaggregates. Change in the extinction at 526nm is plotted against the temperature to generate melting curves. (a and b) representative melting curves for nanoaggregates where the surface density for Seq. 2 was varied while surface density of Probe was kept at 220 and 154 strands/NP, respectively. (c and d) show the first derivative plots of the fits shown in a and b, respectively. Likewise, e and f are melting curves, and g and h are first derivatives plots for nanoaggregates where Probe density is varied but Seq. 2 is fixed. T_m indicates the mid-point in the change of extinction of the sigmoidal transition curve

mid-point in the change of extinction of the sigmoidal transition curve), is directly related to the surface density of Seq. 2 but not to the Probe surface density; this trend can be seen by comparing Fig. 2-3a and b to Fig. 2-3e and f. Combinations of nanoparticles with high surface DNA densities (e.g. Fig. 2-3a) possess sharp melting transitions, as indicated by the narrow FWHM of the first derivate curves (Fig. 2-3c). This sharpness in the melting of DNA on AuNP is attributed to the cooperativity effect.^[53a, b] On the contrary, Fig. 2-3b and d show that there exhibits a significant loss in cooperativity for 154 Probe – 202 Seq. 2, as depicted by a significant increase in the FWHM of the first derivative curve. Notably, the first derivative is asymmetric for this set of AuNP as well as 121 Probe-260 Seq. 2. The absence of symmetry (where either left or right skew can be observed) suggests that there are different phenomena governing the rate of disassembly. Because of the asymmetry in the melting curves, the melting transition temperature and the temperature at which the disassembly is at its fastest rate are not the same (as

noted in Fig. 2-3d and h). The

asymmetry of the first derivative of the melting curves is characterized as shown in Figure 2-4: the front and the tailing portions are denoted by |AB| and |BC|, respectively. The symmetry factor is calculated according to the following formula:

$$S = \frac{C-A}{2(B-A)}$$

Equation 2-2 Symmetry factor (S) equation

A positive skew means length |AB| is shorter than the length |BC|, whereas negative skew

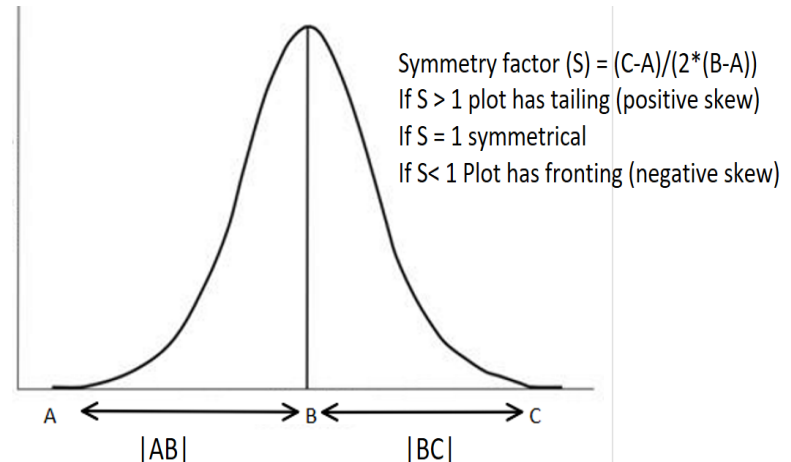


Figure 2-4 A diagram showing the method used to characterize the asymmetry of the first derivative cure.

is when length $|BC|$ is longer than $|AB|$; the corresponding symmetry factors are $S>1$ and $S<1$, respectively. Note that the symmetry factor only reveals the relative contribution of cooperativity and interparticle repulsion on the disassembly rate and not the rate of melting transition. When $S>1$, cooperativity dominates interparticle repulsion and vice versa. Refer to Table 2-3 for the parameters obtained from plots in Figure 2-3.

Table 2-3 Summary of parameter obtained from Figure 2-3. Impact of the surface density of DNA on the melting profile, hence on thermodynamic (T_m , melting on-set and offset) and kinetic properties (FWHM) of these nanoaggregates. Symmetry factor reveals the relative contribution of cooperativity and interparticle repulsion on the disassembly rate. Note, T_m and Inflection point are not identical values due to asymmetry.

Probe Density (Strands /AuNP)	Seq. 2 Density (Strands /AuNP)	Inflection Point ($^{\circ}\text{C}$)	Max. Melting Rate (A.U/ $^{\circ}\text{C}$)	T_m ($^{\circ}\text{C}$)	FWHM ($^{\circ}\text{C}$)	Melting on-set ($^{\circ}\text{C}$)	Melting off-set ($^{\circ}\text{C}$)	Symmetry Factor
220	260	47.96	0.08	48.2	2.7	44.1	54.6	1.27
154	260	47.54	0.04	47.5	2.7	41.2	54.0	0.98
121	260	46.58	0.04	47.5	8.5	35.2	64.0	1.34
220	202	39.52	0.06	39.4	2.8	32.2	44.4	0.90
154	202	38.68	0.02	37.2	4.9	27.5	45.8	0.71

We proposed that before the T_m , the front portion of the melting transition curve ($|AB|$) is controlled by cooperative binding attributed to the attinebility and avidity, while the tailing portion after the T_m ($|BC|$) is dictated by the total repulsive forces between the particles. At high attinebility, the Probe strands can retain as the duplex linker with Seq. 2 more effectively. This attinebility prevents the initiation of the disassembly process and hence shifts the melting on-set temperature higher; the net result is a very narrow front width of the melting curve. As attinebility and avidity decreases, the front portion of the first derivative increases; this trend is most prominent for 154 Probe – 202 Seq. 2 and 121 Probe – 260 Seq. 2 combinations (Table 2-3) where the surface density of Probe is low. Note that attinebility from Probe is more significant than Seq. 2 because

Seq. 2 is similar in length as the Diluent DNA and is therefore embedded in the DNA layer with lower accessibility. The density and accessibility of Seq. 2, however, control the number of linkers at the interparticle space and therefore T_m is related to the surface density of Seq. 2, and not Probe.

Once T_m is reached and more than 50% of the hybridized strands at the interparticle space dissociate, the effect of attainability diminishes, and the repulsive forces between AuNPs dominate and dictate the disassembly kinetics. The repulsion between the particles is related to the length and density of the negatively charged DNA strands functionalized on the AuNP. Table 2-4 summarizes the charge of each of the DNA-AuNP. The negative charge for Probe-AuNP varies by 13% (from 5940 to 5141) while that of Seq. 2-AuNP varies only by 5% (from 5356 to 5087). High electrostatic repulsion and steric hindrance results in the narrowing of the right half of the first derivative peak. The decrease in electrostatic repulsion is most significant for 121 Probe – 260 Seq. 2. where the positive-skewness in the first derivative curve and a high symmetry factor (1.34) are prominent. In summary, the surface density of DNA has a dramatic impact on the thermodynamic and kinetic properties of the temperature-induced disassembly of nanoaggregates.

Table 2-4 A tabulated summary of the impact of surface DNA density on the charge and crowdedness on the AuNP surface.

Set 1 Probe Density (Strands/AuNP)	Set 2 Seq. 2 Density (Strands/AuNP)	Set 1 Diluent Density (Strands/AuNP)	Set 2 Diluent Density (Strands/AuNP)	Charge (-ve)	
				Set 1	Set 2
220	260	0	35	5940	5356
154	260	104	35	5407	5356
121	260	156	35	5141	5356
220	202	0	104	5940	5087
154	202	104	104	5407	5087

2.3.7 Influence of Surface DNA Density on the Target-Induced Disassembly of Nanoaggregates

Next, we investigate target-induced disassembly of nanoaggregates which could be adapted as a biosensing platform. The impact of surface DNA density on the thermodynamic and kinetic properties of toe-hold mediated disassembly process is addressed. Unlike the thermal disassembly of the nanoaggregates, the target-induced disassembly must overcome additional barriers such as the added steric and electrostatic repulsion of the target strands and energy barriers associated with the toe-hold strand displacement reaction. Toe-hold binding is not a concern for less dense and accessible aggregates but accessing a compactly packed aggregate bearing many links at the interparticle space may be challenging for the target. Hence, binding of the target to the probe sequence can negatively influence the binding affinity of the subsequent target molecules in crowded interparticle junctions. Alternatively, the same target binding event can increase the interparticle repulsion and positively influence the binding affinity of subsequent target strands in less crowded junctions.^[56] Another difference is that once the target is bound to Probe sequence, the reverse reaction is energetically unfavourable due to the lack of toe-hold region for the reverse reaction. Therefore, the positively or negatively cooperative behaviour depends largely on the number of hybridization events present at the interparticle space.

To study the impact of surface density on the target-induced disassembly process, 30 nm particles with different surface Probe coverage prepared (220, 143 and 121 Probes/particle). Additionally, three more batches of 30 nm particles were prepared with varied Seq.2 surface densities (260, 202 and 173 strands/AuNP). Figure 2-5 shows the time-dependence of the change in LSPR extinction upon the addition of the target DNA-210. The experiments were performed at constant target concentration (206 nM), in which the target to Probe ratio was kept high to minimize the impact of target concentration on the disassembly process. The Target to Probe ratio

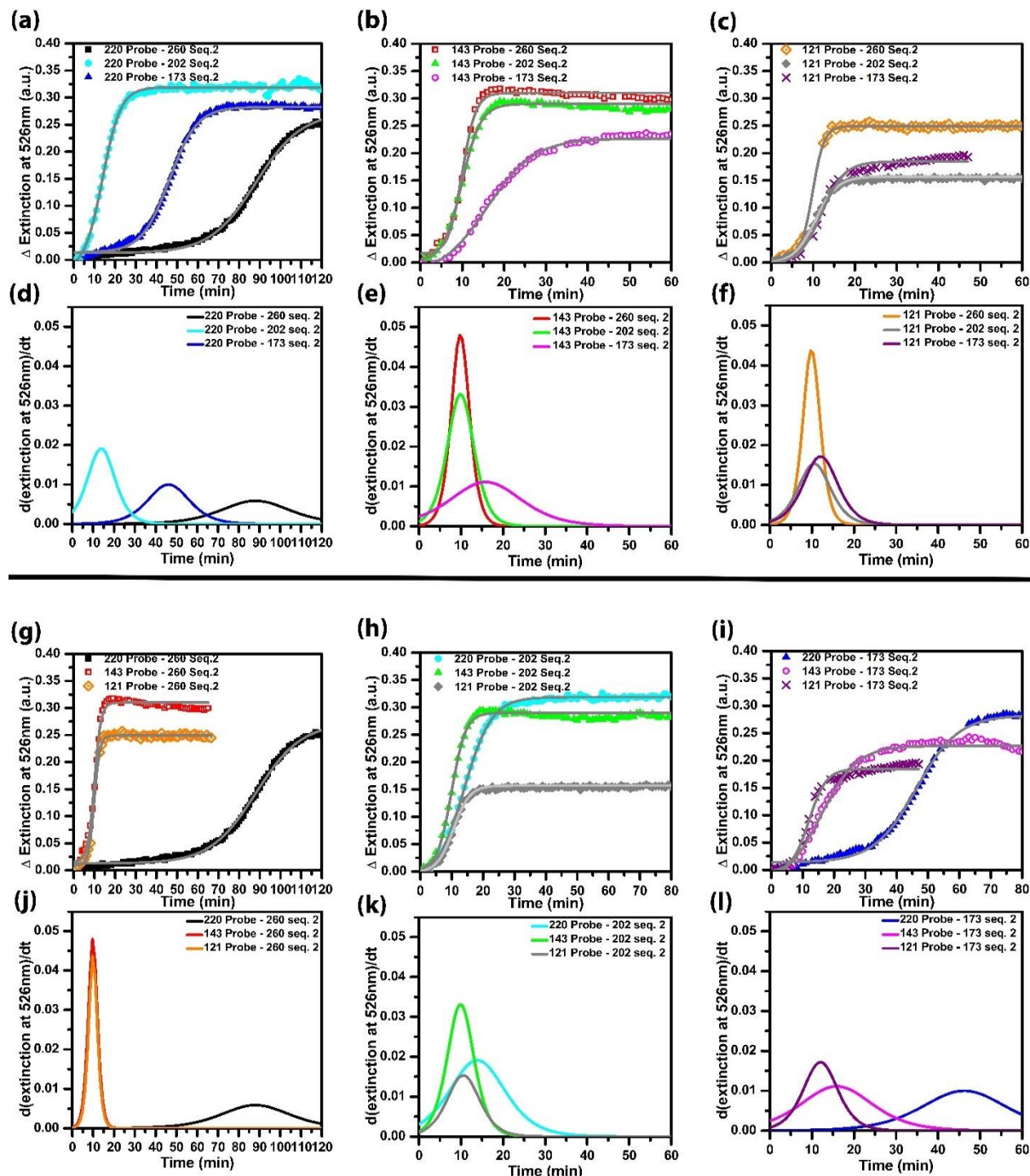


Figure 2-5 The impact of surface DNA density on the thermodynamic and kinetic properties of target-induced disassembly of nanoaggregates. The disassembly analyses were carried out with the target concentration of 206 nM in a neutral pH buffer (0.01 M PB, 0.3 M NaCl, and 0.01 % SDS). Change in the extinction at 526 nm over time is plotted to produce disassembly profile. a, b and c show sets of nanoparticles where the Probe surface density was fixed (220, 143, and 121, respectively) while varying Seq. 2 surface densities (260, 202 and 173 strands/AuNP). Plots in d, e and f show the first derivatives of the fitting curves from a, b, and c, respectively. Similarly, the same data was reorganized in figures (g-l) to elucidate the impact of varying the surface density of Probe with constant Seq. 2 density.

was 22, 14 and 12 for particles functionalized with 121, 143, 220 Probe surface density, respectively. Nine different combinations of these particles are investigated: Figures 2-5a, b and c show sets of nanoparticles where the Probe surface density was fixed to 220, 143, and 121 while varying Seq. 2 surface densities (260, 202 and 173 strands/AuNP). Figure 2-5d, e and f show the first derivatives of the fitting curves from Figure 2-5a, b, and c, respectively. Similarly, the same data was reorganized in Figures 2-5(g-l) to elucidate the impact of varying the surface density of Probe with constant Seq. 2 density.

In Figures 2-5a-f, a general trend that T_{50} (time required for 50% disassembly) and FWHM increase with decreasing Seq. 2 density was observed. An exception to this trend is found for 220 Probe -260 Seq. 2 combination. Because Seq. 2 has more limited accessibility than Probe, it is the limiting strand at the interparticle junctions and determines the number of links between particles. As Seq. 2 density decreases, more Probe strands at the junction are in excess and can, therefore, retain and rehybridize with any newly dissociated Seq. 2 strands via attainability. This effect leads to an increase in T_{50} . Concurrently, the binding of target strand to the probe increase crowding and steric and electrostatic repulsions, thereby negatively influence the binding of subsequent target strands; this effect leads to an increase in the FWHM. Additionally, the interparticle repulsion from target-Probe binding is higher for particles with high Seq. 2 density, hence the narrowest FWHM are observed for combinations with 260-Seq. 2. For 220 Probe – 260 Seq. 2, the trend was not observed because with many interparticle links in 220 Probe – 260 Seq. 2 and attainability, the kinetics of target disassembly shows high T_{50} and broad FWHM.

Now we consider the impact of increasing Probe surface density while keeping the Seq. 2 density constant (Figure 2-5(g-l)). We observe the general trend that increasing the density of Probe increases both FWHM and T_{50} value. This trend further supports the attainability effect

arising from extra Probe strands at the junction. Overall, to achieve fast and immediate target-induced disassembly, the combination of nanoparticles with high Seq. 2 surface density and low Probe surface density should be employed. The low Probe density decreases cooperativity and attainability to yield short disassembly time, whereas high Seq. 2 density sharpens the disassembly curve by increasing interparticle repulsion.

Table 2-5 summarizes the parameters obtained from plots in Figure 2-5. The T_{50} and FWHM values dramatically decrease as the probe density decreases with fixed Seq. 2 density, supporting the cooperativity by attainability. In contrast, when the Probe density is kept constant and Seq. 2 density is varied (combination # (2, 5 and 8), or (3, 6, and 9) in Table 2-5) the T_{50} and FWHM decreases and Seq. 2 density is increased, with an exception of combination # 1 as discussed above.

The repulsion between the particles is related to the length and density of the negatively charged DNA strands functionalized on the AuNP. The negative charge for Probe-AuNP varies by 13% (from 5940 to 5141) while that of Seq. 2-AuNP varies only by 8% (from 5356 to 4955). High electrostatic repulsion and steric hindrance results in the narrowing of FWHM. The impact of electrostatic repulsion can be elucidated when comparing the FWHM of combinations with fixed Probe surface density with varied Seq. 2 density (combination # (2, 5 and 8), or (3, 6, and 9)).

Table 2-5 Summary of parameter obtained from Figure 2-5. Impact of the surface density of DNA on the thermodynamic (T_{50}) and kinetic properties (FWHM) of target-induced disassembly of nanoaggregates, and on the charge and crowdedness on the AuNP surface.

Combination #	Set-1 (Probe /AuNP)	Set-2 (Seq. 2 /AuNP)	Set 1 (Diluent /AuNP)	Set 2 (Diluent /AuNP)	Charge (-ve)		T_{50} (min)	FWHM (min)
					Set 1	Set 2		
1	220	260	0	35	5940	5356	87.97	38.94
2	143	260	121	35	5313	5356	9.19	4.10
3	121	260	156	35	5141	5356	9.19	5.43
4	220	202	0	104	5940	5087	14.44	15.70
5	143	202	121	104	5313	5087	10.50	7.70
6	121	202	156	104	5141	5087	10.50	9.21
7	220	173	0	139	5940	4955	45.96	23.67
8	143	173	121	139	5313	4955	15.76	20.11
9	121	173	156	139	5141	4955	11.82	9.70

2.3.8 Using Fluorescently-Tagged Target to Determine the Impact of Surface DNA Density on the Toe-Hold Mediated Nanoaggregate Disassembly Process

To further understand the target-induced disassembly process, we employed fluorescently tagged DNA-210-cy3 as the target. The goal is to examine how readily the target can bind to the Probe strands in nanoaggregates of varying surface DNA density. Förster Resonance Energy Transfer (FRET)^[57] is a physical phenomenon that relies on the distance-dependent transfer of energy from a donor molecule to an acceptor molecule. The donor molecule absorbs the energy and subsequently transfers it to the acceptor chromophore via resonance. This leads to a reduction in the donor's fluorescence intensity and an increase in acceptor's emission intensity. Dye molecules and gold act as a donor-acceptor pair. The phenomenon of FRET is exploited to verify and determine the rate of hybridization of fluorescently tagged target molecules to the Probe sequence. The target was labelled with Cy3 dye covalently attached at the 3' end so that when the target hybridizes with the Probe, its fluorescence would be quenched due to its proximity to the AuNP

surface, and the overall fluorescence in the solution would decrease. To get a measurable change in fluorescence, the ratio of target to Probe is set as 2:1. Figure 2-6 shows the kinetics of decay in the Cy3 fluorescence for the different nanoparticle combinations and unaggregated Probe-AuNP at two different surface densities. For the unaggregated Probe-AuNP (220 Probe only and 121 Probe only), a single, rapid and immediate decay was observed because they have a large surface area with all their Probe strands exposed and available for hybridization. In nanoaggregates with sparse Probe density (121 or 132 Probes/AuNP, red, blue and green data), the quenching initiated immediately, and single decay kinetics was observed; the rate, however, is generally slower

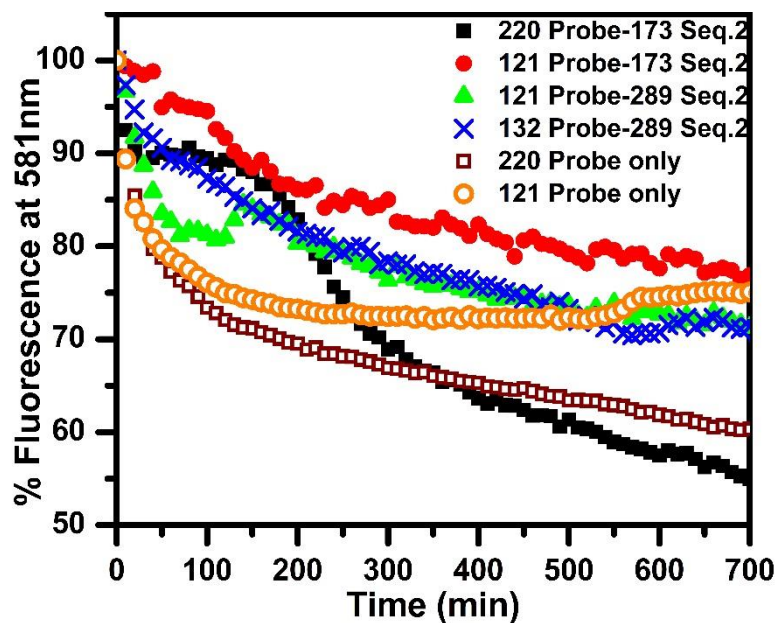


Figure 2-6 The impact of surface DNA density on the rate of hybridization of fluorescently tagged target. Quenching of fluorescently labelled target via FRET was monitored over time to determine the rate of hybridization of target to the Probe sequence. Unaggregated AuNPs (orange and brown) are also analyzed for comparison.

than free Probe-AuNP. On the contrary, for 220 Probe-173 Seq. 2, a small quenching is observed initially, followed by a long induction period (about 150 min) for additional quenching. In this combination, the Probe density is higher than Seq. 2 and there exists attainability and crowding at the nanoparticle junction. The initial small fluorescence quenching arises from the binding of the target to Probe strands outside of the nanoparticle junction; eventually, the target is able to disassemble the particles to yield more surface area and effective hybridization and therefore significant fluorescence quenching is observed at a second stage after >200 minutes. The data support the negative cooperativity arising from high DNA crowding at the junction.

Furthermore, to support the impact of Seq. 2 in the disassembly kinetics, we compare the results of 121 Probe-173 Seq. 2 (red) with 121 Probes-289 Seq. 2 (green). A clear difference in the rate of target binding was observed. As expected from the target-induced disassembly experiments, the aggregates formed with denser Seq. 2 (green) surface density were disassembling at a dramatically faster rate compared to the aggregates formed using lower Seq. 2 surface density (red). There was no delay in target binding, therefore, as supported by Seq. 2 accessibility experiments, Seq. 2 was not able to contribute towards attinebility. The increase in the rate of target hybridization can be explained by accounting for the electrostatic repulsion contributed by extra Seq. 2 strands at the interparticle space. As the target binds to the probe at the interparticle space, it enhances the repulsion between the particles. Therefore, the aggregates formed using AuNPs with higher Seq. 2 surface density while keeping the Probe density low, were disassembling at a much faster rate. These results can also be explained in terms of attinebility. When Seq. 2 density is lowered, there are relatively more free Probe strands at the junction contributing towards positive cooperativity via attinebility, hence slowing the rate of disassembly. Aggregates with 132 Probe – 289 Seq. 2 exhibits slower hybridization kinetics as compared to 121 Probe – 289 Seq. 2 because of the increase in attinebility as Probe density increase. These results support our proposal that the combination of high Seq. 2 surface density and low Probe surface density is desirable for sensing applications.

2.4 Conclusion

In this chapter, we explored the influence of DNA density on the aggregation, thermal disassembly and target-induced disassembly of DNA-AuNPs. The surface DNA density can be effectively modulated by exploiting pH-assisted functionalization approach followed by salt aging. Besides being a decent approach to modify surface density of DNA, the incorporation of diluent DNA offers additional advantages such as, enhanced particle stability, ability to inhibit secondary structure formation on the surface, a technique to control the accessibility of the functional DNA strands and to some extent can also control the size of the aggregates in the solution. Varying surface DNA density turned out to be an effective technique to tune the cooperative properties of densely functionalized DNA-AuNPs by directly controlling the number of DNA links at the interparticle junction, modulating the attainability and impacting the repulsive forces between particles. Etching DNA-functionalized AuNPs followed by staining with SYBR® (a fluorescent dye) is an effective technique to determine surface coverage of mono-component DNA layer on the AuNP. The surface DNA density was verified to be dependent on many factors such as the strand size, presence of secondary structure, and presence of polyA block on the strand. Along with the surface DNA density, the accessibility of strands is equally important in determining the number of link at the interparticle junction and the cooperative properties of functionalized DNA. Here, we verified that the use of nano-flares is an effective method to determine the accessibility of immobilized DNA strands. The relative length of the functional strand as compared to the diluent DNA strand largely impacts their accessibility. The Probe sequence being longer than diluent strand showed overall high accessibility which was further enhanced upon dilution of surface coverage with diluent DNA. In contrast, Seq. 2 showed highly limited accessibility which was not dependent on the dilution of the surface coverage with diluent DNA due to their high density and comparable size to diluent DNA strands.

The impact of surface DNA coverage on the hybridization kinetics of surface-bound DNA strands was established. An increase in the Probe density with Seq. 2 density kept constant results in a fast DNA hybridization kinetics due to enhanced cooperativity of functionalized DNA strands via attinebility and avidity. The contribution of Seq. 2 in cooperativity via attinebility and avidity is not significant due to their limited accessibility. Therefore, high Probe density and moderate Seq. 2 density is suggested to maximize the aggregation rate.

The thermal disassembly of the nanoaggregates was carried out to further understand the binding properties of AuNPs. The T_m is controlled by the limiting strand which was Seq. 2 due to its limited accessibility. Whereas, the melting transition of nanoaggregates is proposed to be controlled by cooperative binding before the T_m , and by the total repulsive forces between the particle after the T_m . Therefore, depending on their relative contribution, the first derivative of the melting curve can be skewed.

Finally, the impact of the surface density of DNA on the thermodynamic and kinetic properties of target-induced disassembly of nanoaggregates via toehold-mediated strand displacement reaction was investigated. The crowding at the interparticle junction dramatically impacts the time and rate of disassembly thus impacts the strand displacement reaction. The high Probe density delays and slows the disassembly by retaining newly dissociated Seq. 2 via attinebility and due to increased crowdedness at the interparticle junction which retards subsequent target bindings. The density of Seq. 2 was also observed to increase the disassembly rate via enhancement of repulsive forces between particles upon target binding to the probe sequence.

Henceforth, in chapter-3, these findings will be used for the rational design and optimization of a plasmonic biosensing platform that is based on the disassembly of nanoaggregates via toe-hold mediated strand displacement reaction.

Chapter 3. A Biosensing Platform: Detection of Oligonucleotide Biomarkers Based on the Disassembly of the Plasmonic Core-Satellite Nanocluster

3.1 Introduction

DNA nanotechnology has revolutionized the fields of nanoscience and nanotechnology. The information and properties of DNA molecules are used to manipulate the spatial and temporal distribution of matter. This structural nanotechnology has achieved construction of two-dimensional and three-dimensional functional structures of varying complexity and sizes using bottom-up DNA self-assembly. These assembled structures have emerging applications in the fields of biophysics, diagnostics, nanoparticle and protein assemblies, drug delivery and synthetic biology.^[58]

Although the specificity, sensitivity and limit of detection were improved by employing plasmonic coupling in solution aggregation, their susceptibility to environmental factors such as pH, temperature, ionic content and short shelf life limits their utility in many applications. Moreover, since aggregate formation and dissociation cannot be controlled in solution due to their ability to form different shapes, they have less potential for quantitative analysis. As mentioned above, the plasmonic properties and their coupling highly depend on the size, shape and density of the aggregate, the aggregation process should be controlled to develop a compelling sensing platform. Majority of these disadvantages can be resolved by constructing controlled aggregates on a solid substrate. In addition to overcoming inherent disadvantages associated with solution-based techniques, substrate-bound sensing platforms have the potential to further improve the detection performance such as a tunable dynamic range, improved sensitivity, high specificity and robustness. Additionally, surface-bound aggregates with highly controlled structure size can generate reproducible results with less batch-to-batch variation, and the overall cost can be minimized because of the lesser material required and high miniaturization potential. Since these

structures can also be incorporated with microfluidic setup, they can be made portable, reusable, and can be used in a variety of point-of-care environments. Furthermore, miniaturization in the form of nanoarrays would allow multiplexed detection with improved detection limits.^[10]

3.1.1 Surface-bound nanostructure: Discrete nanoparticle dimer structures

Discrete plasmonic dimer nanostructures have been studied to develop as chip-based sensors and plasmon ruler, and to monitor nanoscale distances between single pairs of gold and silver NPs.^[2a] The sensing platform is based on the distance-dependent plasmonic coupling between plasmonic NPs. This development was an important step towards realizing the use of biological scaffolds for greater selectivity and specificity. To fabricate these dimers, single plasmonic nanoparticle is first immobilized on the glass slide via highly specific biotin-streptavidin interaction. Single-stranded thiolated DNA with biotin functionalization is conjugated on AuNP via thiol-Au self-assembly, as shown in Figure 3-1a. Then, streptavidin coated AuNPs are introduced which, consequently, form a dimer by tethering two plasmonic particles by single-stranded DNA (ssDNA). The binding of an analyte specific to the tethered ssDNA changes the conformation of the DNA and increases the interparticle spacing, hence causing a spectral blue shift in LSPR frequency (Figure 3-1b) due to a decrease in plasmonic coupling.

A more specific dimer-based sensing study was executed by our group in the recent past to detect a biomarker, miR-210.^[1c] Figure 3-1c shows a heterodimer comprised of 100 nm and 60 nm AuNPs that was linked by a stem-loop DNA motif. Hybridization of miR-210 formed a rigid double-stranded DNA (dsDNA) structure and resulted in geometrically extended DNA loop. The weakening of distance-depended plasmon coupling resulted in a significant blueshift of the LSPR frequency. The dimer platform was demonstrated to tremendously improve sensitivity and limit of detection as it was able to detect femtomolar concentration of target in optimally buffered

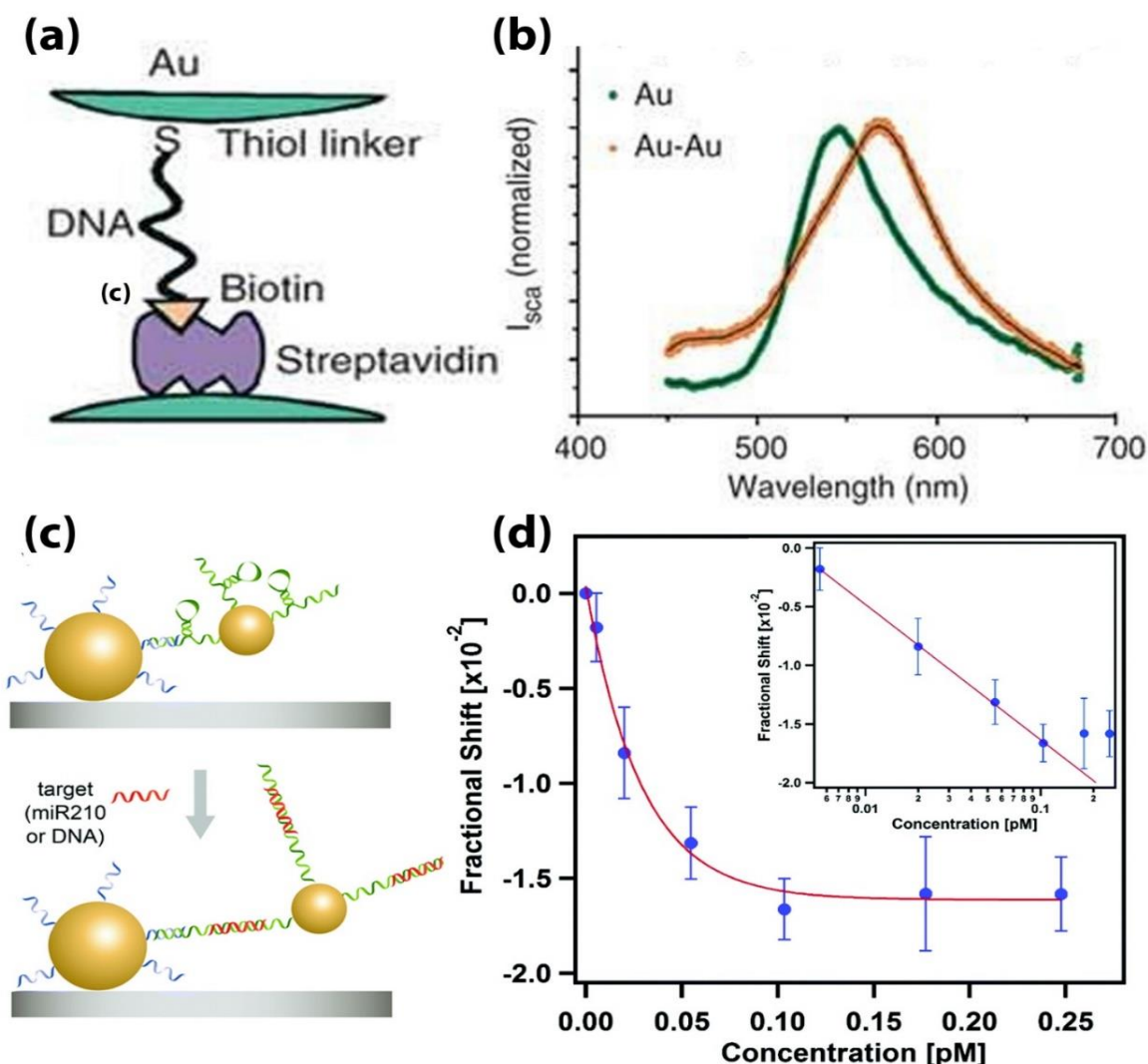


Figure 3-1 Illustration of discrete NP dimer structures as a plasmon ruler and as a sensing platform. (a) Design of the interparticle ssDNA tethering in a plasmon ruler by means of thiol-Au bonding on one end and a highly specific Streptavidin-Biotin binding on the other end. (b) Representative scattering spectra of AuNP (green) and AuNP pair (orange) revealing a spectral shift of 23nm due to plasmon coupling. Adapted from reference 2a with permission. (c) a schematic of a stem-loop DNA-linked NP dimer as a sensing motif (top) and a geometrical extension of dimer upon hybridization of target strand (bottom). (d) Results generated via scheme (c) revealing the sensitivity and dynamic range of the dimer motif. An exponential relation is observed between the fractional shift and the target (miR-210) concentration. Inset shows calibration curve on a logarithmic scale. Adapted from reference 1c with permission.

conditions (Figure 3-1d). Additional advantages offered by this platform were high specificity, rapid detection, potential to be miniaturized and suitability for multiplexed detection.^[1c]

Additionally, dimer structures have been exploited for the elucidation of the kinetics of

hybridization by recording the time dependence of spectral shifts.^[2a] However, the dimer platform has inherent limitation such as a narrow dynamic range, significant background noise in complex media due to non-specific binding on the surface, and false positive readouts from environmental factors discussed above. Detection based on disassembly of surface-bound nanoclusters has the potential to further improve and resolve these challenges.

3.1.2 Surface-bound core-satellite nanoassemblies

One of the strategies for improving the sensitivity of a plasmonic biosensor is to construct three-dimensional (3D) assemblies such as a layer-by-layer assembly technique to fabricate multiplayer AuNP structures.^[2b, c] Disassembly of these nanoassemblies upon introducing target yields enhanced changes in scattering intensity and a spectral shift. Fabrication schemes for core-satellite nanoassemblies on a substrate have been recently explored by various research groups to monitor enzymatic activities and to follow cell-signaling pathways *in vivo*.

Our group has recently reported a biosensing platform^[59] for the specific detection of Adenosine Triphosphate (ATP) molecules based on the disassembly of the surface-anchored plasmonic core-satellite nanostructures. The highly regulated and organized plasmonic assembly was comprised of a core AuNP surrounded by layers of satellite AuNPs through aptamer linkers. Figure 3-2a shows representative Scanning electron microscopy (SEM) images of assemblies with 1, 2, and 3 layers of satellite particles (30 nm core) around a 60 nm AuNP core. The use of oligonucleotides as the linker for the reversible assembly of these assemblies is of utmost importance for DNA technologists. The opportunity to enhance scattering intensity, signal-to-noise and sensitivity via plasmonic coupling by controlling the size of the assembly was exploited to design this chip-based design. The specific interaction of the ATP molecules with the aptamer linker induces disassembly and leads to a dramatic decrease in the scattering intensity that can be

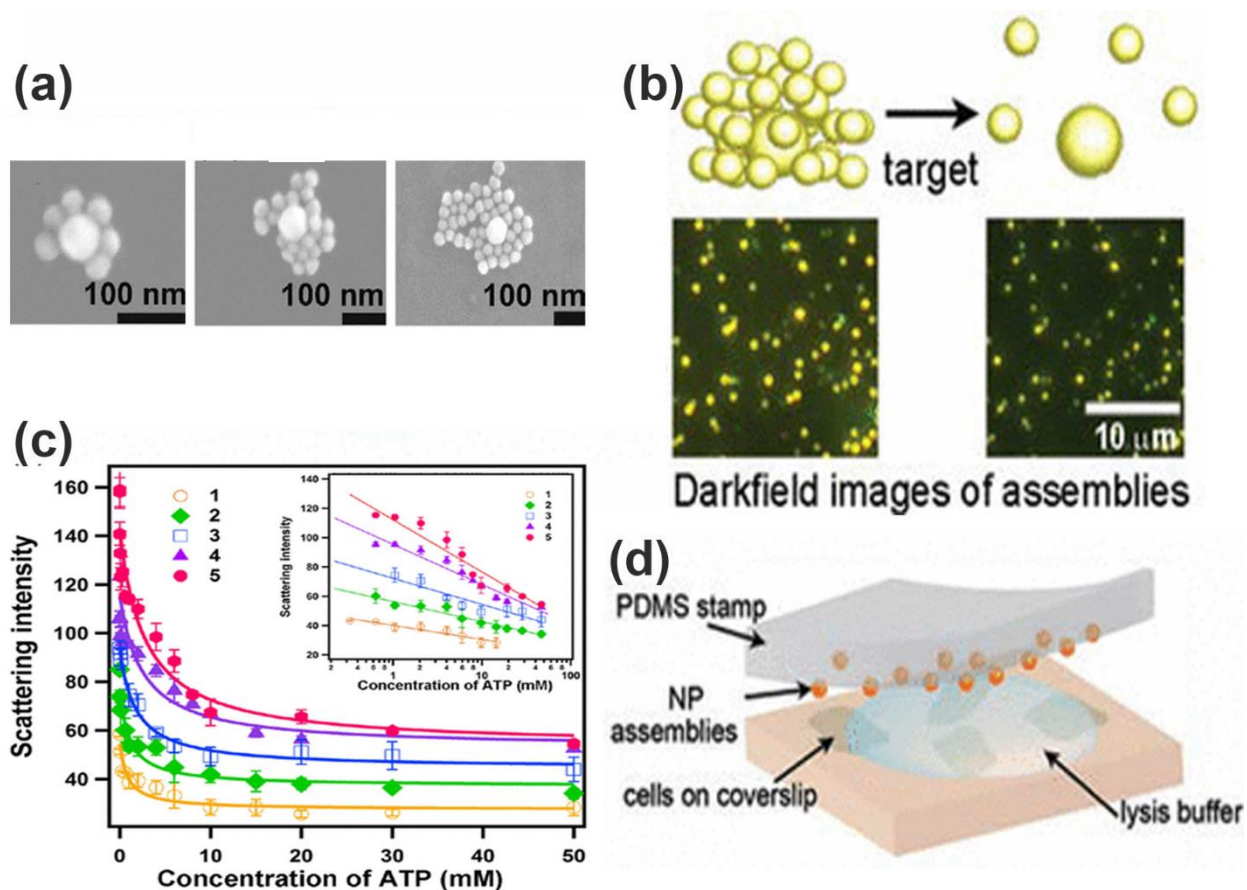


Figure 3-2 A plasmonic biosensor based on the disassembly of surface-anchored core-satellite nanocluster. (a) Representative SEM images of assemblies with 1, 2 and 3 layers of satellite (30 nm) AuNPs on a 60 nm core AuNP. (b) The sensing via disassembly of the nanoaggregate into individual satellite particles in the presence of the target is illustrated here along with the concomitant decrease in scattering intensity shown in DF images. (c) Calibration curve and tunability of the sensing platform is depicted in the plot where different sized cluster expressed different dynamic performance. Inset in (c) shows the linear relationship between the scattering intensity and the log of target concentration (d) The setup for the direct detection of ATP from lysed adherent cells which were in close contact with the plasmonic assemblies. Adapted from reference 59 with permission.

monitored by darkfield images, as can be observed in DF images in Figure 3-2b. More importantly, the potential to tune the sensing performance, such as detection limit, dynamic range and sensitivity, simply by controlling the size of the assembly was demonstrated. Calibration Plot in Figure 3-2c, demonstrate the disassembly profile of different sized assemblies, unrevealing the tunability of the sensing platform. The inset in Figure 3-2c shows a linear relationship between the scattering intensity and the log of the target concentration. Additionally, the sensor demonstrated

robustness and practicality by direct detection of ATP from lysed adherent cells which were in close contact with the plasmonic assemblies, as illustrated in Figure 3-2d. Along with the ability to detect in complex medium without any preparatory or purification steps, this chip-based sensing platform can be incorporated into low-cost portable imaging systems.

3.1.3 Purpose

The sensing platform discussed above in section 3.1.2 has the potential to be adapted for a variety of target, hence multiplexed detection with high sensing performance is possible. Thus, one of the objectives of this study is to adapt the biosensing platform based on the disassembly of plasmonic core-satellite nanocluster for the specific detection of oligonucleotides. Detecting macromolecules, instead of small molecules such as ATP molecules, would indicate the span of molecules the sensor can potentially detect. The specificity of the sensor is based on the interaction of the analyte with the linker molecule; therefore, each type of analyte requires a different type of linker molecules. For example, nuclease activity can be determined by a designing a linker that can be cleaved specifically by the nuclease^[2b]; ATP was detected by our group by exploiting the structural-switching property of the aptamer upon interaction with the ATP which caused the linkage to weaken, thus disassemble. Herein, we aim to detect miR-210 by designing a linker molecule bearing a toehold domain complementary to the target sequence which can offer specificity during the target hybridization and can further enhance it during the strand migration step.

Herein, we aim to adapt our ATP sensing platform for the detection of miR-210. Compared to small-molecules, the larger size and charge on the oligonucleotides can strongly impact the sensing performance of the platform because of the inaccessibility due to steric and electrostatic repulsion at the particle surface and due to the energy barriers during target recognition and strand

migration steps. Therefore, the fundamental study in chapter-2 was carried out to understand how some important factors, such as above-mentioned energy barriers, cooperativity, and attainability contribute towards the assembly and disassembly process. The observation and results were utilized here to optimize the design of a label-free, low cost and miniaturized biosensing platform. Compared to benchmark techniques, the sensing platform described in this study has the potential to offer competitive, if not better, dynamic performance, such as high sensitivity, high S/N ratio, wide dynamic range, low detection limit, high selectivity and specificity without the need of laborious manipulations and labelling of the target. Since these structures can also be incorporated with microfluidic setup, they can be made portable, reusable, and can be used in a variety of point-of-care environments. Furthermore, miniaturization in the form of nanoarrays would allow multiplexed detection with improved detection limits. We successfully manipulate the system for the rapid and selective detection of an exemplary nucleic acid biomarker – microRNA-210, enabling diverse biological applicability.

3.2 Experimental

Refer to chapter-2 for reagents and materials information (section 2.2.1) and for the protocol used to prepare DNA-functionalized BSPP-capped AuNPs (section 2.2.2 - 2.2.4). Refer to sections 2.2.5-2.2.6 for procedure to determining DNA Loading on Satellite NPs and to determine DNA accessibility on the AuNP surface, respectively.

Additional DNA sequences used: Control-DNA strands for assembly

Control-1: 5'- /5ThioMC6-D/AAA AAT CAA CCT TGG TTA TAC GAT GAC-3'

Control-1-complement: 5'- /5ThioMC6-D/AAA AAA AAA AGC TAT AAC C

3.2.1 Activation and Preparation of Silanized Glass Substrate

Glass coverslips were first rinsed with water and 2-propanol followed by 20 min of plasma treatment (Harrick's PDC-32G). Cleaned cover-slips were then immersed in a freshly prepared 0.5% APTMS solution in anhydrous ethanol for 2 hours. Silanized coverslips were then rinsed with 2-propanol and heated on hot plate for 1 hour under nitrogen at 85°C followed by an overnight heating at 85°C without nitrogen.

3.2.2 Deposition and DNA-functionalization of Core AuNPs on amino-modified substrate

Citrate-capped AuNPs (60 nm or 100 nm) were first immobilized on a silanized glass substrate by depositing 5 μ L of diluted (1:5) stock of colloidal core AuNPs for 5 minutes to allow AuNPs to be electrostatically attach to the amino groups on the modified surface. Excess solution was then rinsed with water and dried with compressed air. Coverage of core particles on the substrate was then checked under the dark-field microscope (Nikon Eclipse, TE2000-U), and the area was marked with a glass scribe for visualization during downstream steps. These core particles were then functionalized with DNA of interest by putting 10 μ L of 0.01 M PB, 1.25 M NaCl, 0.1% SDS and 10 μ L of DNA (2-5 μ M) over the scribed area for 2 hours. Sample was kept in a humid

container during 2 hours of incubation to prevent evaporation. Then the sample surface was rinsed with water and dried with compressed air.

3.2.3 Passivation of the substrate surface after core functionalization

To prevent specific and non-specific binding of the satellite nanoparticles on the amino-modified glass coverslip, the remaining amino groups on the coverslip are protected. The area of interest ($\approx 20 \text{ mm}^2$) was stamped with perfusion chamber and was incubated with approximately 10 mM mPEG-SVA solution in 0.1 M bicarbonate buffer (pH of 8.3) for 4 hours. Then the coverslip was treated with 0.2 M solution of sulfo-NHS-acetate in 0.1 M bicarbonate buffer (pH 8.3) for 4 hours again to protect remaining amino groups that are not protected by bulky mPEG-SVA treatment. After passivation, the sample was rinsed with water and dried with compressed air. A fresh perfusion chamber was stamped to incubate the surface in 0.01 M PB, 0.4 M NaCl buffer in a humid container until further use.

3.2.4 Layer-by-layer assembly on the core AuNPs

The first layer of satellite particles on the DNA-functionalized core was constructed by replacing the storage buffer with a concentrated (0.6 nM) solution of satellite particles (bearing DNA strands complementary to the DNA functionalized on the core particle) in 0.01 M PB, 0.4 M NaCl and 0.01% SDS and allowing to incubate for 45-60 min. The solution was then quantitatively replaced with the storage buffer (0.01 M PB, 0.4 M NaCl). To assemble the second layer, satellite particles (0.6 nM in 0.01 M PB, 0.4 M NaCl and 0.01% SDS) bearing complementary DNA to the first layer were incubated for 45-60 min. The procedure was repeated until desired number of layers were assembled. Each layer assembly was monitored by dark-field microscopy. Nanoassemblies were stored in 0.01 M PB, 0.13 M NaCl until sensing experiments.

3.2.5 Detection of the biomarker (DNA-210 or miR-210) by core-satellite disassembly

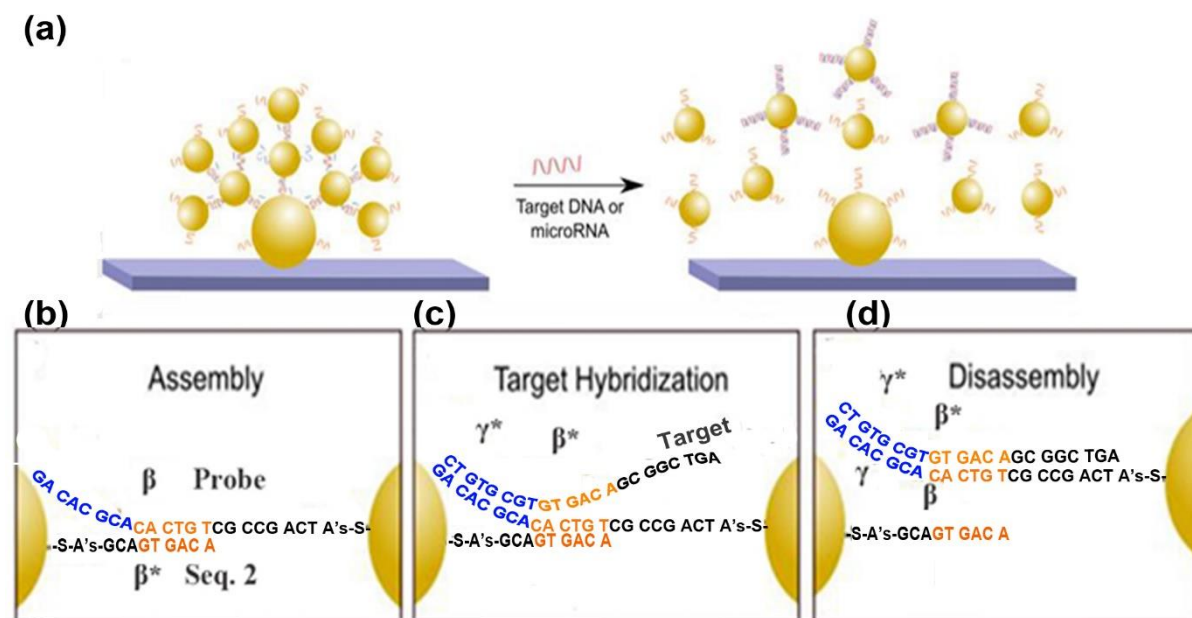
Dark-field images are captured before initiating the sensing experiments. Depending on the type of analysis (kinetic analysis or calibration curve construction), the appropriate amount of target was added in the hybridization chamber and allowed to incubate for appropriate duration of time before capturing dark-field images.

3.2.6 Cell-lysate preparation (hypoxic and normoxic cells)

Human trophoblast cells (HTR-8/SVneo) were cultured in 100-mm petri dishes in incubators (set to 37°C) until desired confluency was achieved. Confluency was monitored by compound microscope until harvesting step. Cells were washed three times with 2 mL of 1x PBS. Volumes of 2 mL of trypsin and 2 mL 1xPBS were added to the petrie dish and placed the dish in incubator for 2 min (or until detached). Cells were collected in microcentrifuge tubes. Cells were purified by centrifuging (1400 rpm for 4 min). Supernatant was discarded and cells were collected in one tube. Cells were resuspended and incubated in lysate buffer (0.10 M PB, 0.05% Triton X-100, 0.11 M NaCl) for 2 hours at room temperature. Cell debris was removed by centrifuging (10K rpm, 10 min) twice with 0.10 M PB, 0.11 M NaCl (300 µL each). The lysate was immediately used for disassembly analysis. To determine the upregulation of miR-210 in hypoxic cells, CoCl₂ (100 µM) was added to the cells for 24 hours before harvesting.

3.3 Results and Discussion

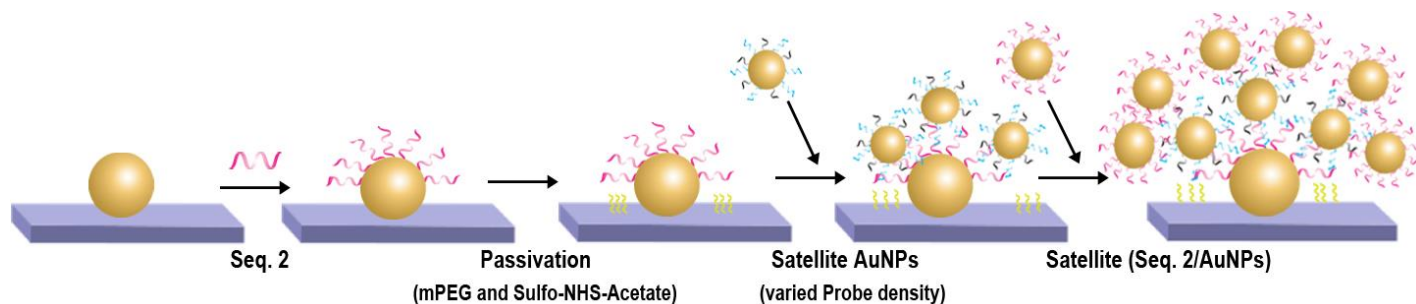
The sensing platform consists of core-satellite nanoclusters on a modified glass substrate using the bottom-up DNA self-assembly approach. Scheme 3-1 depicts the sensing mechanism along with the toe-hold mediated strand-displacement motif as established in Chapter 2. The layer-by-layer assembly of satellite AuNPs around a large core nanoparticle yields controlled size of the assembly and the optical properties. The scattering cross-section of the nanoclusters increases due to plasmonic coupling, and the disassembly induced by target (DNA-210 or miR-210) therefore yields a dramatic decrease in the scattering signal in darkfield microscopy. We explore this optical detection signal for the detection of miR-210, a biomarker for hypertensive-related diseases. The



Scheme 3-1 The mechanism of the sensing platform based on the disassembly of core-satellite nanoassemblies via toe-hold mediated strand-displacement reaction is depicted here. (a) The layer-by-layer assembly of satellite AuNPs around a large core nanoparticle disassembles when target is introduced to it. (b) A representation of the interparticle linkage that occur via hybridization of the β domain of the Probe sequence with the β* domain of the Seq. 2. (c) the γ* domain (blue) of the target (DNA-210) hybridizes with γ toe-hold domain (blue) of the Probe sequence to initiate the toe-hold strand displacement event, and finally (d) the strand migration of the target strand displaces DNA Seq. 2 resulting in disassembly of the AuNPs.

platform can offer enhanced signal-to-noise ratio which is highly desirable for an ultrasensitive detection platform.

3.3.1 Fabrication of a Core-Satellite Nanocluster on a Glass Substrate



Scheme 3-2 The layer-by-layer DNA self assembly approach to fabricate a core-satellite nanoassembly on a substrate. The core (60 nm or 100 nm AuNP) is first deposited on a silanized glass substrate which are then functionalized with thiolated Seq. 2 strands. Then the substrate is passivated with mPeg-SVA and Sulfo-NHS-Acetate for downstream manipulations. A large excess of Probe-functionalized satellite particles (30 nm AuNP with desired surface density) are then allowed to self assemble on the core via DNA hybridization. Then Seq.2-functionalized satellite particles are introduced in large excess to self-assemble into second layer by hybridizing with the Probe sequence. This cycle can be repeated to achieve desired number of layers.

The fabrication of core-satellite nanoclusters on a chemically modified glass substrate is depicted in Scheme 3-2. Surface Cleaning is one of the most crucial steps in the construction of evenly sized and uniformly spaced nanocluster. Therefore, the glass coverslip is first plasma cleaned to remove impurities and to free hydroxyl groups for further surface modifications. The activated glass coverslip is then silanized with (3-Aminopropyl)trimethoxysilane (APTMS) to form a self-assembled monolayer (SAM) of silanes on the glass surface with exposed amino groups ($-NH_2$).^[60] Negatively charged core particles are then electrostatically deposited on the amino-modified substrate in a two-dimensional array. Deposited core particles are then covalently functionalized with the thiolated Seq. 2 strands via thiol-gold chemistry. To minimize non-specific adsorption to the substrate, the satellite particles were capped with Bis(p-sulfonatophenyl)phenyl phosphine dihydrate dipotassium salt (BSPP) prior to conjugating with DNA strands. Citrate

capping was replaced with BSPP via ligand-exchange reaction by overnight mixing with a large excess of BSPP. BSPP is a relatively stronger ligand and presents a larger negative charge on the AuNP surface, hence BSPP-capping is known to enhance the colloidal stability and the hydrophobicity of the AuNP surface.^[61] The colloidal stability imparted by BSPP was verified by increasing the salt concentration of citrate-capped and BSPP-capped 30 nm AuNP colloidal solutions separately. It was observed that AuNPs functionalized with BSPP were stable at 0.10 M NaCl while citrate-capped particles were stable only up to 0.025 M NaCl concentrations.

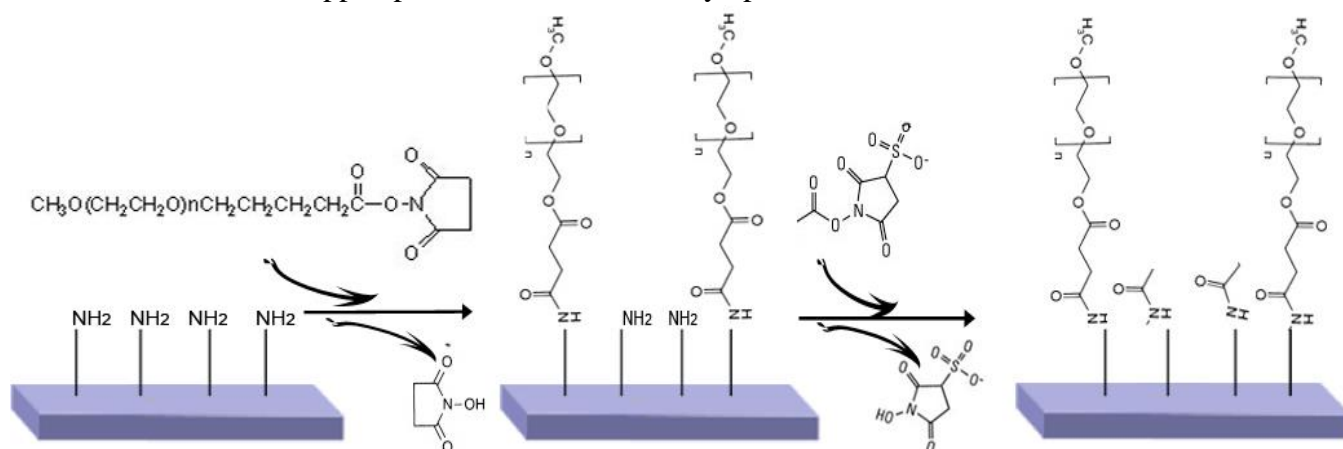


Figure 3-3 A reaction mechanism for the PEGylation of the amino-modified surface followed by acylation of sterically shielded amino groups to achieve an effective surface passivation. Primary amines on the substrate react with bulky mPEG ester molecules by nucleophilic attack at slightly basic pH which immobilizes mPEG on the substrate and releases N-Hydroxysuccinimide (NHS) as by-product. Passivation can further be improved by acylation of sterically shielded amino groups via similar mechanism using Sulfo-NHS-acetate which generates Sulfo-NHS as by-product.

To minimize specific and non-specific adsorption of satellite particles in the subsequent steps, the extra amino groups on the glass substrate are then PEGylated with bulky mPEG-SVA ester which immobilizes the mPEG on the substrate by forming an amide bond with the primary amino group and releases 1-hydroxy-2,5-pyrrolidinedione as a by-product. Since primary amines react with mPEG-SVA by a nucleophilic attack, the reaction mechanism requires neutral to a slightly basic environment for effective passivation. Therefore, the passivation process where the APTMS treated hydrophilic surface gets converted to a hydrophobic surface is carried out in 100

mM sodium bicarbonate buffer at the pH of 8.3, as illustrated in Figure 3-3. The passivation of the silanized surface with mPEG-SVA was effective when working with AuNPs functionalized with 100% Probe or 100% Seq. 2. However, when the surface DNA density was lowered by employing diluent DNA, the non-specific binding of satellite AuNPs to the passivated surface was dramatically increased, rendering passivation practically ineffective. The insufficient shielding of the AuNPs by shorter diluent DNA was hypothesized to be the contributing factor towards non-specific adsorption of AuNPs on the passivated substrate. Moreover, bulky mPEG molecules immobilized on the amino group during passivation are ineffective at protecting all amino groups on the densely packed SAM of APTMS. Hence, additional surface protection with relatively smaller Sulfo-NHS-Acetate is performed to effectively block exposed amino groups. The Acylation step using Sulfo-NHS-Acetate after mPEG-SVA treatment was observed to be effective. As in the PEGylation step, Sulfo-NHS-acetate reacts with and irreversibly blocks primary amine by forming stable, covalent amide bond in a slightly basic environment.^[60, 62] Once amine is irreversibly capped with an acyl group, the electrostatic interactions between satellite AuNPs and the substrate surface diminishes, hence specific and non-specific adsorption is efficiently minimized. Therefore, it was established that both passivation steps are essential for the core-satellite fabrication.

An excess amount of 30 nm satellite Probe-AuNPs was incubated with the core Seq.2-AuNP to form the first layer of particles through programmed DNA hybridization at high NaCl concentration (0.40 M) in the hybridization chamber. After incubation of about 45 min, the excess satellite particles were washed off with the buffer containing 0.40 M NaCl. Similarly, additional layers can be fabricated on top of the previous layer by introducing satellite particles bearing complementary DNA strands, i.e. alternating between Probe and Seq. 2 functionalized satellite AuNP, resulting in a large core-satellite nanocluster via DNA hybridization of the immobilized

DNA strands. As more layers of satellite AuNPs are assembled around the core AuNP, the size of the core-satellite nanocluster increases, and which can be monitored by DF microscopy.^[2c] Additionally, as these AuNPs are spatially brought closer through DNA hybridization, the strong plasmonic coupling interactions result in a substantial red-shift and broadening of the plasmon peak which can also be monitored by DF microscopy.

Care and precautions are required when handling these nanoclusters because they are very prone to disassembly when dried or when shear forces are introduced during solutions exchange steps in the hybridization chamber. Additionally, as observed by other researchers, capillary forces impact the structure of these nanoclusters when the sample is dried.^[63] Therefore, throughout the assembly and disassembly process, nanoclusters are kept in an appropriate solution and were not allowed to dry.

3.3.2 Method for the Optical Analysis Assembly and Disassembly Process

A typical layout of an inverted DF microscope is illustrated in Figure 3-4, where a light source (Halogen lamp) transmits white light through the dark-field condenser. A specialized disc (the patch stop) in the condenser blocks the majority of the incident light, leaving only an outer ring of the incident light. Some of the incident light gets scattered by nanoclusters due to LSPR and is collected by the objective lens, which has a smaller numerical aperture than the condenser. The scattered light is either routed to the eye-piece, Charge-Coupled Device (CCD) camera to produce an image or to a spectrometer to acquire scattering spectra from each individual nanocluster.^[4]

Both layer-by-layer assembly and the extent of target-induced disassembly of the core-satellite nanoaggregate were monitored by darkfield imaging. For the quantitative analysis of the assembly and disassembly of these nanoaggregates, the scattering intensity of the captured

grayscale JPEG images was employed as the optical signal. The average intensity of pixels corresponding to the nanocluster in the DF-images is used for intensity analyses. Our group has previously validated the analysis of DF image analysis by comparing results obtained from images with those obtained through single-nanoparticle scattering spectroscopy.^[59] The quantitative analysis via images also offers us the ability to simultaneously analyze optical properties of hundreds or even thousands of nanoaggregates that

are present in the field of view, making it a highly efficient and a facile method. The scattering intensities of the DF images were processed using Igor Pro software.

3.3.3 Monitoring the Assembly of Core-Satellite Nanocluster Anchored on the Substrate

We investigate the assembly process of DNA-AuNP with different surface densities of Probe and Seq. 2. Figure 3-5 shows the darkfield images of the samples during the layer-by-layer assembly. Here we qualitatively monitor the assembly process by colorimetric comparison of the nanoaggregates as we build layers on the core. Figure 3-5(a- d) and Figure 3-5(e-i) show layer-by-layer DF-images of two separate nanoaggregate formations using 60 nm and 100 nm AuNP as the core, respectively. Comparing the 100 nm with the 60 nm core, the color of the 100 nm core is

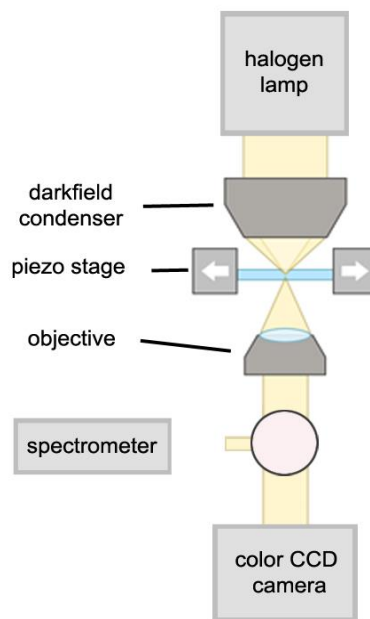


Figure 3-4 A diagram describing the layout of a typical inverted DF microscope. The white light is focused on the substrate where some of the incident gets scattered by the nanoassemblies and is collected by the objective lens. The output signal is directed to the eye-piece, charge-couple device (CCD) camera for imaging and to the spectrometer for measurement of spectrum.

relatively more intense and yellowish-green whereas 60 nm core is dimly green in color. The light

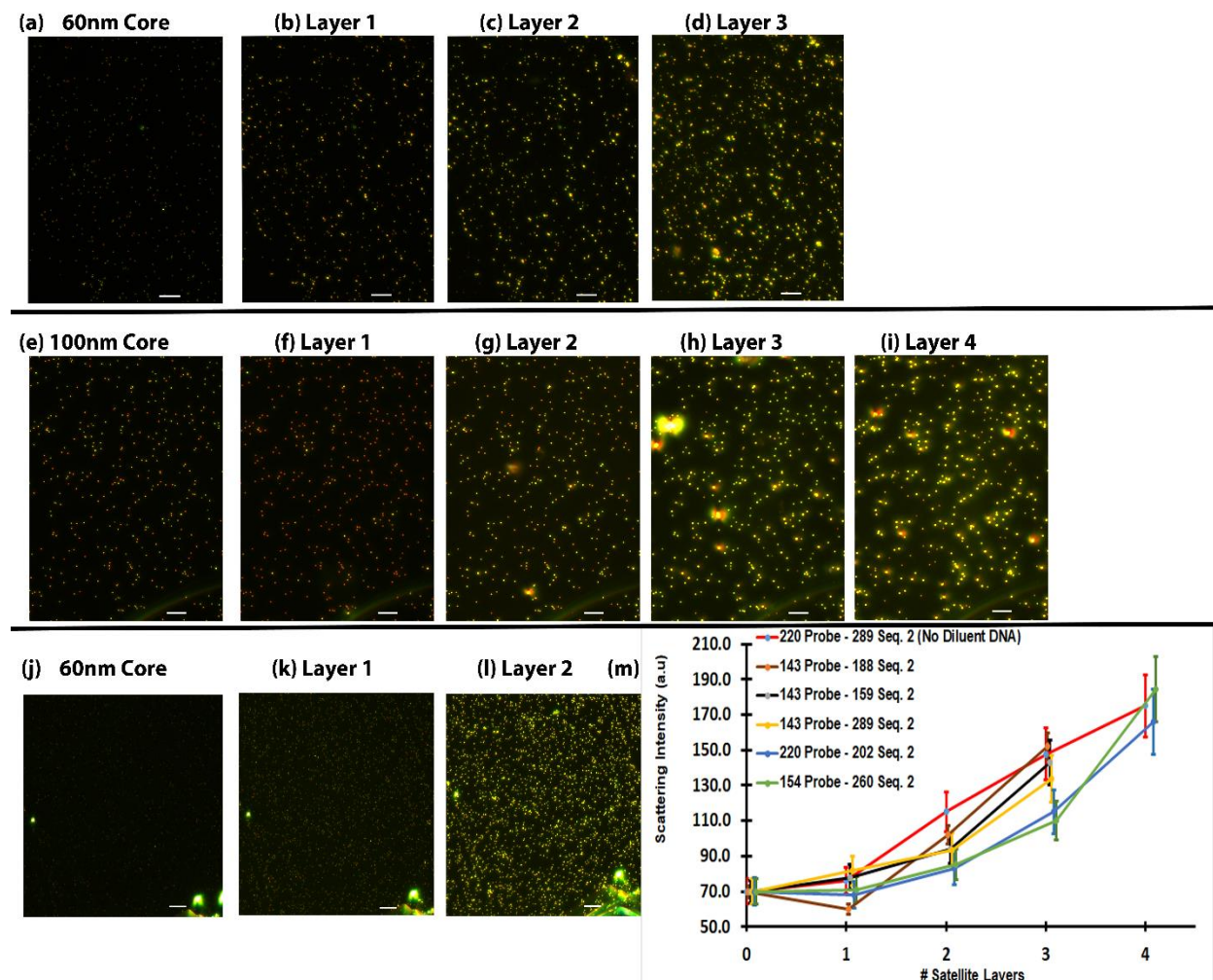


Figure 3-5 A comparison of DF images of the samples during layer-by-layer assembly using different core sizes (60 nm and 100 nm) and with satellite particle bearing varied surface density of Probe. DF images (a-d) represent core-satellite assemblies constructed using 60 nm AuNP core and 30 nm satellite AuNPs bearing maximum surface density of DNA. DF images (e-i) represent core-satellite assemblies formed as in (a-d) but with 100 nm core AuNP. DF images (j-l) represent a two layer nanoassembly formed as in (a-c) but with 121 Probe/AuNP DNA density for the first layer. Plot (e) summarizes the change in scattering intensity with respect to the number of layers of core-satellite nanocluster formed by varying surface density of DNA. Scale bar = 10 μ m in all DF images. Error bars: Std dev (n=100).

scattering of 100 nm core is more intense than 60 nm core because the scattering intensity is proportional to r^6 (where r is the radius of the NP). The extinction cross-section as well as the relative contribution of scattering to the extinction increases as the NP size increases. Additionally, as the size of the core increases, the scattering peak broadens and red-shifts due to retardation

effect where conduction electrons do not move in phase.^[2c, 4, 6, 64] Both 60 nm and 100 nm core can form assemblies (Figure 3-5 a-i), however, the intensity increase offered by the 100 nm core was significantly higher than the 60 nm because 100 nm can bear a greater number of satellites around it in every satellite layer. Another important observation to make is that the first layer on 100 nm core resulted in an entirely red color (Figure 3-5f) whereas 60 nm core did not have as large of a red-shift (Fig 3-5b). The red-shift in the scattered light is due to the local plasmonic coupling when two plasmonic AuNP come in proximity to each other. The big core, due to its larger surface, can bind to more satellite AuNP as compared to the 60 nm core, resulting in a greater red-shift in plasmon peak. According to plasmon hybridization theory, heterodimers display multiple absorption peaks and broader absorption spectra because various bonding and anti-bonding plasmons are excitable by light. Therefore, the magnitude of the red-shift is bigger during the construction of a 30 nm layer on a 100 nm as compared to that obtained by using a 60 nm core.^[6] One of the limitations of using a 100nm core is that as subsequent layers are built on the 100 nm core, the scattering spectra can shift to the near-IR and cannot be visually discerned for the analysis. Additionally, with 100 nm core, only shift in the scattering plasmon was observed, while the increase in scattering intensity was negligible, rendering the nanocluster insensitive below 2nd layer.

The size of the satellite AuNPs was chosen to be 30 nm because as the size of the AuNP decreases, their extinction cross-section and the relative contribution of scattering intensity towards total extinction also decreases. Smaller NPs tend to pack for densely in the nanocluster, hence making it harder to disassemble them by large target molecules. On the other hand, bigger NPs result in lesser number of satellite particles in every layer, making it less sensitive to a change in target concentrations. Moreover, the plasmon band broadens significantly due to retardation effect as the cluster becomes comparable to the size of the wavelength of light.^[2c]

During further layer build-up (Figure 3-5 (c-d) and (g- i)), the dark field images show that the scattering signal gets enhanced from light orange clusters to bright yellow, indicating more satellites are coupling. The multi-layer core satellite exhibits more conduction electrons and electromagnetic interactions, resulting in the formation of higher plasmon coupling modes. Therefore, the increase in the aggregate size is an important signal enhancing factor that is exploited in this sensing platform. Notably, the multi-layered core-satellite allows us to tune the sensing performance, such as detection limit, dynamic range and sensitivity. The enhanced scattering intensity from these nanoaggregates can also be used as contrast agents in cellular and biological imaging where the background noise is high.

Figure 3-5m summarizes the changes in scattering intensity with respect to the number of layers of core-satellite nanocluster. As before, the prefix indicates the surface DNA density (strands/AuNP) and the suffix signifies the type of DNA strands (i.e. 220 Probe denotes AuNP with 220 Probe strands/particle). The maximum surface densities for the Probe sequence and Seq. 2 strands were 220 and 289 strands/AuNP, respectively. In solution-based assembly experiments from Chapter 2, it was observed that the rate of aggregation of AuNPs decreases as the surface DNA coverage is lowered. However, provided that the incubation time for hybridization (40 to 60 min) and the buffer NaCl concentration (0.3 M to 0.4 M) are adequate, variations in the DNA surface coverage on AuNP do not have a significant impact on the intensity changes or the buildup of the layers. Figure 3-5(j to l) show DF images of two-layer assemblies formed on the 60 nm core using 121 Probes/AuNP and 289 Seq.2/AuNP satellite particles where increases in intensity are visibly comparable to nanoaggregates formed using satellite particles bearing maximum DNA density.

3.3.4 Sensing of Oligonucleotide Biomarkers Based on the Disassembly of the Plasmonic Core-Satellite Nanocluster

Next, we explore the target-induced disassembly of these nanoaggregates for sensing the target (DNA-210 or miR-210). Work by a previous group member did not achieve effective disassembly when the surface DNA density was not diluted, in which about 32% of disassembly occurred over 16 hours at 0.2 M NaCl.^[65] Some environmental factors such as the NaCl

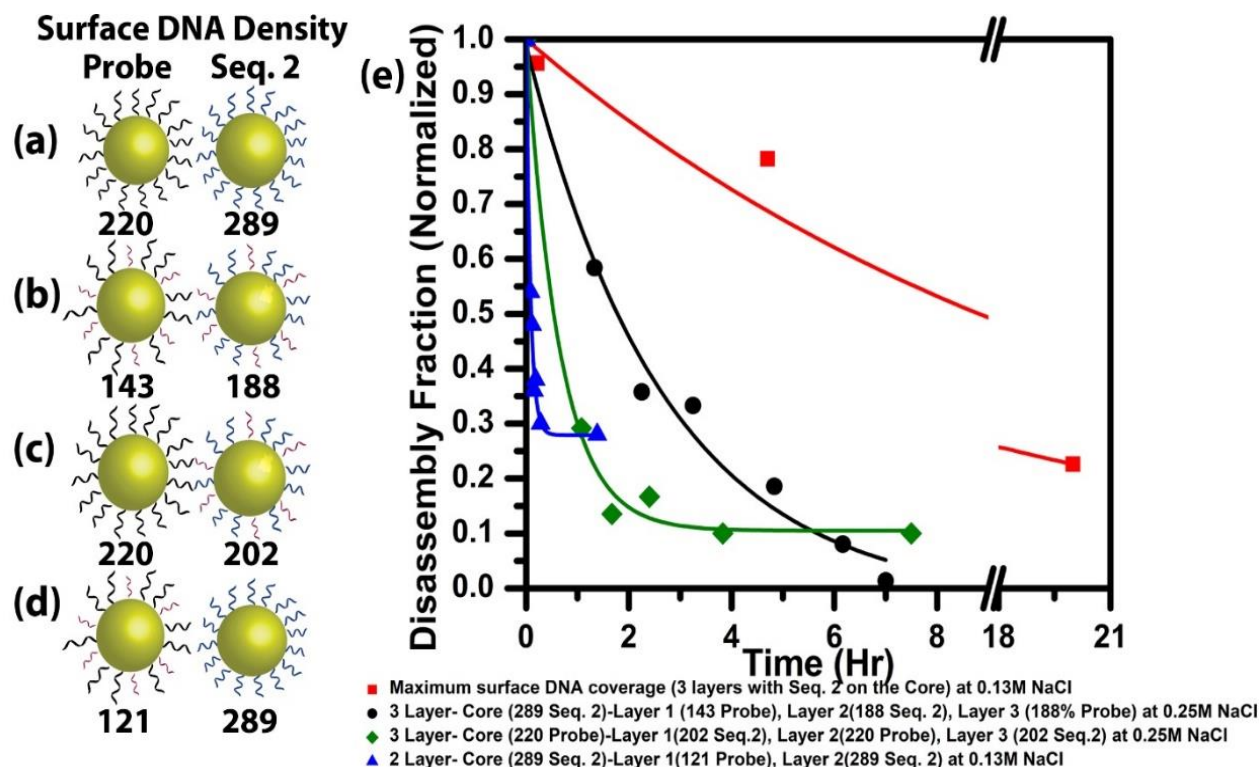


Figure 3-6 The impact of surface density of DNA on the kinetics of target-induced disassembly of surface-bound nanoassemblies with an excess amount (1 μ M) of DNA-210 is illustrated here. Plot in (e) summarizes the rate of disassembly (decay of scattering intensity) overtime. Four combinations of satellite particles bearing varied surface density of DNA were investigated in this study, as illustrated in figure (a-d). The surface density of DNA, number of layers, composition of each layer and the NaCl content are all captured in the legends of (e). Diluting the surface DNA density were generally observed to enhance the disassembly rate even at high NaCl content.

concentration and particle capping impacted the disassembly process and were optimized. The NaCl concentration was lowered from 0.20 M to 0.13 M in this work.

Figure 3-6 shows the impact of the surface density of DNA on the target-induced disassembly of substrate-bound core-satellite nanoclusters. Four combinations of particles with varied surface DNA density (Figure 3-6(a-d)) were analyzed and their kinetics are shown in Figure 3-6e. In 220 Probe-289 Seq. 2, (Figure 3-6a), both sets of particles had maximum DNA density; In 143 Probe-188 Seq. 2 (Figure 3-6b), both particles had reduced surface DNA density; in 220 Probe-202 Seq. 2 (Figure 3-6c), the density of the Seq.2 strands was lowered while the density of Probe was kept maximum; and finally in 121 Probe – 289 Seq. 2 (Figure 3-6d), the density of the Probe sequence was lowered while the density of Seq. 2 was kept maximum. The general observation is that lowering the surface coverage improved the disassembly kinetics dramatically. With an excess amount of target (1 μ M), almost complete disassembly was observed in 20h, 7h, 3h and 0.5h for 220 Probe-289 Seq. 2, 143 Probe-188 Seq. 2, 220 Probe-202 Seq. 2 and 121 Probe – 289 Seq. 2, respectively. The rates of disassembly are in a good agreement with those observed in chapter 2 for colloidal aggregates. When Seq. 2 density is lowered while keeping the Probe density high, the retention of Seq. 2 strand by Probe strand via attinebility is still effective, hence the disassembly rate is relatively long in this combination (green curve in Figure 3-6e). In contrast, when Probe density is lowered while keeping the Seq. 2 density maximum, the affinity between particle is lower because neither sparse Probe sequence can retain Seq. 2 strands, nor inaccessible Seq. 2 can contribute towards attinebility as effectively, thus nanoaggregates disassemble within few minutes (blue curve in Figure 3-6e). As the target replaces Seq. 2 from the Probe strand, it also increases the electrostatic and steric repulsion between particles, hence makes interparticle space more accessible to the subsequent target molecules. This repulsion introduced by the target is higher in the particles with higher Seq. 2 density which further increases the rate of disassembly in combination with high Seq. 2 density. The repulsion introduced by the target is also experienced by the subsequent targets

as well, hence if the crowding at the interparticle space is high, target binding can result in negative cooperativity and result in much slower disassembly rate (red curve in Figure 3-6e).

3.3.5 Calibration Curve for DNA-210 and miR-210 sensing

We optimized the structure of the nano-assembly, i.e. the number of layers in the nanocluster, which layer should be comprised of which DNA-AuNPs and what surface DNA coverage to use. Hereafter, due to their fast kinetics, assemblies with 121 Probe/AuNP and 289 Seq.2/AuNP combination were exploited to construct the calibration curve. Previous work showed that the first and second layer on a 60 nm core is roughly comprised of 6 and 18 satellite (30 nm) particles, respectively.^[59] The surface coverage of oligonucleotides on a 60 nm particle is ~900 strands/particles.^[49] Therefore, in a two-layer system, using probe-functionalized satellite particles in the first layer results in 726 Probe/nanocluster; on the other hand, using Probe on the core and the second satellite layer would result in ~2700 Probe/nanocluster. To achieve the lowest detection limit, two-layered nanocluster with the first layer comprised of Probe-functionalized-AuNPs was selected for calibration curve construction.

The performance of the core-satellite sensor was explored by constructing a calibration curve for DNA-210 and miR-210. Figure 3-7a shows the DF images of nanoparticle assemblies at various concentrations of the target after incubating for 1h: the scattering intensity decreases with increasing concentration of the target. Figure 3-7b and c show the calibration curves for the quantification of DNA-210 and miR-210. On a linear scale (Figure 3-7b), a hyperbolic relationship is observed between the scattering intensity and the target concentration and can be well described by Langmuir binding isotherm. When plotted on a semi-log scale (Figure 3-7c), the relationship becomes sigmoidal which can be analyzed by a linear approximation between the scattering intensity and log[target]. A linear relation is observed between the scattering intensity and

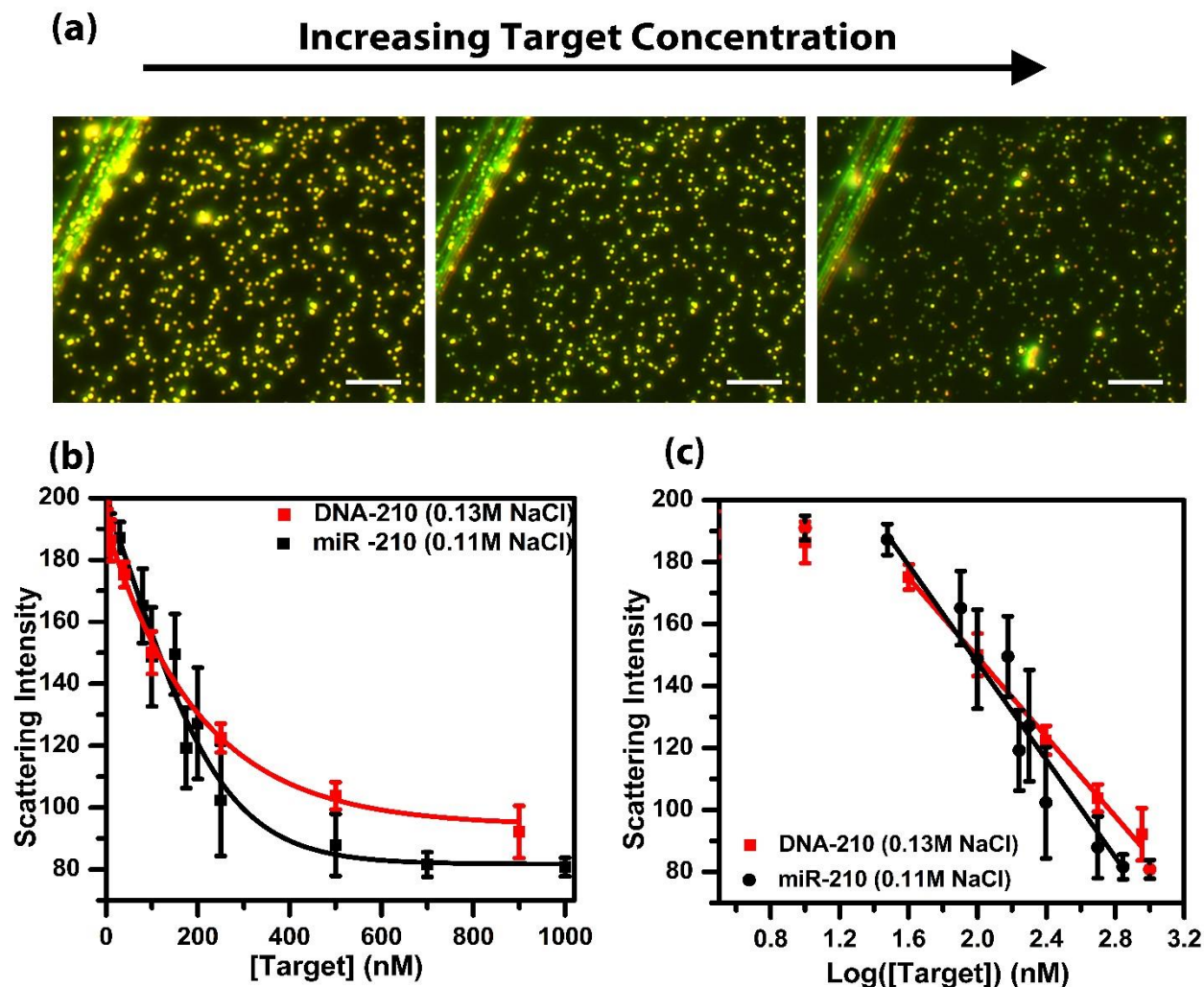


Figure 3-7 The calibration curves for the quantification of DNA-210 and miR-210. DF images of nanoparticle assemblies at various concentrations of target after incubating for 1h. are shown in (a). (b) shows the relationship between scattering intensity and the target (DNA-210 (red) or miR-210(black)) and target concentration. (c) reveals a linear relationship between scattering intensity and the log of target concentration. Scale bar = 10 μ m for DF images. Note: Different NaCl content was required for these two targets. Fitting equation in (c) - DNA-210: $y = -64.2x + 277.7$ ($R^2 = 0.997$), miR-210: $y = -78.6x + 304.8$ ($R^2 = 0.986$). Error bars: std dev (n=3).

log[target]. No disassembly is observed for concentrations lower than the limit of detection (LOD) value. As the target concentration is further increased, more targets bind to the probes and some of the nanoclusters start to disassemble resulting in a slower decrease in scattering intensity. The rate of intensity decrease increases as more targets are introduced because all nanoclusters start to disassemble resulting in a maximum disassembly rate at the point of inflection on the semi-log

scale plot (Figure 3-7c). Upon further addition of target, nanocluster starts to reach their saturation point hence the rate of decrease in the scattering intensity slows resulting in a sigmoidal disassembly curve on the semi-log scale. Calibration curves reveal that the detection range spans from 10 nM to ~800 nM and 10 nM to ~650 nM for DNA-210 and miR-210, respectively. The sensitivity of the sensor is derived from the slope of the scattering intensity vs log[target]. Although the sensor appears to be more sensitive towards the miR-210 (slope = -78.6 ± 7.2 units/Log(nM)) as compared to its DNA analogue (slope = -64.2 ± 6.1 units/Log(nM)), they both required different buffer conditions which could potentially contribute towards their different sensitivity. For miR-210 detection, the NaCl content had to be further reduced to observe disassembly in nM range because very limited disassembly was observed at 0.13 M NaCl (results not shown). Compared to DNA counterparts, RNAs are known to form more stable secondary structures^[66] which are further stabilized by at higher NaCl content, hence could potentially be the cause for their poor performance at 0.13 M NaCl. At 0.11 M NaCl, the strand displacement reaction is enhanced due to decreased charge shielding by counter ions resulting in a higher interparticle repulsion and due to reduced stability of Probe-Seq. 2 duplex, which could enhance the sensitivity towards miR-210. Additionally, at lower Na⁺ content, the shielding of AuNPs is relatively poor; therefore, interparticle repulsion is expected to be high, thus giving more accessibility for the target binding. The apparent dissociation constant (K_d) is inversely proportional to the affinity constant between the target and the Probe. Using the Langmuir isotherm model, the K_d value for DNA-210 and miR-210 was estimated to be approximately 162 ± 10 nM and 188 ± 20 nM, respectively. The lower the K_d , the higher the affinity. Although the K_d value is in the nM range, it is not enough to detect ultra-low concentrations of extracellular miRNA.

3.3.6 Direct Measurement in Cell Lysate

The practicality and robustness of our sensing platform were explored for the detection of miR-210 in human trophoblast cells (HTR-8/SVneo). Hypoxia is known to upregulate the expression of miR-210 in these cells. To determine the upregulation of miR-210 in hypoxic cells, CoCl_2 , a hypoxia inducing agent, was used. Figure 3-8 shows the DF images and scattering intensities of nanoclusters before and after they are exposed to the hypoxic and normoxic cell lysate. The negative control experiments were performed by constructing assemblies using control-DNA sequences (Control-1 and Control-1-complement). The overall structure and surface density of DNA was similar to that of our sensing platform, i.e., 2 layers using 55% Control-1 and 100% Control-1-complement strands. Figure 3-8a, b and c show the DF images for normoxic cell lysate, hypoxic cell lysate and negative control (for hypoxic lysate), respectively. When exposed to the lysate of normoxic cells, the scattering intensity decreased from 142.8 ± 15.0 to 109.1 ± 27.3 units; in comparison, the lysate of hypoxic cells lowered the scattering intensity from 148.3 ± 20.16 to 87.4 ± 23.1 units (Figure 3-8d). No significant change in scattering intensity is observed in control experiments with hypoxic and normoxic cell lysate. These scattering intensities translate to miR-210 concentrations of ~ 194 nM and ~ 485 nM for normoxic and hypoxic cell lysates based on the calibration curve; the miR-210 level in hypoxic cells is ~ 2.5 -fold higher than in normoxic cells. The extent of upregulation detected by our sensing platform strongly agrees with the reported results of 2-3-fold difference based on RT-qPCR technique.^[67] In comparison, negligible change in the scattering intensity is observed for the control assemblies (Fig. 3-8c), supporting the sequence-specificity of our sensing platform and that disassembly does not arise from other cellular biomolecular interactions. The sensor demonstrated the ability to directly detect miR-210 for biological samples without labelling and amplification requirements using a few μL sample

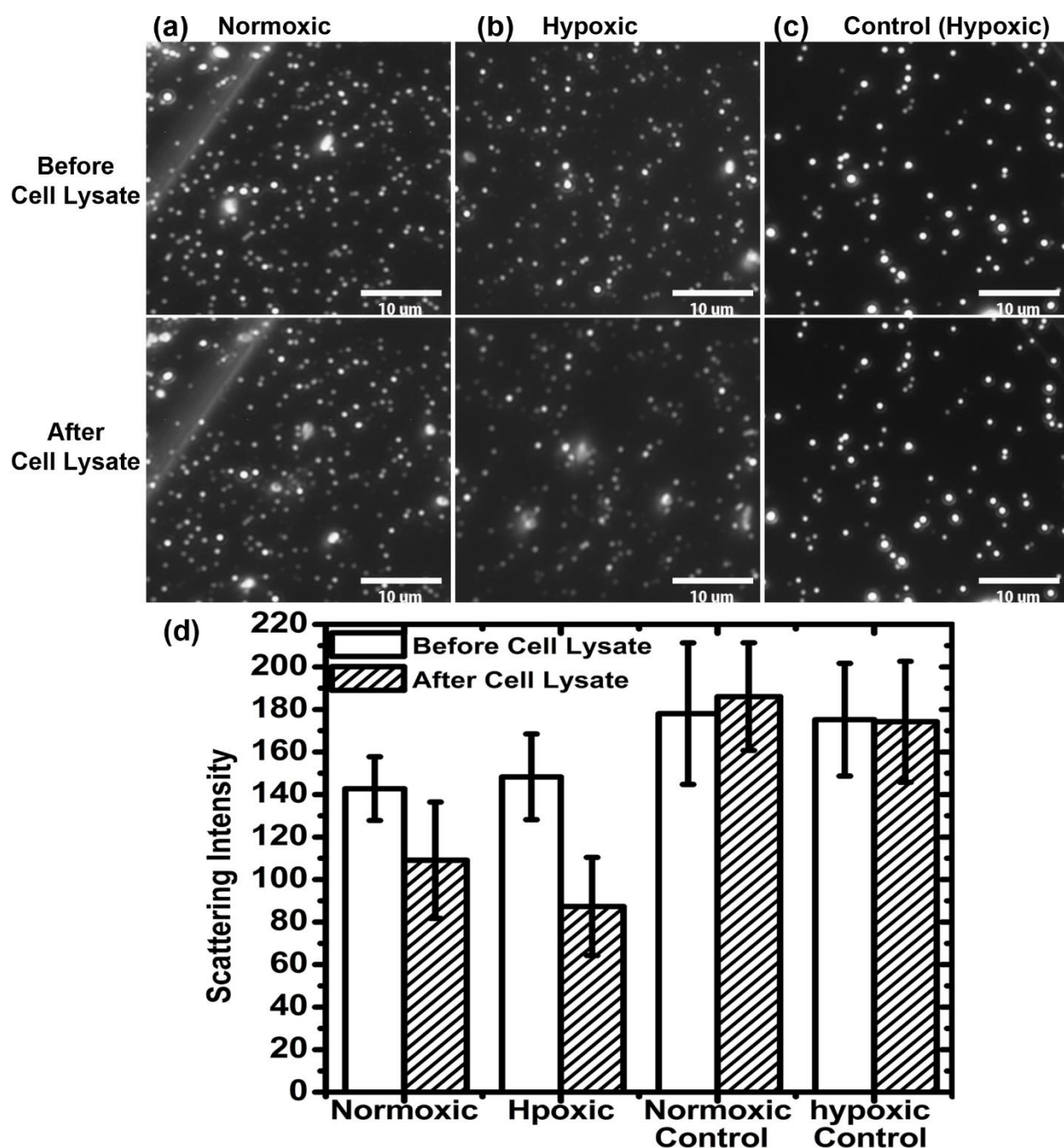


Figure 3-8 DF images and scattering intensities of core-satellite nanoassemblies before and after they are exposed to hypoxic and normoxic cell lysate. DF images of sensors before and after exposure to cell lysate from normoxic cells (a), from hypoxic cells (b). (c) shows nanoassemblies formed by using scrambled DNA sequences before and after exposure to hypoxic cell lysate. (d) summarizes the scattering intensity before and after exposure to their corresponding cell lysate. Error bars: std dev (n=51). Scale bar in DF images = 10 μm

volume within one hour. Hence, we developed a non-invasive, rapid and a personalized sensor which can be considered as a new medical tool for relevant clinical samples, leading to improved

patient prognosis. Ability to profile microRNA expression pattern offers tremendous potential for the diagnosis of a broad range of diseases such as cancer, cardiovascular disorders, Alzheimer's.

3.4 Conclusion

We successfully adapted our previous ATP sensing platform to detect oligonucleotides in complex solutions. We manipulated the system for the rapid and selective detection of an exemplary nucleic acid biomarker-miR210 by tuning and optimizing the thermodynamic and kinetic properties of the toehold-mediated strand displacement reactions on the particle surface.

Passivation of the substrate is critical for the functionality of the sensor. Secondary passivation by acylating after PEGylating the substrate is an effective method to further minimize specific and non-specific interactions with the substrate. A wide range of surface density of DNA was able to generate similar sized assemblies without compromising the S/N ratio. We were able to control the thermodynamic and kinetic properties of the toehold-mediated disassembly by modifying the surface DNA density. Higher DNA crowding at the interparticle junction retards the binding of the target to the Probe strand to initiate disassembly, hence results in incomplete and slower disassembly. Diluting the surface density of DNA dramatically enhance the disassembly process by lowering DNA crowding, cooperativity and attainability. Probe strands contribute more effectively towards attainability and cooperativity due to their markedly higher accessibility as compared to Seq. 2. Due to their larger size and more negative charge, the inaccessible Seq. 2 strands facilitate the disassembly via interparticle repulsion. Therefore, lowering the probe density while keeping the Seq. 2 density high result in a fast and immediate disassembly.

The detection span of the two-layered nanoassembly is from ~10 nM to ~800 nM and 10 nM to ~650 nM for DNA-210 and miR-210, respectively. The sensitivity towards miR-210 is -78.6 units/log(nM) and -64.2 units/Log(nM) towards DNA-210. A moderate affinity between the

target and the Probe strand was observed with the apparent K_d value of 162 ± 10 nM and 188 ± 20 nM for DNA-210 and miR-210, respectively.

Chapter 4. Outlook and Future work

4.1 Summary

Through this work, we have gained a fundamental insight at the impact of the surface density of DNA on the binding properties of the immobilized DNA strands. The surface density of DNA was observed to impact the aggregate formation and disassembly of DNA-AuNPs at many levels. Varying the surface DNA density was observed to impact the accessibility of the functional DNA stands dramatically. The accessibility of the DNA strand on the surface is critical in determining the role of densely populated DNA in positive or negative cooperativity. Then the impact of surface DNA density on the aggregate formation revealed that the hybridization kinetics of the immobilized DNA strands on two sets of AuNPs is also subject to the surface DNA density. An increase in the surface density of Probe significantly increased the hybridization kinetics, thus aggregate formation due to enhanced cooperativity via attinebility and avidity. Seq. 2 strands have very limited accessibility; therefore, they were the limiting strands at the interparticle junction, hence controlled the number of links between the particle. High probe density resulted in cooperative binding via attinebility during thermal and target-induced disassembly. The impact of surface DNA density on the thermodynamic and kinetic properties of toehold-mediated strand displacement reaction on the AuNP surface revealed that the high Probe density delays and slows the disassembly by retaining newly dissociated Seq. 2 via attinebility and due to increased crowdedness at the interparticle junction which retards subsequent target bindings. The density of Seq. 2 was also observed to increase the disassembly rate via enhancement of repulsive forces between particles upon target binding to the probe sequence.

These fundamental studies were necessary to understand the factors that impact the toehold-mediated strand displacement reaction on the particle surface. Our findings have the potential to facilitate the rational design of surface-bound dynamic DNA nanomachines. The

fundamental understandings from chapter-2 allowed us to design and adapt to a label-free, low cost and miniaturized biosensing platform based on the disassembly of core-satellite nanoassemblies. Our sensing platform provides various factors that can allow extensive tunability of sensing performance. A wide range of surface density of DNA was able to generate similar sized assemblies without compromising the S/N ratio. Surface DNA density, size of the cluster, the ionic content of the buffer, and changing the size of the core or satellite particles can all separately and exclusively alter the sensing performance of our platform dramatically. For instance, the lower surface density of DNA and lower ionic content of the buffer was able to shift the dynamic range from μM range to nM range and enhance the sensitivity and kinetic properties of the sensor. The ability of our sensing platform to span from small molecule to macromolecule detection qualifies it for diverse biological applicability. Our sensing platform satisfies many of the crucial needs for the clinical and environmental applicability, such as specificity, reproducibility, high sensitivity, high S/N ratio, wide dynamic range, reasonable detection limit and compatibility with unprocessed samples. Additionally, being a chip-based sensor, it can easily be incorporated with microfluidic setup and can be made portable, reusable, and can also be used in a variety of point-of-care environments. Furthermore, miniaturization in the form of nanoarrays would allow multiplexed detection with improved detection limits.

Although our sensing platform worked well for the detection of miR-210, we have not achieved the maximum performance of this sensor yet. Our sensor with two layers of satellite particle should completely disassemble with sub-picomolar target concentration but it revealed a moderate limit of detection of approximately $\sim 10\text{nM}$ which is far bigger than expected. Other factors such as specific or non-specific binding interactions of the target to the substrate, to the perfusion chamber or to the molecules used to protect the substrate should be studied to improve

the limit of detection. The impact of DNA crowding on the core-satellite nanoassemblies might be higher than the aggregates formed in solutions, thus preventing the target to access the interparticle junction. To minimize the crowding and electrostatic repulsion from these densely packed DNA strands, neutral diluent molecules can be used to modulate the surface DNA density. Additionally, the area of the substrate used to construct nanoassemblies is much larger than needed which can be reduced to improve the LOD. The sensitivity of the sensor is also lower than what was expected from calculations which can also be attributed to the same factors involved in poor LOD. It is essential to resolve issues related to the limit of detection and sensitivity because if they can be improved, our sensor may be valuable for point-of-care testing. The reproducibility also needs to be further improved in order to achieve a rigorous method that can accurately distinguish a few fold up or down-regulation of miR-210. To achieve more reproducible results, the surface coverage of clusters on the 2-D glass substrate needs to be controlled precisely. Current, electrostatic interaction between the core particle and the amino-modified substrate does not offer control over the surface coverage of nanoclusters. Additionally, as observed in chapter 2, the surface DNA density on the particle surface should be verified prior to use in order to minimize variation in DNA density on the satellite particles.

Our work has addressed some of the demands of developing a biosensor for point-of-care testing, for example, it can be used by minimally trained personnel if the data processing is automated. Additionally, our sensor has the ability to perform in complex media eliminating the need for sample purification steps and to some extent minimizes the need for sample enrichment and amplification. Moreover, our work has values in sensor design, e.g. kits, chips, that can be used by other researchers, not necessarily for diagnostic purpose. There are already many powerful methods available for detecting and sensing miRNA, therefore any new sensor needs to pose

significant economical and/or practical advantages for the end user. Most of the benchmark techniques that require sample processing and extraction of miRNA can take more than a day due to the small size of miRNA. Additionally, the recovery and purification of miRNA using commercial kits requires a few hours. In comparison, we were able to directly detect the miRNA in the cell lysate in less than 30 min. Being suitable for miniaturization, our sensor can be incorporated into low-cost and portable microscopic devices that can be attached to a smartphone. With advances in miniaturized electronics and smartphones, our sensor can be used as a common and convenient tool to perform lab-on-a-chip based POC biomedical application. By using the digital camera and advanced computational capacity of smartphones, microscopic DF images can be captured, magnified, processed and analyzed in real time for POC diagnosis. The total cost of the portable device can be estimated to be approximately \$7 and the fabrication cost of each microfluidic chip or glass slider is roughly \$1 or less. The cost of reagents and material is quite low for our platform as compared to RT-qPCR. The minimum amount of sample required for our assay is roughly 2 ng which is comparable to most of the miRNA detection platforms that do not use amplification step. With these economical and practical advantages, these techniques capable for selective and specific detection of miRNA biomarkers could potentially transform the way diseases are diagnosed and treated.

4.2 Outlook and Future Work

Although the sensor has satisfied many of the requirements for clinical applicability, the lower limit of detection is still not low enough to look at samples with smaller cell numbers such as 3D spheroids (~10-10 000 cells), circulating cell clusters (~10-100 cells), organoids (~1000-10 000 cells), early-stage embryos (~10-100 cells) and small whole organisms (~1000 cells). Therefore, there is a need to lower the dynamic range of this biosensor. Currently we are working

with cluster spread on large 2-D surface area ($\sim 20 \text{ mm}^2$) which contains about 5×10^5 nanoclusters, therefore all clusters should disassembly with sub-nM target concentration ($\sim 15 \text{ pM}$), however no disassembly is observed until about 15 nM target is added. Additionally, the sensitivity is about $64 \text{ units}/\log(\text{nM})$. Clearly, something on the substrate is inhibiting or impacting the efficiency of disassembly process and there is an opportunity to improve the sensing performance. The detection limit can be lowered further by reducing the working area from mm scale to μM scale. Additionally, we have not explored lower Probe surface density than 121 Probe/AuNP which could further enhance the disassembly process.

Now that our sensing platform has been established for the detection of ATP and oligonucleotides via completely different mechanisms, it opens an opportunity for the multiplexed detection of ATP and miR-210 by constructing these clusters on the same area. Additionally, as reported for the ATP sensing platform, miR-210 content in a cell may directly be measured by lysing the cell in close proximity of the nanoassemblies.

Chapter 5. References

- [1] a) S. Unser, I. Bruzas, J. He and L. Sagle, *Sensors* **2015**, *15*, 15684-15716; b) L. Wang, Y. Sun, Z. Li, A. Wu and G. Wei, *Materials* **2016**, *9*, 53; c) Y. Wang, E. MacLachlan, B. K. Nguyen, G. Fu, C. Peng and J. I. Chen, *Analyst* **2015**, *140*, 1140-1148.
- [2] a) C. Sönnichsen, B. M. Reinhard, J. Liphardt and A. P. Alivisatos, *Nature Biotechnology* **2005**, *23*, 741; b) Y.-w. Jun, S. Sheikholeslami, D. R. Hostetter, C. Tajon, C. S. Craik and A. P. Alivisatos, *Proceedings of the National Academy of Sciences* **2009**, *106*, 17735-17740; c) J. R. Waldeisen, T. Wang, B. M. Ross and L. P. Lee, *ACS Nano* **2011**, *5*, 5383-5389.
- [3] X. Fan, I. M. White, S. I. Shopova, H. Zhu, J. D. Suter and Y. Sun, *Analytica Chimica Acta* **2008**, *620*, 8-26.
- [4] E. Petryayeva and U. J. Krull, *Analytica Chimica Acta* **2011**, *706*, 8-24.
- [5] K. A. Willets and R. P. Van Duyne, *Annual Review of Physical Chemistry* **2007**, *58*, 267-297.
- [6] P. Nordlander, C. Oubre, E. Prodan, K. Li and M. I. Stockman, *Nano Letters* **2004**, *4*, 899-903.
- [7] N. J. Halas, S. Lal, W.-S. Chang, S. Link and P. Nordlander, *Chemical Reviews* **2011**, *111*, 3913-3961.
- [8] S. K. Ghosh and T. Pal, *Chemical Reviews* **2007**, *107*, 4797-4862.
- [9] R. Elghanian, J. J. Storhoff, R. C. Mucic, R. L. Letsinger and C. A. Mirkin, *Science* **1997**, *277*, 1078.
- [10] N. L. Rosi and C. A. Mirkin, *Chemical Reviews* **2005**, *105*, 1547-1562.
- [11] G. Vauquelin and S. J. Charlton, *British journal of pharmacology* **2013**, *168*, 1771-1785.
- [12] P. Rajendran in *Plasmonic nanoparticles with tailored attinebility for direct oligonucleotide sensing - Optimization & Application*, Vol. ETH Zürich, **2015**.
- [13] J. D. Badjić, A. Nelson, S. J. Cantrill, W. B. Turnbull and J. F. Stoddart, *Accounts of Chemical Research* **2005**, *38*, 723-732.

- [14] Q.-l. Lei, C.-l. Ren, X.-h. Su and Y.-q. Ma, *Scientific reports* **2015**, 5, 9217-9217.
- [15] J. A. Milton, S. Patole, H. Yin, Q. Xiao, T. Brown and T. Melvin, *Nucleic Acids Research* **2013**, 41, e80-e80.
- [16] H. Pei, F. Li, Y. Wan, M. Wei, H. Liu, Y. Su, N. Chen, Q. Huang and C. Fan, *Journal of the American Chemical Society* **2012**, 134, 11876-11879.
- [17] L.-A. Macfarlane and P. R. Murphy, *Current genomics* **2010**, 11, 537-561.
- [18] W. Tian, X. Dong, X. Liu, G. Wang, Z. Dong, W. Shen, G. Zheng, J. Lu, J. Chen, Y. Wang, Z. Wu and X. Wu, *PloS one* **2012**, 7, e29551-e29551.
- [19] a) L. Moldovan, K. Batte, Y. Wang, J. Wisler and M. Piper, *Methods in Molecular Biology* **2013**, 453-451_410; b) L. Moldovan, K. E. Batte, J. Trgovcich, J. Wisler, C. B. Marsh and M. Piper, *Journal of Cellular and Molecular Medicine* **2014**, 18, 371-390.
- [20] S. G. Jensen, P. Lamy, M. H. Rasmussen, M. S. Ostenfeld, L. Dyrskjot, T. F. Orntoft and C. L. Andersen, *BMC Genomics* **2011**, 12, 1471-2164.
- [21] C. C. Pritchard, H. H. Cheng and M. Tewari, *Nature reviews. Genetics* **2012**, 13, 358-369.
- [22] T. Wang, E. Viennois, D. Merlin and G. Wang, *Analytical Chemistry* **2015**, 87, 8173-8180.
- [23] D. Grieshaber, R. MacKenzie, J. Vörös and E. Reimhult, *Sensors* **2008**, 8, 1400-1458.
- [24] P. Gillespie, S. Ladame and D. O'Hare, *Analyst* **2019**, 144, 114-129.
- [25] M. R. Williams, R. D. Stedtfeld, T. M. Stedtfeld, J. M. Tiedje and S. A. Hashsham, *Biomedical microdevices* **2017**, 19, 45-45.
- [26] Y.-H. Wang, L.-L. He, K.-J. Huang, Y.-X. Chen, S.-Y. Wang, Z.-H. Liu and D. Li, *Analyst* **2019**, 144, 2849-2866.
- [27] a) C. K. Almlie, N. E. Larkey and S. M. Burrows, *Analytical Methods* **2015**, 7, 7296-7310; b) A. M. James, M. B. Baker, G. Bao and C. D. Searles, *Theranostics* **2017**, 7, 634-646.

- [28] J. Zheng, R. Yang, M. Shi, C. Wu, X. Fang, Y. Li, J. Li and W. Tan, *Chemical Society Reviews* **2015**, *44*, 3036-3055.
- [29] L. Moody, H. He, Y.-X. Pan and H. Chen, *Clinical epigenetics* **2017**, *9*, 119-119.
- [30] a) G. Fu, J. Brkic, H. Hayder and C. Peng, *International Journal of Molecular Sciences* **2013**, *14*, 5519-5544; b) Z. Zhao, K. H. Moley and A. M. Gronowski, *Clinical Biochemistry* **2013**, *46*, 953-960.
- [31] R. Luo, Y. Wang, P. Xu, G. Cao, Y. Zhao, X. Shao, Y.-x. Li, C. Chang, C. Peng and Y.-l. Wang, *Scientific reports* **2016**, *6*, 19588-19588.
- [32] a) Y. Zhang, M. Fei, G. Xue, Q. Zhou, Y. Jia, L. Li, H. Xin and S. Sun, *Journal of cellular and molecular medicine* **2012**, *16*, 249-259; b) R. Kulshreshtha, M. Ferracin, S. E. Wojcik, R. Garzon, H. Alder, F. J. Agosto-Perez, R. Davuluri, C.-G. Liu, C. M. Croce, M. Negrini, G. A. Calin and M. Ivan, *Molecular and Cellular Biology* **2007**, *27*, 1859; c) P. Fasanaro, Y. D'Alessandra, V. Di Stefano, R. Melchionna, S. Romani, G. Pompilio, M. C. Capogrossi and F. Martelli, *The Journal of biological chemistry* **2008**, *283*, 15878-15883; d) H. Dweep and N. Gretz, *Nature Methods* **2015**, *12*, 697.
- [33] M. Yamanaka-Tatematsu, A. Nakashima, N. Fujita, T. Shima, T. Yoshimori and S. Saito, *PloS one* **2013**, *8*, e76605-e76605.
- [34] D. Y. Zhang and G. Seelig, *Nature Chemistry* **2011**, *3*, 103.
- [35] L. Qian and E. Winfree, *Science* **2011**, *332*, 1196.
- [36] Y. Zhao, H. Wang, W. Tang, S. Hu, N. Li and F. Liu, *Chemical Communications* **2015**, *51*, 10660-10663.
- [37] M. Rudchenko, S. Taylor, P. Pallavi, A. Dechkovskaia, S. Khan, V. P. Butler, Jr., S. Rudchenko and M. N. Stojanovic, *Nature Nanotechnology* **2013**, *8*, 580-586.
- [38] Y. Zhao, F. Chen, Q. Li, L. Wang and C. Fan, *Chemical Reviews* **2015**, *115*, 12491-12545.

- [39] B. Yurke, A. J. Turberfield, A. P. Mills Jr, F. C. Simmel and J. L. Neumann, *Nature* **2000**, 406, 605.
- [40] Y. Guo, B. Wei, S. Xiao, D. Yao, H. Li, H. Xu, T. Song, X. Li and H. Liang, *Quantitative Biology* **2017**, 5, 25-41.
- [41] G. Seelig, D. Soloveichik, D. Y. Zhang and E. Winfree, *Science* **2006**, 314, 1585.
- [42] K. E. Dunn, M. A. Trefzer, S. Johnson and A. M. Tyrrell, *Scientific reports* **2016**, 6, 29581.
- [43] A. W. Peterson, R. J. Heaton and R. M. Georgiadis, *Nucleic Acids Research* **2001**, 29, 5163-5168.
- [44] H. M. Watkins, A. J. Simon, F. Ricci and K. W. Plaxco, *Journal of the American Chemical Society* **2014**, 136, 8923-8927.
- [45] J. Xu and S. L. Craig, *Journal of the American Chemical Society* **2005**, 127, 13227-13231.
- [46] J. Zhang, H. P. Lang, G. Yoshikawa and C. Gerber, *Langmuir* **2012**, 28, 6494-6501.
- [47] X. Zhang, M. R. Servos and J. Liu, *Journal of the American Chemical Society* **2012**, 134, 7266-7269.
- [48] D. Y. Zhang and E. Winfree, *Journal of the American Chemical Society* **2009**, 131, 17303-17314.
- [49] a) S. J. Hurst, A. K. R. Lytton-Jean and C. A. Mirkin, *Analytical Chemistry* **2006**, 78, 8313-8318;
b) H. D. Hill, J. E. Millstone, M. J. Banholzer and C. A. Mirkin, *ACS Nano* **2009**, 3, 418-424.
- [50] S. S. Hinman, K. S. McKeating and Q. Cheng, *Analytical Chemistry* **2017**, 89, 4272-4279.
- [51] J.-H. Oh and J.-S. Lee, *Analytical Chemistry* **2011**, 83, 7364-7370.
- [52] S. Seo, J. H. Joo, D. H. Park and J.-S. Lee, *The Journal of Physical Chemistry C* **2017**.
- [53] a) R. Jin, G. Wu, Z. Li, C. A. Mirkin and G. C. Schatz, *Journal of the American Chemical Society* **2003**, 125, 1643-1654; b) O.-S. Lee, T. R. Prytkova and G. C. Schatz, *The Journal of Physical Chemistry Letters* **2010**, 1, 1781-1788; c) E. M. Hotze, T. Phenrat and G. V. Lowry, *Journal of Environmental Quality* **2010**, 39, 1909-1924.
- [54] P. G. Gottschalk and J. R. Dunn, *Analytical Biochemistry* **2005**, 343, 54-65.

- [55] C. J. Wienken, P. Baaske, S. Duhr and D. Braun, *Nucleic Acids Research* **2011**, 39, e52-e52.
- [56] S. E. Seo, T. Li, A. J. Senesi, C. A. Mirkin and B. Lee, *Journal of the American Chemical Society* **2017**, 139, 16528-16535.
- [57] T. Forster, *Naturwissenschaften* **1946**, 33, 166-175.
- [58] N. C. Seeman and H. F. Sleiman, *Nature Reviews Materials* **2017**, 3, 17068.
- [59] N. H. Le, B. K. Nguyen, G. Ye, C. Peng and J. I. L. Chen, *ACS Sensors* **2017**, 2, 1578-1583.
- [60] N. Abello, H. A. Kerstjens, D. S. Postma and R. Bischoff, *Journal of Proteome Research* **2007**, 6, 4770-4776.
- [61] a) S. Bidault and A. Polman, *Water-Based Assembly and Purification of Plasmon-Coupled Gold Nanoparticle Dimers and Trimers*, **2012**, p; b) X. Han, J. Goebel, Z. Lu and Y. Yin, *Langmuir* **2011**, 27, 5282-5289.
- [62] B. Cha, T. Chen, R. Sarker, J. Yang, D. Raben, C. M. Tse, O. Kovbasnjuk and M. Donowitz, *American Journal of Physiology-Cell Physiology* **2014**, 307, 23.
- [63] N. Gandra, A. Abbas, L. Tian and S. Singamaneni, *Nano Letters* **2012**, 12, 2645-2651.
- [64] B. M. Ross, J. R. Waldeisen, T. Wang and L. P. Lee, *Applied Physics Letters* **2009**, 95, 193112.
- [65] B. K. Nguyen in *Optical Detection of Oligonucleotide Biomarkers Based on the Disassembly of Plasmonic Core-Satellite Nanoclusters*, Vol. Bachelor of Science (HONS.) York University, Toronto, **2016**.
- [66] a) M. Bercy and U. Bockelmann, *Nucleic Acids Research* **2015**, 43, 9928-9936; b) E. A. Lesnik and S. M. Freier, *Biochemistry* **1995**, 34, 10807-10815.
- [67] a) B. L. Pineles, R. Romero, D. Montenegro, A. L. Tarca, Y. M. Han, Y. M. Kim, S. Draghici, J. Espinoza, J. P. Kusanovic, P. Mittal, S. S. Hassan and C. J. Kim, *American Journal of Obstetrics & Gynecology* **2007**, 196, 008; b) D. A. Enquobahrie, D. F. Abetew, T. K. Sorensen, D.

Willoughby, K. Chidambaram and M. A. Williams, *American Journal of Obstetrics & Gynecology*
2011, 204, 20.

Appendix A.

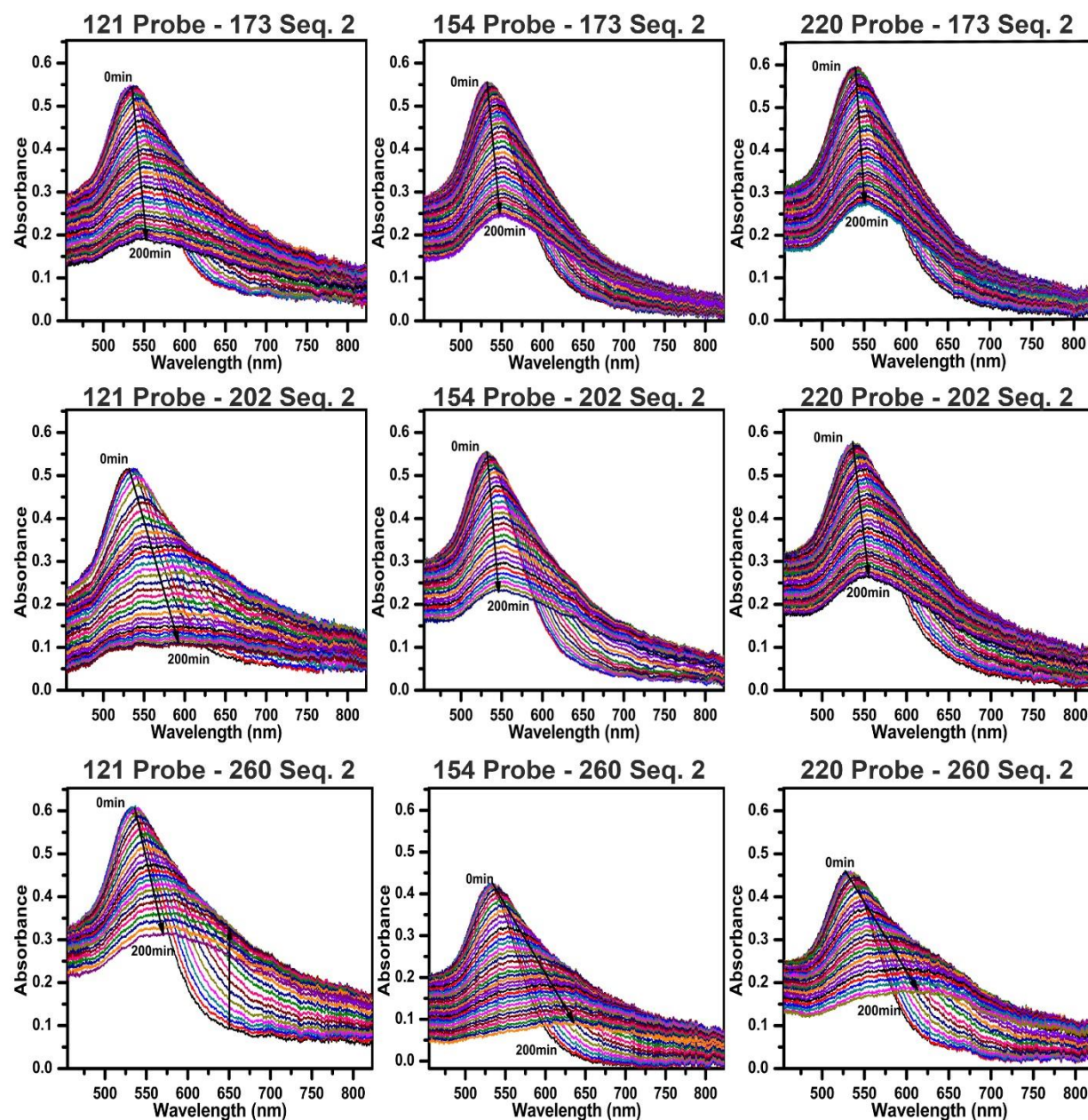


Figure S-1 Monitoring the LSPR peak by UV-Vis spectroscopy during the aggregation of AuNPs with varied surface density of DNA in solution-phase. Initially, the AuNPs exhibit a sharp peak at 526nm which redshifts and broadens as the aggregation proceeds. Arrows indicate the progression of aggregation over time.